

# Structural Analysis for Large-Scale Space Domain Awareness Simulator

Justin Bak  
Space Systems Design Studio  
Cornell University  
Advised by Dr. Mason Peck

May 2025

## Contents

<b>1 Abstract</b>	<b>4</b>
<b>2 Acknowledgements</b>	<b>4</b>
<b>3 Introduction</b>	<b>5</b>
3.1 Requirements . . . . .	5
3.2 Trade Study . . . . .	6
3.2.1 COTS Design . . . . .	6
3.3 Custom Design I . . . . .	8
3.3.1 Custom Design II . . . . .	10
3.3.2 Custom Design III . . . . .	11
3.4 Comparison of Designs . . . . .	13
<b>4 Literature Review</b>	<b>15</b>
<b>5 Methodology and Experimental Details</b>	<b>21</b>
5.1 General Meshing Practices . . . . .	21
5.2 Mesh Convergence Study . . . . .	24
5.3 Freely-Rotating Modal Analysis . . . . .	28
5.4 Constant-Spin Modal Analysis . . . . .	30
5.5 Prestressed Modal Analysis . . . . .	31
<b>6 Results and Discussions</b>	<b>37</b>
6.1 Freely-Rotating Modal Analysis Results . . . . .	37
6.1.1 Effective Mass Ratio Tables . . . . .	37
6.1.2 Mode Shapes . . . . .	39

6.2 Constant-Spin Modal Analysis Results . . . . .	42
6.2.1 Effective Mass Ratio Tables . . . . .	42
6.2.2 Discussion on Nutation Frequency . . . . .	44
6.2.3 Mode Shapes . . . . .	47
6.3 Prestressed Modal Analysis Results . . . . .	51
6.3.1 Discussion on Sagging . . . . .	52
6.3.2 Effective Mass Ratio Tables . . . . .	52
6.3.3 Mode Shapes . . . . .	54
<b>7 Conclusions and Recommendations</b>	<b>62</b>
<b>8 Appendices</b>	<b>66</b>
<b>9 List of Variables</b>	<b>84</b>

## 1. Abstract

This report presents the structural and dynamic analysis of a large-scale spacecraft model developed to simulate space domain awareness operations in a laboratory environment. The spacecraft structure is evaluated through finite element modeling to characterize the vibrational behavior under various operational conditions. Modal analyses are conducted to determine natural frequencies and mode shapes, both in a free-rotation configuration and under constant spin at 1 rad/s to simulate slow operational rotation. A static structural analysis is also performed to incorporate prestress effects arising from gravitational loading and nominal thrust maneuvers, followed by a prestressed modal analysis. Results revealed that the dominant coupled motion occurs between 9–14 Hz, primarily driven by flexure of the solar arrays. Constant-spin analysis demonstrates minimal gyroscopic coupling due to the low spin rate, resulting in modal behavior closely resembling the non-spinning configuration. Prestressing introduces significant changes in the lower modes, notably eliminating rigid body modes and increasing coupling between rotation and structural deformation. Recommendations are made regarding operational procedures to avoid excitation near critical modal frequencies. Overall, the analysis provides a comprehensive basis for predicting and mitigating dynamic behavior during experimental operations.

## 2. Acknowledgements

The progress made in the past two semesters on the Large-Scale Simulator would not be possible without the Space Domain Awareness team in the Space Domain Awareness team in the Space Systems Design Studio. First and foremost, Dr. Mason Peck provided incredible guidance throughout the entire project. Much of the progress made would not be possible without his insight, sparked by his rich experience in the industry. The mechanical subdivision of the Space Domain Awareness team includes Hannah Epstein, Juan Pelaez, Benjamin Gerard, and myself. Hannah Epstein is responsible for one of the proposed designs of the large-scale structure, denoted as ‘Custom Design I’ in this report. Her work is responsible for a large portion of the progress made on the structure over the past two semesters. Juan Pelaez is responsible for the lifting mechanism and mobile platform that one of the large-scale structures rests on. His work on integrating the structure to these mechanisms allows for the experimental conditions to be met. Benjamin Gerard works closely in conjunction with the structures team, as he is responsible for the propulsion system within the testbed. His communication is necessary for proper integration of components into the structure. Furthermore, Dr. Rajesh Bhaskaran contributed to the Space Domain Awareness team through his valuable insight into finite element analysis. Communication with Dr. Bhaskaran is essential to ensuring the modal analysis yields a dynamical behavior consistent with the behavior displayed under experimental conditions.

### 3. Introduction

Space Domain Awareness (SDA) involves understanding nearby resident space objects and inferring their intent to inform tactical decision-making through spacecraft autonomy or human command systems. Some key objectives for space domain awareness include: detection of resident space objects, predict atmospheric entry, predict interference in operations, and discriminate objects in the context of missile defense. The ability of the large-scale simulator to mimic a cislunar space environment is the critical performance metric of this project. Thus, the following requirements are created to ensure the structure fits that of a space-like environment:

#### 3.1 Requirements

- 45 degrees of rotational freedom from air bearing in all directions
- Flight-like appearance
- Cone of view for star tracker
- Support all components and fit all components within structure
- Spacecraft is below 1000 kg, including all components

As the large-scale structure is mounted on a semi-spherical air bearing, it is impossible to achieve full rotational freedom without interfering with the lifting mechanism. The first requirement is dependent upon the star tracker system. Considering a rotational freedom of 45 degrees in each axis orthogonal to the vertical axis in tandem with the existing 90 degree field of vision on the star tracker yields a complete 180 degree field of vision for the integrated system. Sweeping this profile along the vertical axis, from which the structure is free to rotate about, yields a full field of vision in the high bay. This is crucial to the success of the space domain awareness simulator as LED lights are displayed on the walls of the high bay in proportion to preexisting constellations. The star tracker uses these LED lights to discern the orientation of the satellite relative to previously known positions. Flight-like geometry helps ensure realistic center of mass, moments of inertia, and dynamic behavior during attitude control simulations or vibration testing. A solar array is included in the design of the structure to maintain a flight-like appearance. However, it should be noted that this solar array is not functional nor is it deployable as it is in the best interest of the attitude control team for the structure to behave as rigidly as possible. The cone of view for the star tracker is established through two methods: requiring 45 degrees of rotational freedom and prohibiting any structural components within the design to interfere with the cone of view. The star tracker is housed on the bearing plate of the inner structure, which serves as the rotational center of the large-scale structure. Thus, it is necessary to avoid any structural linkages or mechanical components in the cone

of view, present in the top half of the structure. The spacecraft must also be capable of housing all components within the structure. These components include a cold-gas propulsion system, four control-moment gyros, a high performance IMU, a star tracker, and onboard electronics. Furthermore, the structure must house a proper mechanism that can integrate with the lifting system. Finally, the satellite model must be less than 1000 kg, including the aforementioned components. This requirement is driven by the maximum loading capacity of the air bearing, considering a safety factor.

### 3.2 Trade Study

Four designs are considered to meet the requirements discussed above. In each of the four designs, composite honeycomb panels are mounted on each side panel to resist shear forces inherent in typical experimental conditions. To mitigate the cost of machining these panels, a bus profile of 5 by 5 by 4 feet (length  $\times$  width  $\times$  height) is established. This profile assures the full profile of the commercial-off-the-shelf (COTS) honeycomb panel is utilized in the design. Furthermore, the design of the solar wing is constant throughout each of the four designs. As the solar array is not functional, the wings comprise of a simplistic, rigid arm connected to a 4 by 4 foot thin sheet of aluminum. It should be noted that the design of the solar array is subject to change due to experimental outcomes. For example, if an interceptor requires a more elliptical path in relation to the chief, the solar wing may have to be cut down to avoid interference with the high bay walls. Furthermore, the solar array geometry influences the mode shapes of the entire structure. If these mode shapes are found to effect the structure during experimentation, alteration of the solar array can be discussed as a potential mitigation technique. This is discussed further in the results section. As the outer structure and solar array remains fixed during this trade study, an effective envelope is created to visualize the space the translationally stationary model can possibly occupy. By creating this model in the context of the high bay, the maximum profile of the mobile platform model is established. These profiles can be found in Appendix M. Finally, a bumper profile is established independent of each design. This bumper is fabricated to ensure the lifting mechanism collides with this component before any inner structure beam or other subsystem. This bumper profile comes into contact with the lifting mechanism at the rotational threshold of 45 degrees, ensuring safety of the inner components. For all design renderings in this section, the optimal shading options are chosen for maximum visibility.

#### 3.2.1 COTS Design

By leveraging commercial off-the-shelf (COTS) components in the design, manufacturing time, cost, and technical risk are significantly decreased. COTS parts typically come with documentation, support, and standardized interfaces, making them easier to integrate and replace. The COTS design explores the benefit of COTS parts to the fullest capability, as the only custom parts used are the bumper for the spherical air bearing and

the plate that connects to the spherical air bearing. Each beam member is comprised of 80/20 aluminum, while each joint member is compatible with 80/20 geometry, as sourced from McMaster-Carr. Joint brackets are mounted on the base of the spherical air bearing plate to a square cross section, ensuring the star-tracker field of view. This cross section is then connected via joint bracketry to the top section of the spacecraft. This geometry in particular, driven by the need of COTS parts, complicates the load paths of the structure. The load path from the bearing plate to the top profile of the structure is impeded by the intermediate profile, creating a disconnect between the top profile and the mid-plane. Furthermore, the use of joint brackets is not optimal for rigidity, as it assumes an inextensible mechanism is present at the location of that particular node. Also, the geometry of the satellite bus, derived in the previous section, is not conducive to a simple truss structure beneath the honeycomb panels. As brackets and mounts for 80/20 members are designed at fixed angles (30, 45, 60 degrees), redundant bracketing is necessary for a full COTS truss design, as seen in Figure 2 and 3. This is not only inefficient structurally, but also impedes the manufacturing process and drives cost up unnecessarily.

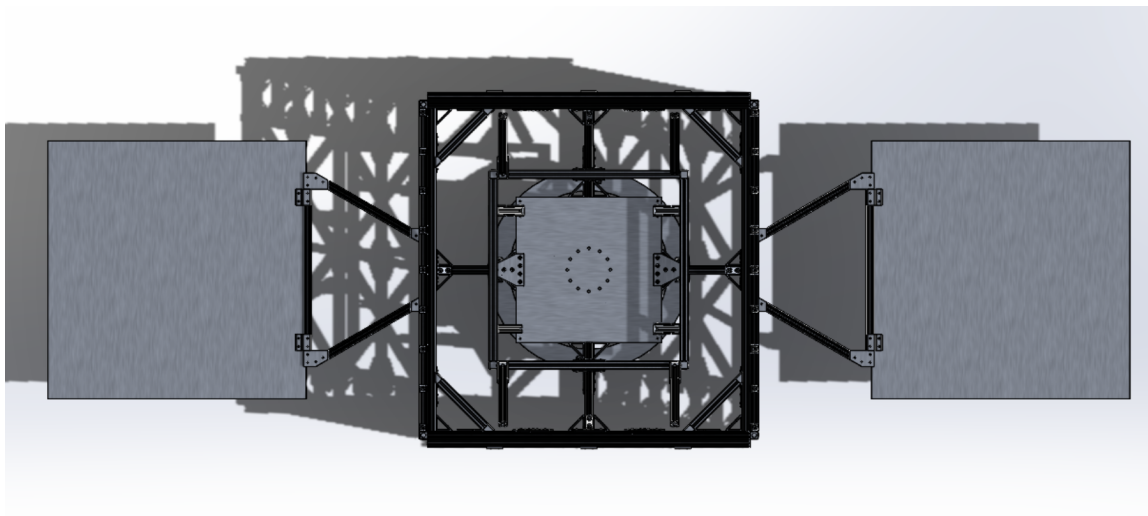


Figure 1: COTS Design Top View

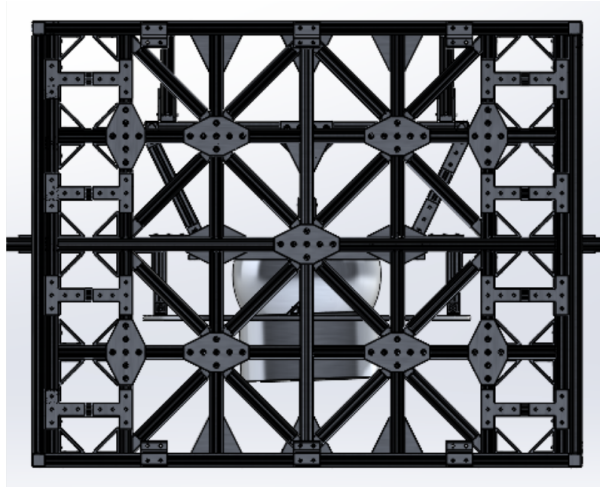


Figure 2: COTS Design x-z Plane

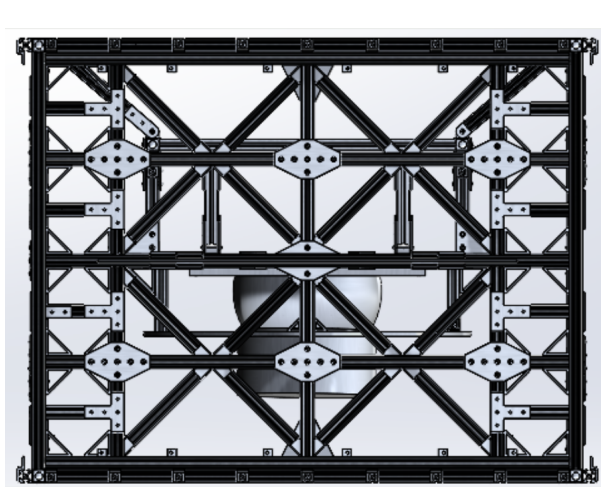


Figure 3: COTS Design y-z Plane

### 3.3 Custom Design I

The following custom designs aim to mitigate the amount of unnecessary parts in the COTS Design. The panels on the outside of the structure are assumed to be capable of handling large amounts of shear loading as they are derived from a honeycomb composite. Thus, the truss sections on the side profiles of the structure are simplified to a singular intersection between members at the midpoint of each conjoining profile, negating much of the ability of these members to resist shear forces. It should be noted that the main purpose of these members is component mounting; therefore, they are subject to change. For the sake of the trade study, the simplified side profile structures are considered.

Custom Design I is comprised of the bearing plate, bumper, top and bottom ring profiles, and connecting members. The bottom ring profiles is sized according to the requirement of 45 degrees of rotational freedom while the top ring profile is sized according to the star tracker cone of view and former requirement. The members extend from the midpoints of the bearing plate to the points at which the top ring meets the outer structure top profile. The bumper plate is then connected by its corner nodes vertically to the bearing plate, which is connected to the bottom profile in the same manner that the bumper plate is connected to the top ring. Custom Design I is one rigid part. The advantages and disadvantages of this design choice will be discussed later in this section. The only custom parts included in this design are the panel mounts that connect the top and bottom rings to the outer structure of the satellite model.

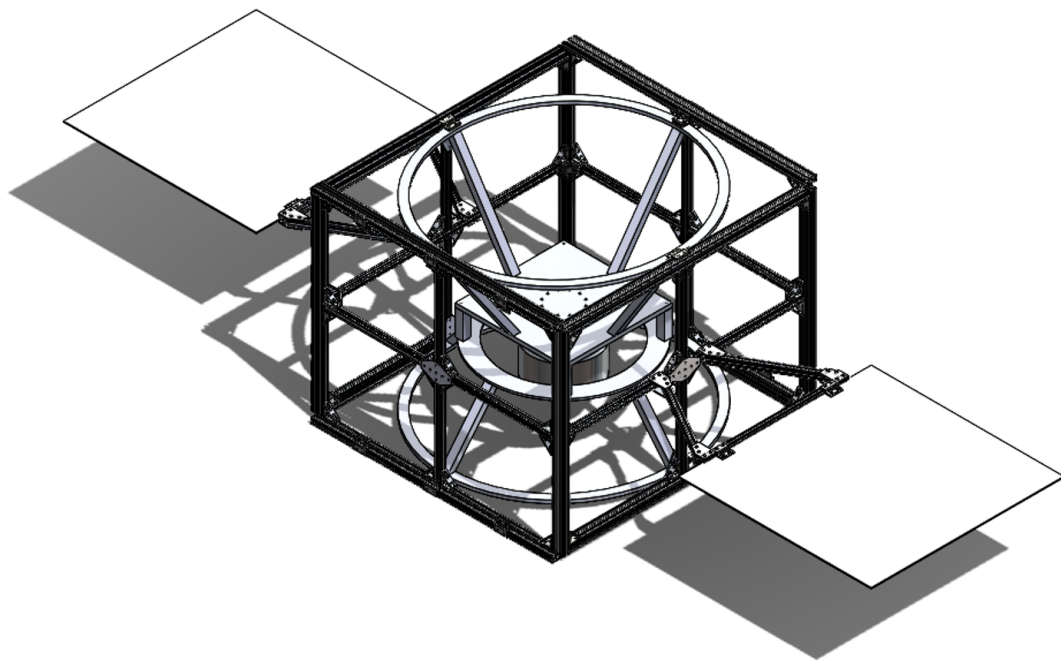


Figure 4: Custom Design I Isometric View

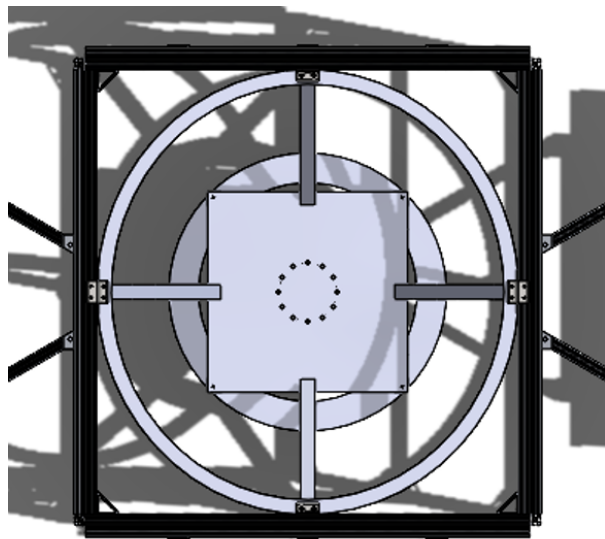


Figure 5: Custom Design I Top View

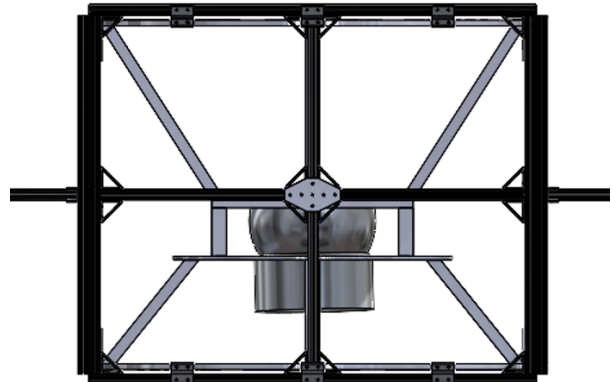


Figure 6: Custom Design I Side View

### 3.3.1 Custom Design II

The second custom design provides an internally rigid geometry, similar to the first custom design. However, while the first custom design includes a fully custom inner structure, this design incorporates COTS parts, most notably the 80/20 aluminum beams.

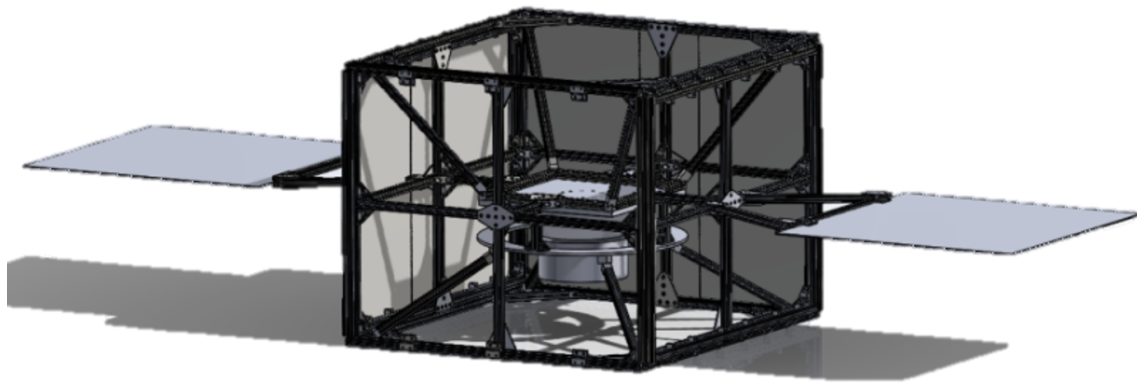


Figure 7: Custom Design II Isometric View

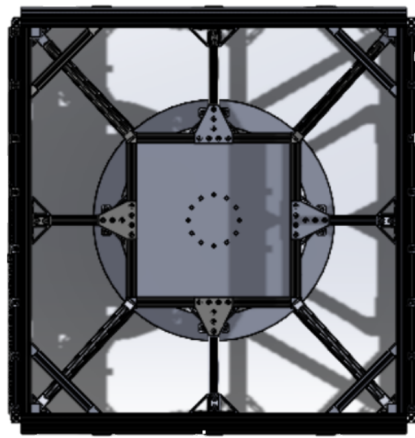


Figure 8: Custom Design II Top View

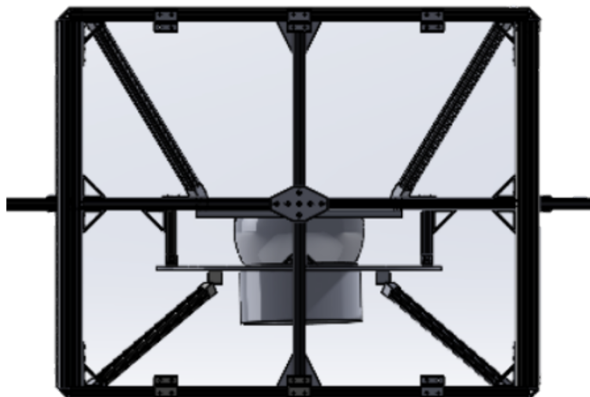


Figure 9: Custom Design II Side View

To properly integrate the 80/20 beams within the inner structure, the following parts are designed:

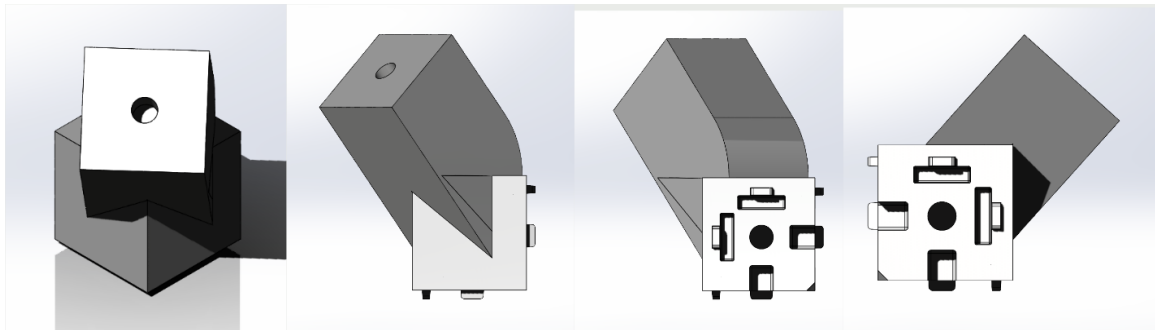


Figure 10: Custom Part I

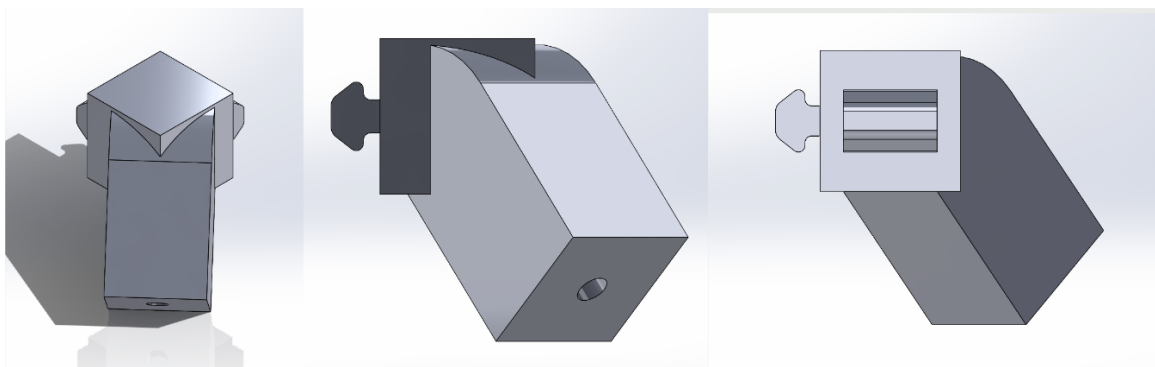


Figure 11: Custom Part II

The first custom part is created for mounting the bumper and bearing plate to the 80/20 beams, while the latter of the two is created to connect at the corner nodes of the outer structure. It is crucial to note that while there are only two custom designed parts, the angles of the plane at which the connection to the 80/20 beam is extruded varies for two conditions. These angle variations are most clear in Figure 9. The geometry of the inner structure of Custom Design II also varies to Custom Design I in the respect of connecting corner nodes rather than nodes along the halfway point of beams. This effectively maximizes the moment arm of any lateral force acting on the outer structure, which is then transferred to the inner structure. The only external lateral forces that act on the satellite are those of the thrusters, capable of 2.5 N pulses. This effect is mitigated through the diagonal braces on the top and bottom profiles of the outer structure, visible most clearly in Figure 8. Additionally, Custom Design II is braced using the horizontal bars connecting the bearing plate to the outer structure along the mid-plane.

### 3.3.2 Custom Design III

Custom Design III is a fully custom design, similar to Custom Design I. While Custom Design I is comprised of one rigid inner structure, Custom Design III consists of 49 custom parts. The first custom part is an edited version of the bearing plate for the mounting

of the spherical air bearing. The full drawing of this part can be found in Appendix A. Compared to the original design of the bearing plate, this design includes a central cutout for integration of the star tracker. From a top view, the cone of view for the star tracker is visible. Furthermore, wedge profiles are included to properly angle the linkages to the connection nodes on the top profile of the structure. Similar to Custom Design II, a diagonal approach for node connection is included to allow for maximal component integration volume. However, the effect of the longer moment arm is mitigated by implementing an isogrid on the top and bottom profiles of the outer structure. This isogrid includes a circular cutout that allows for 45 degrees of rotational freedom. To integrate the top and bottom isogrid to the inner structure, custom wedge parts are designed, each with a different angle of inclination. These wedges integrate with the isogrid via a connection of 8 nuts and bolts in a circular profile. The wedge is then attached to a rod connection component by 3/4 - 16 bolts. Two perpendicular nut and bolt configurations secure each rod into the connection pieces. It should be noted that the rod ends a quarter inch before the bottom profile of the connection piece. In fabrication, this area will be filled with a spring to pre-tension the inner structure. In Appendix H, the custom part for the connection between the bumper piece and the bottom isogrid is shown. As seen, the wedge component is extruded laterally from the bumper connection to ensure the wedge does not come into contact with the lifting mechanism before the bumper itself. An isometric, top, and side view of Custom Design III is shown below:

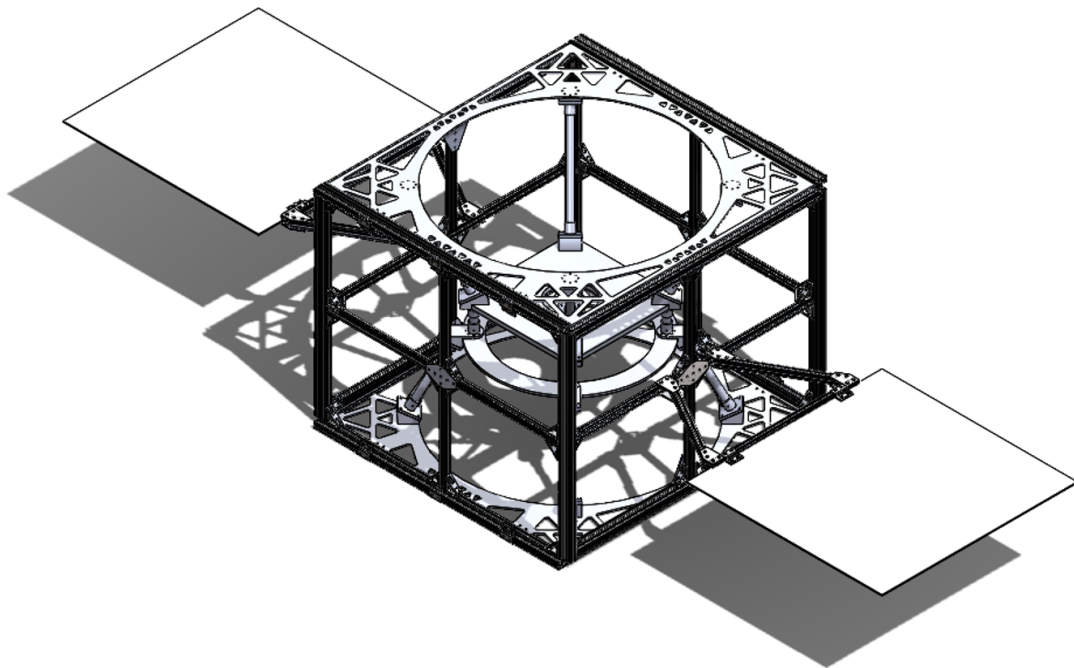


Figure 12: Custom Design III Isometric View

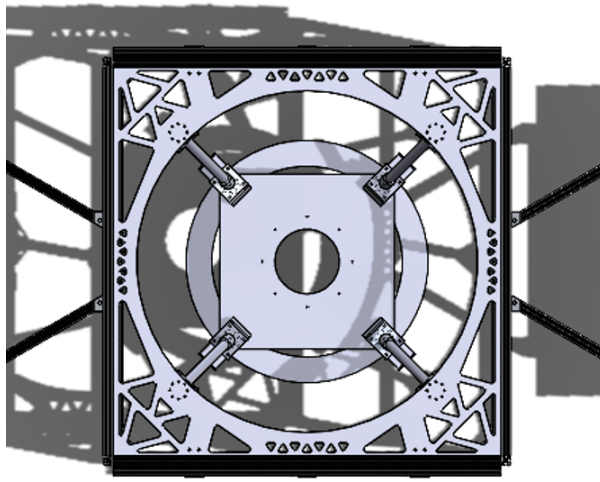


Figure 13: Custom Design III Top View

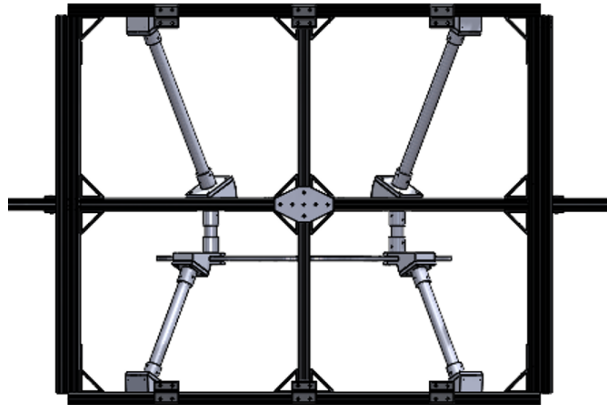


Figure 14: Custom Design III Side View

### 3.4 Comparison of Designs

In Solidworks Mechanical, Aluminum-6065 is assigned as the material for all parts in each design. Using the ‘Mass Properties’ function, the Table below is derived:

Table 1: Comparison of COTS, Custom Design I, Custom Design II, and Custom Design III

Design	Mass (kg)	Volume ( $\text{m}^3$ )	Surface Area ( $\text{m}^2$ )	Principal Inertia Matrix ( $\text{kg}\cdot\text{m}^2$ )
COTS	236.57	0.24	104.36	$\begin{bmatrix} 92.86 & 0 & 0 \\ 0 & 164.91 & 0 \\ 0 & 0 & 205.61 \end{bmatrix}$
Custom I	193.9	0.19	74.48	$\begin{bmatrix} 71.18 & 0 & 0 \\ 0 & 140.63 & 0 \\ 0 & 0 & 168.94 \end{bmatrix}$
Custom II	182.12	0.18	79.46	$\begin{bmatrix} 62.92 & 0 & 0 \\ 0 & 139.45 & 0 \\ 0 & 0 & 163.11 \end{bmatrix}$
Custom III	191.64	0.10	30.59	$\begin{bmatrix} 81.54 & 0 & 0 \\ 0 & 312.34 & 0 \\ 0 & 0 & 285.38 \end{bmatrix}$

In the table above, we compare the mass, volume, surface area, and the principal inertia matrix for each of the three designs previously discussed. It is important to note that the volume displayed in the table is the effective volume of the sum of all parts, and not the total volume of the geometry itself. Thus, the effective volume available for the

other spacecraft components is verified through an independent geometrical analysis. The principal moments of inertia are used mainly as a sanity check, as the intended spin direction of the spacecraft is in the z-axis direction.

Assuming a maximum component mass of 500 kg, all designs are in accordance with the mass requirement. Furthermore, all designs have their largest principal moment of inertia around the z-axis, which is desired in many experimental cases. As discussed in the ‘COTS Design’ section, the COTS design has structural redundancies which over-complicates the manufacturing process and drives cost up. The custom design approach mitigates these unnecessary members and provides a more desirable volume profile for the integration of components. First, consider Custom Design I. The inner structure of Custom Design I is one rigid part, which is optimal for structural stability. However, one part connecting four profiles on one vertical plane is exceedingly difficult to manufacture. The top and bottom ring profiles establish a definitive envelope for component integration. However, these rings connect to the top and bottom profiles at four tangent points, creating a disconnect between the inner structure and outer structure. Furthermore, the load path throughout the inner structure becomes complicated due to the need to connect the bumper to the bearing plate through the corner nodes. This creates a moment arm between this node and the one at which the top and bottom rings are connected to the inner structure. The creation of this moment arm leads the load path to travel through the ring profiles, which is less predictable. Custom Design II suffers from this same problem. The bearing plate connects to the top profile through corner nodes, as does the bumper to the bottom profile. However, the bumper is connected to the midpoints of the bearing plate, further complicating the load path. Custom Design II mitigates the need for custom member parts by designing joints that are compatible with 80/20 geometry. These joints are established at the corner nodes of the outer structure, which is useful in resisting tensile and compressive forces, but not as efficient in resisting shear forces. The custom joints connect flush with the 80/20 beams, fastened by a singular screw. This solution is not as robust as many connection techniques seen in industry. Custom Design III offers a more robust technique for connecting the inner structure to the outer structure. The isogrid in Custom Design III establishes an effective envelope for the integration of components while providing a full connection to the outer structure. The isogrid aids in resisting lateral shearing, and connects to the inner structure via a custom wedge piece. The wedge piece aids in manufacturing ease as it separates the connector piece and isogrid, avoiding unnecessary angular defect in the connector piece. Furthermore, Custom Design III requires 224 fasteners, increasing the resilience of each connection. Considering the requirements of the design and the trade-offs discussed above, Custom Design III is chosen to continue the project. As mentioned previously, the main purpose of the side profiles of the outer structure is mounting components. Included below is a figure of Custom Design III with a modified side profile to integrate the propulsion system of the large-scale simulator testbed:

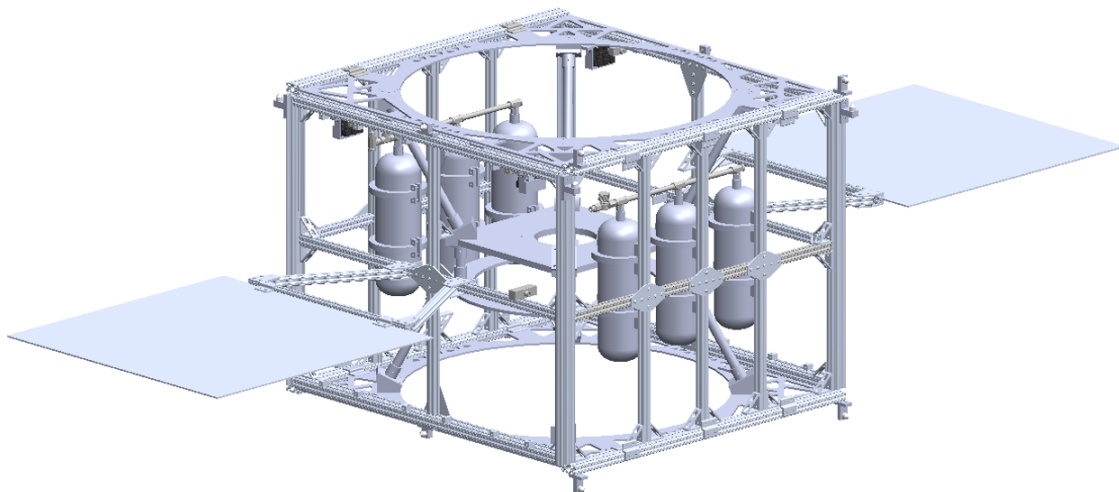


Figure 15: Custom Design III Including Propulsion System

## 4. Literature Review

This section focuses on the theory behind the computational methods inherent within the modal analysis of the satellite structure. A modal analysis determines vibrational characteristics of a structure. This includes both natural frequencies and mode shapes. Throughout the report, all analysis is performed using Ansys Modal. The dynamical response of any system is best understood as a superposition of modes. The equivalent stiffness of beam profiles is utilized in tandem with multi-degree-of-freedom systems to understand how these modes are derived.

The basis of Finite Element Analysis (FEA) is contingent upon equating structures to a collection of nodes and elements. Each node is considered to be a point mass with a network of springs (bars) joining them. To understand how these networks move multi-dimensionally, it is essential to know how a one-degree-of-motion spring mass system works. Hooke's Law states that the force  $F$  needed to extend or compress a spring by some distance  $x$  scales linearly with respect to that distance. This law can be extended to the tensional stress of a uniform and elastic bar where the length, area, and Young's modulus of the bar are represented by  $l$ ,  $A$ , and  $E$ , respectively. Knowing the tensile stress in the bar:

$$\sigma = \frac{F}{A}$$

and the definition of strain:

$$\varepsilon = \frac{\Delta l}{l}$$

Hooke's law can be expanded to represent a uniform and elastic bar:

$$\sigma = E\varepsilon$$

It follows that the change in length  $\Delta l$  can be expressed as:

$$\Delta l = \varepsilon l = \frac{Fl}{AE}$$

Hooke's law is often expressed using the convention that  $F$  is the restoring force exerted by the spring on the applied force at the free end. Defining the stiffness and displacement as  $k = \frac{AE}{l}$  and  $\Delta l = x$ , respectively. The equation for Hooke's Law becomes:

$$F = -kx$$

since the direction of the restoring force is opposite the spring displacement [5].

In multiple-degree-of-freedom systems, these components expand into matrices. In these systems, an eigenvalue based solution approach takes advantage of the symmetry within the mass and stiffness matrices. To derive an eigenvalue-based solution for calculating the natural frequencies and mode shapes in a computationally efficient way, the mass and stiffness are merged into one expression, denoted by the mass normalized stiffness  $\tilde{K}$ . First, assume that the all mass ( $M$ ) and stiffness ( $K$ ) matrices are symmetric and positive definite due to the physical nature of these matrices. Therefore,  $M$  can be factored into two terms using the Cholesky decomposition:

$$M = LL^T$$

For the unique case diagonal mass matrices the Cholesky decomposition ( $L$ ) is defined as:

$$L = M^{1/2} = \begin{bmatrix} \sqrt{m_1} & 0 \\ 0 & \sqrt{m_2} \end{bmatrix}$$

While a special case that is not always true, it is a commonly encountered mass matrix formulation due to the nature of mass matrices [6]. Moreover, the example considered

within this text all consists of a diagonal mass matrix. For the special case diagonal mass matrices, the equation factors into:

$$\mathbf{M} = \mathbf{M}^{1/2} \mathbf{M}^{1/2}$$

Moreover, the inverse of the diagonal matrix  $\mathbf{M}^{1/2}$  is denoted as  $\mathbf{M}^{-1/2}$  and defined as:

$$\mathbf{L}^{-1} = \mathbf{M}^{-1/2} = \begin{bmatrix} \frac{1}{\sqrt{m_1}} & 0 \\ 0 & \frac{1}{\sqrt{m_2}} \end{bmatrix}$$

Now, consider an equation of motion for an undamped 2-DOF system:

$$\ddot{\mathbf{M}\vec{x}} + \mathbf{K}\vec{x} = 0$$

This expression can be transformed into a symmetric eigenvalue problem. To perform this transform, we set  $\vec{x} = \mathbf{M}^{-1/2}\vec{q}$  and multiply the equation by  $\mathbf{M}^{-1/2}$  such that the EOM becomes:

$$\mathbf{M}^{-1/2} \mathbf{M} \mathbf{M}^{-1/2} \ddot{\vec{q}} + \mathbf{M}^{-1/2} \mathbf{K} \mathbf{M}^{-1/2} \vec{q} = 0$$

As  $\mathbf{M}^{-1/2} \mathbf{M} \mathbf{M}^{-1/2}$  is equal to the identity matrix  $\mathbf{I}$  and defining  $\mathbf{M}^{-1/2} \mathbf{K} \mathbf{M}^{-1/2}$  as the mass normalized stiffness  $\tilde{K}$  yields the simplified expression:

$$\ddot{\mathbf{I}\vec{q}} + \tilde{K}\vec{q} = 0$$

where  $\tilde{K} = \mathbf{M}^{-1/2} \mathbf{K} \mathbf{M}^{-1/2}$  is equivalent to the expression  $k/m$  from the 1-DOF system as the are both mass-normalized stiffness values.

A solution is found by assuming a solution, taking the derivatives of the solution, and substituting it into the equation of motion. Following these steps and assuming a solution of:

$$\vec{q} = \mathbf{v} e^{j\omega t}$$

where  $\mathbf{v}$  is an  $n \times n$  matrix for a system with  $n$  degrees of freedom. Adding this assumed solution to the equation of motion results in the form:

$$-\mathbf{v}\omega^2 e^{j\omega t} + \tilde{K}\mathbf{v} e^{j\omega t} = 0$$

driving out the nonzero scalar  $e^{j\omega t}$  and rearranging the above expression results in:

$$\tilde{K}\mathbf{v} = \omega^2\mathbf{v}$$

Knowing that  $\mathbf{v} \neq 0$ , as a matrix of zeros would mean no motion is present in the system, this equation can be expressed in a typical eigenvalue formulation:

$$\tilde{K}\mathbf{v} = \lambda\mathbf{v}$$

where  $\mathbf{v}$  is a column matrix made up of the eigenvectors  $\mathbf{v} = [v_1, v_2, \dots, v_n]$  and  $\lambda$  is a square matrix with eigenvalues on the diagonal. As  $\mathbf{K}$  is symmetric, this is a symmetric eigenvalue problem [6].

This is the basis of every computational method for solving multi-degree-of-freedom system. However, the efficiency of a modal substructuring method depends on the component modes used to reduce the subcomponent models. Several model reduction techniques are commonly used in finite element analysis (FEA) to decrease computational cost while preserving essential system dynamics, including Guyan reduction, modal decoupling, and the Craig-Bampton method. Modal decoupling is based upon the theory discussed above, as the approximate system behavior depends solely on the eigenvectors of the solution, or physically, the mode shapes. This method retains key dynamic characteristics, particularly for low-frequency modes, but can lose accuracy for responses outside the captured modal bandwidth. Guyan reduction, or static condensation, simplifies a system by assuming the inertial effects of non-primary degrees of freedom are negligible, allowing these to be expressed as static functions of the retained degrees of freedom. The Guyan reduction can poorly capture dynamic behavior, as at higher frequencies, the mode shapes are neglected. This reduction is typically used when computational power is a choking requirement. The Craig-Bampton reduction combines elements of both approaches by explicitly keeping boundary degrees of freedom and reducing interior dynamics using a mix of constraint modes and selected vibration modes. As a result, Craig-Bampton offers a better balance between accuracy and efficiency, especially for structures that interface with other systems, and is widely preferred for problems involving component mode synthesis and coupled dynamic simulations [12] [8] [9].

As the Craig-Bampton method allows for different boundary conditions while allowing for the problem size to be reduced, it is chosen for the modal analysis and included in Ansys FEA. The classical Craig-Bampton method is inherently a linear model reduction technique, developed under the assumption that the mass and stiffness matrices of the system are constant and independent of the system's deformation state [8]. In the linear Craig-Bampton formulation, the structural behavior is captured through a combination of static constraint modes and fixed-interface normal modes, enabling efficient dynamic analysis while preserving the boundary conditions. However, when geometric nonlinearities or material nonlinearities become significant, the assumptions underlying the linear

Craig-Bampton method are no longer valid. In such cases, a nonlinear extension of the Craig-Bampton method is required [9]. The nonlinear Craig-Bampton approach adapts the reduction process by either updating the modal basis during the simulation or projecting nonlinear internal forces onto the reduced space at each time step. This allows the reduced-order model to account for nonlinear stiffness, displacement-dependent mass properties, and other state-dependent effects. While nonlinear Craig-Bampton models provide improved accuracy for large deformation problems, they introduce increased computational complexity and typically require hyper-reduction techniques to remain tractable for practical simulations. The satellite testbed is not subject to large deformations, and all materials used in the model are not plastic under environmental conditions. Therefore, a linear Craig-Bampton model is chosen for modal analysis of the large-scale model.

Ignoring damping, the equation of motion for a given multi-degree-of-freedom system is as follows:

$$[M_{u_d}] \{ \ddot{u}_d \} + [K_{u_d}] \{ u_d \} = \{ F(t) \}$$

The Craig-Bampton transform is applied to the equation of motion, defined as:

$$\{ u_d \} = \begin{Bmatrix} u_b \\ u_\ell \end{Bmatrix} = \begin{bmatrix} I & 0 \\ \phi_r & \phi_\ell \end{bmatrix} \begin{Bmatrix} u_b \\ q \end{Bmatrix}$$

Combining the Craig-Bampton transformation and pre-multiplying by  $\phi_{cb}^T$ , the following is obtained:

$$\phi_{cb}^T [M_{u_d}] \phi_{cb} \begin{Bmatrix} \ddot{u}_b \\ \ddot{q} \end{Bmatrix} + \phi_{cb}^T [K_{u_d}] \phi_{cb} \begin{Bmatrix} u_b \\ q \end{Bmatrix} = \phi_{cb}^T \begin{Bmatrix} F_b \\ F_\ell \end{Bmatrix}$$

It is useful to define the mass and stiffness matrices as:

$$[M_{cb}] = \phi_{cb}^T [M_{u_d}] \phi_{cb} = \begin{bmatrix} M_{bb} & M_{bq} \\ M_{qb} & M_{qq} \end{bmatrix}$$

$$[K_{cb}] = \phi_{cb}^T [K_{u_d}] \phi_{cb} = \begin{bmatrix} K_{bb} & 0 \\ 0 & K_{qq} \end{bmatrix}$$

Furthermore, the following definitions are used to simplify the model:

$$\begin{bmatrix} M_{bb} & M_{bq} \\ M_{qb} & M_{qq} \end{bmatrix} \begin{Bmatrix} \ddot{u}_b \\ \ddot{q} \end{Bmatrix} + \begin{bmatrix} K_{bb} & 0 \\ 0 & K_{qq} \end{bmatrix} \begin{Bmatrix} u_b \\ q \end{Bmatrix} = \begin{Bmatrix} F_b \\ 0 \end{Bmatrix}$$

where input forces are applied at the boundary conditions ( $F_\ell = 0$ ).

The boundary mass matrix is compiled through the total mass properties confined to the boundary points:

$$[M^*] = \phi_{\ell b}^T [M_{u_d}] \phi_{\ell b}$$

While the interface stiffness matrix is obtained by displacing one boundary degree of freedom while the others remain fixed. If the system is non-redundant:

$$K_{bb} = 0$$

Typically, the mode shapes are mass normalized. This separates the conjunction between the eigenvectors and eigenvalues of the solution. Using this method:

$$K_{qq} = \begin{bmatrix} \lambda & 0 \\ 0 & \lambda \end{bmatrix}, \quad \lambda_i = \frac{k}{m_i} = \omega_i^2$$

$$M_{qq} = \begin{bmatrix} I & 0 \\ 0 & I \end{bmatrix}$$

Including damping, the equation of motion including the Craig-Bampton method becomes:

$$\begin{bmatrix} M_{bb} & M_{bq} \\ M_{qb} & I \end{bmatrix} \begin{Bmatrix} \ddot{u}_b \\ \ddot{q} \end{Bmatrix} + \begin{bmatrix} 0 & 0 \\ 0 & 2\zeta\omega \end{bmatrix} \begin{Bmatrix} \dot{u}_b \\ \dot{q} \end{Bmatrix} + \begin{bmatrix} K_{bb} & 0 \\ 0 & \omega^2 \end{bmatrix} \begin{Bmatrix} u_b \\ q \end{Bmatrix} = \begin{Bmatrix} F_b \\ 0 \end{Bmatrix}$$

In summary, the linear Craig-Bampton method provides a substantial framework for structural analysis of the large-scale model. By defining the system through reduced-order mass and stiffness matrices, the dynamical problem is solved while reducing complexity of the system. The explicit retention of boundary degrees of freedom offers a clear mechanism to apply boundary conditions or interfacing with other structural components, which is necessary given the component integration in the modal analysis. Furthermore, this is necessary for studying the testbed in experimental conditions, where the structure is subject to the external forces of the propulsion system [12]. Furthermore, the Craig-Bampton transformation enables the reconstruction of physical displacements and responses from the reduced solution space. This ensures that the reduced model remains directly interpretable in physical terms.

## 5. Methodology and Experimental Details

This section discusses the methodology and experimental details of the modal analysis. The objective of the modal analysis is to properly extract the dynamical behavior of the large-scale structure in experimental conditions. To achieve this, an experimental setup which correctly bounds the physics of the model is necessary. In this report, two methods are explored: a pure modal analysis with free rotation and a static structural model used in tandem with modal analysis.

### 5.1 General Meshing Practices

In both approaches, the same mesh is used to ensure accuracy between the models. In ANSYS Mechanical, several meshing techniques are available to balance computational efficiency and solution accuracy. The ‘Patch Conforming’ method is the default for complex three-dimensional geometries, generating predominantly tetrahedral elements that conform closely to the surface topology. It offers high robustness in handling intricate or organic shapes but can result in a large element count and lower solution accuracy per element compared to structured meshes. The Patch Independent method, alternatively, treats the geometry more flexibly, allowing meshing to proceed even when small features or imperfections would otherwise cause failure. While this increases meshing success rates for highly complex CAD models, it can sacrifice local geometric detail. Sweep meshing is employed for bodies with a natural extrusion or revolution characteristic, producing structured hexahedral elements along a defined path. Similarly, Hex Dominant meshing attempts to fill the interior with hexahedral elements wherever possible, falling back to tetrahedra where necessary. This technique offers a compromise between mesh quality and automatic meshing robustness. In the context of the large-scale structure, this method is useful for parts with a circular cutout, such as the bearing plate. For two-dimensional and surface-based structures, Mapped Face Meshing can generate highly structured quadrilateral meshes, providing excellent performance for thin shell and plate models but requiring clean, square-like surface topology to succeed. Thus, this technique is unnecessary for the complex geometry inherent within the structural model. Overall, while tetrahedral meshes offer the greatest automatic meshing flexibility, structured hexahedral and quadrilateral meshes provide superior convergence rates and solution accuracy.

To begin the meshing process, first consider the outer structure of the model. The profile of the 80/20 beams used for the outer structure of the model contain complex geometry, as seen below:



Figure 16: 80/20 Beam Element Front Profile

To properly mesh this geometry, a swept tetrahedral approach is used with patch independent conforming method. This ensures that the curves of the profile are properly subdivided with enough accuracy. The honeycomb panels are also subdivided using a tetrahedral mesh. The honeycomb panel regions, despite their inherently hexagonal internal architecture, were also meshed using a tetrahedral scheme. A hex-dominant meshing approach was evaluated but found to be inefficient for these regions, as it tended to generate elements extruded laterally through the thickness of the panels, leading to poor aspect ratios. The solar array support structures, composed of 80/20 aluminum framing, were meshed similarly using swept tetrahedral elements to capture their slender geometry. In contrast, the solar panels themselves are modeled as thin planar surfaces. These are divided using a mapped quadrilateral mesh, optimizing element quality and reducing computational cost compared to an unstructured triangular discretization.

As discussed in the literature review, a multi-degree-of-freedom spring–mass system is analyzed through an eigenvalue formulation. In finite element analysis (FEA), structures are discretized into a network of nodes and elements, necessitating the solution of the eigenvalue problem at each nodal degree of freedom. When meshing the full satellite assembly with all subsystem components included, even the coarsest available meshing strategy results in a model exceeding 1.5 million nodes. This nodal density exceeds the available computational resources, rendering direct simulation impractical. Consequently, geometry simplification is employed as a standard model reduction strategy to mitigate the number of elements and associated degrees of freedom. It is critical that such simplifications preserve the overall mass distribution and stiffness characteristics of the system, as the modal behavior of large-scale structures is governed primarily by these properties rather than fine geometric detail.

In the context of the project, the primary goal of geometric simplification is to decrease the amount of elements within the range of computational power available while retaining the large-scale geometry. To begin the simplification, the profile of the 80/20 beams is reduced to a square, 1.5 inch by 1.5 inch profile. This reduces the need for a tetrahedral mesh instilled on the beams. The primary driver of fine mesh elements in the structure is joint geometries, including small hole diameters for nut and bolt connections as well as

threaded holes for bolt connections. These geometries are suppressed, as an equivalent connection can be established in Ansys Workbench using contact regions. Furthermore, the inner honeycomb geometry in the side panel structure is suppressed as this configuration can be achieved using an equivalent material stiffness. Using these approaches, the entire outer structure can be modeled as one part with contact regions, significantly decreasing the computational power required to run the analysis. The inner structure remains a full assembly with 49 custom components. The inner structure is simplified by suppressing the connection geometries. The top and bottom isogrid geometries are the same as the fully detailed structure as it is responsible for resisting much of the shear forces.

The sub-assemblies also contain complex geometry. For example, the control moment gyroscope (CMG) assembly contains over 250 components, many of which require precise meshing. Additionally, the propulsion system includes tubing, the geometry of which changes depending on the orientation of the satellite model. Thus, all sub-assemblies are simplified into lump masses. A custom material for the CMG assembly is defined in Ansys using isotropic material properties. The isotropic properties of structural steel are used for the CMG assembly, including a Young's Modulus of 200 GPa and a Poisson's Ratio of 0.33. A density block is also placed into the custom material, where the density of water is used as a general approximation for the sub-assembly. While this is a good approximation for the CMG subassembly, it is not used for the propulsion system, as the tanks are pressurized, yielding a different density parameter. This parameter is found using the mass properties of the propulsion system, derived by Benjamin Gerard. A screenshot of the Ansys 'Experimental Data' page is shown below to detail the process of creating and assigning a custom material:

	Contents of Engineering Data	Source	Description
1	Material		
2	Aluminum Alloy	Ger	General aluminum alloy. Fatigue properties come from MIL-HDBK-5H, page 3-277.
4	Custom_Material	Ger	
5	Structural Steel	Ger	Fatigue Data at zero mean stress comes from 1998 ASME BPV Code, Section 8, Div 2, Table 5-110.1
*	Click here to add a new material		
1	A	B	C
2	Property	Value	Unit
1	Material Field Variables	Table	
2	Density	998	kg m^-3
4	Isotropic Elasticity	Young's Modulus and Poisson...	
5	Derive from	Young's Modulus and Poisson...	
6	Young's Modulus	2E+11	Pa
7	Poisson's Ratio	0.3	
8	Bulk Modulus	1.6667E+11	Pa
9	Shear Modulus	7.6923E+10	Pa

Figure 17: Custom Material creation in Engineering Data Index

The final suppressed geometry is imported into Ansys Modal initially. The proper connections are established between coincident faces in the model. The custom materials are assigned to the CMG and propulsion sub-assemblies, respectively. Ansys generates an initial coarse mesh for the model, which is shown below. To properly refine the mesh, a mesh convergence study is performed.

## 5.2 Mesh Convergence Study

Mesh convergence is a fundamental component of finite element analysis (FEA) and is critical for establishing the accuracy and validity of numerical simulation results. As the discretization of the domain is refined through the reduction of element size, the numerical approximation of the solution is expected to asymptotically approach the true, continuous solution of the governing physical equations. A mesh convergence study involves systematically refining the mesh and tracking a quantity of interest to verify that further refinements yield diminishing changes in the computed results. In the context of this project, the quantity of interest is the maximum displacement in the tenth mode shape of the free-free modal analysis. As the first six mode shapes in the free-free analysis are the rigid body modes, we neglect these, effectively making the tenth mode shape the fourth mode shape. This mode shape is chosen in particular as the maximum displacement occurs at two nodes, rather than along an edge or throughout a body. Additionally, the solar wings act as cantilever beams protruding from the satellite bus. Thus, the solar wings significantly contribute to the dynamical behavior of the large-scale structure. In the tenth mode shape, the maximum displacement occurs on the corners of the solar panels, making it an effective shape to consider for mesh convergence. To begin this study, a coarse mesh is established on the solar panels using the face sizing tool, with a global element size of 0.25 m. This element size is reduced  $\sim 50\%$  in each step size of the mesh convergence study. A quadrilateral refinement approach would lead to a smoother mesh convergence curve as the elements uniformly substructure the solar panels. However, due to the geometry refinement discussed above, the solar panels must be subdivided through a tetrahedral approach as they are connected to the satellite bus as one geometry. Thus, the mesh convergence is dependent solely on the element sizing of the solar panels. The tenth mode shape and corresponding displacement values and frequencies are shown below:

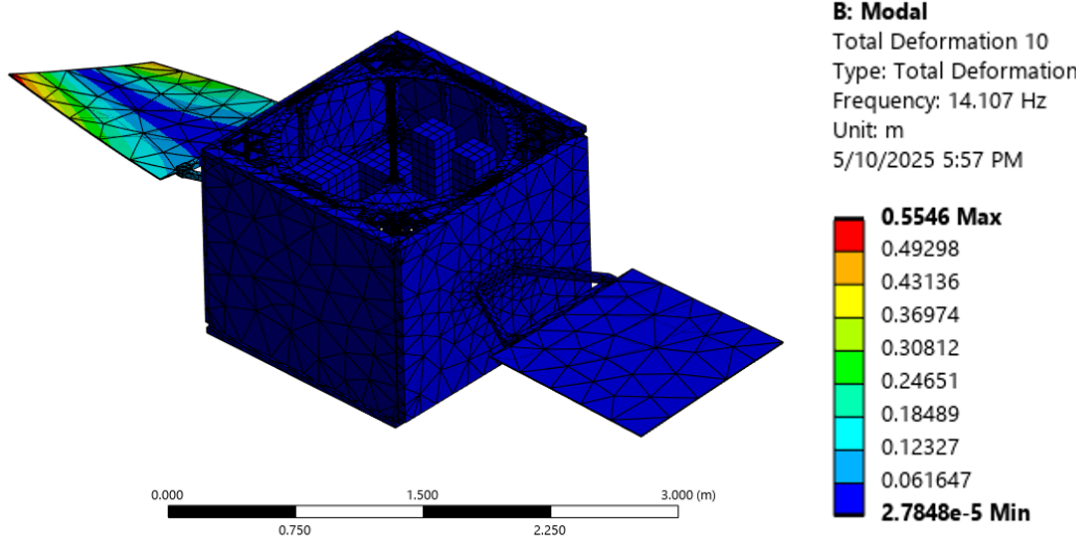


Figure 18: 0.25 Meter Element Size Mesh Results

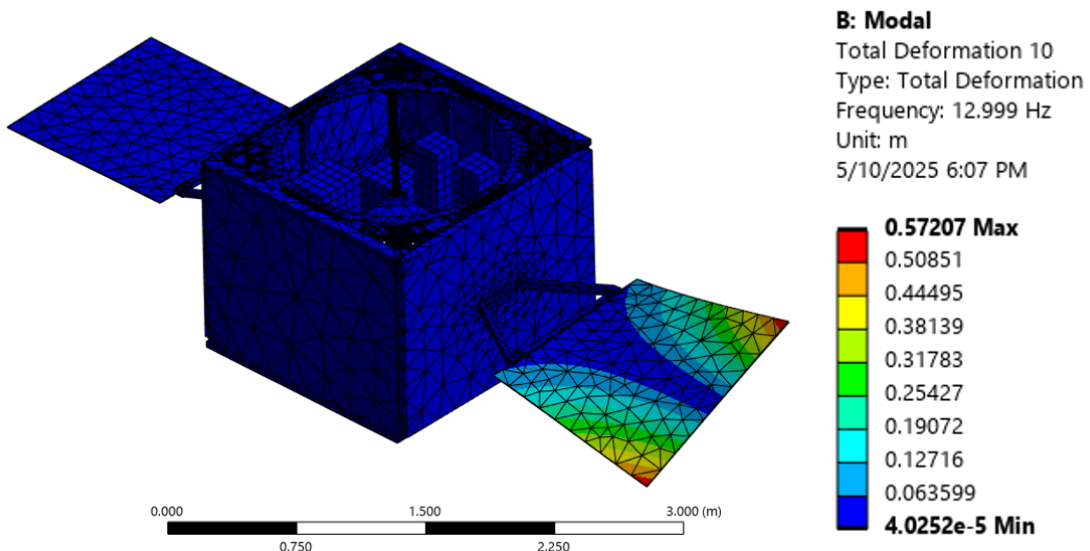


Figure 19: 0.125 Meter Element Size Mesh Results

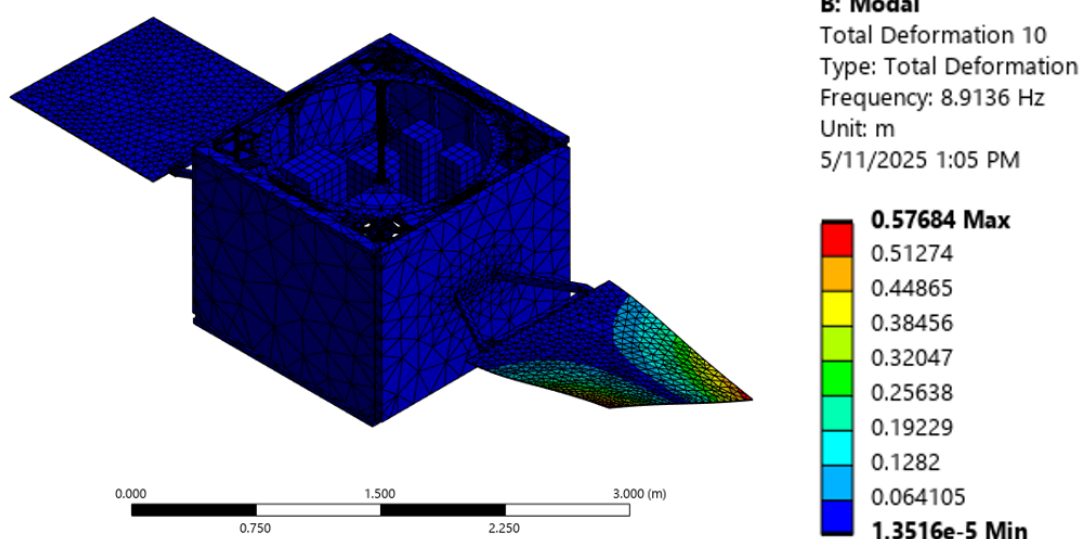


Figure 20: 0.06 Meter Element Size Mesh Results

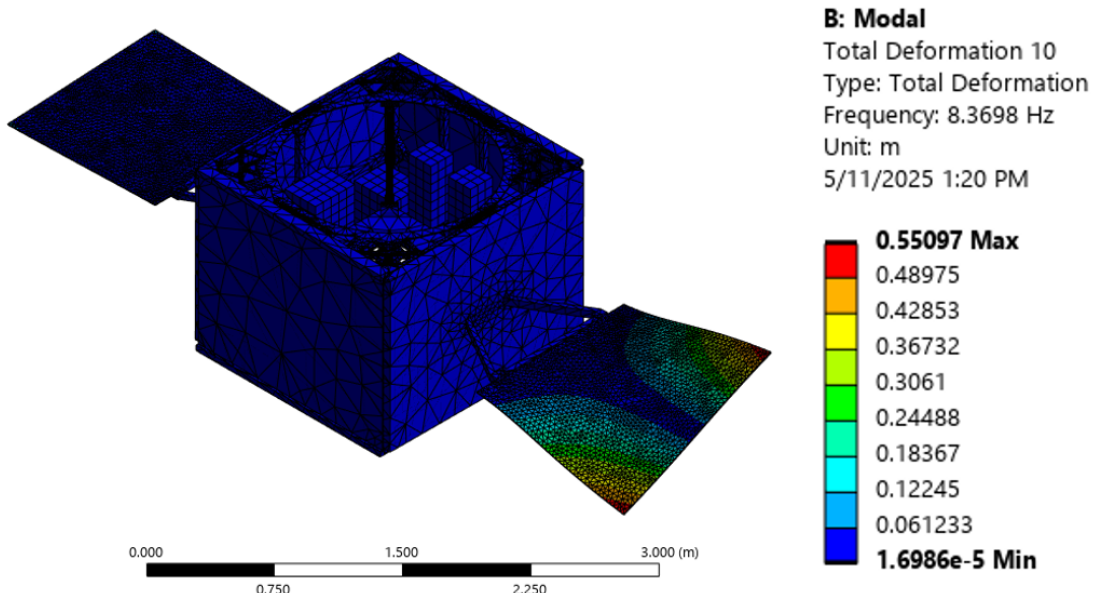


Figure 21: 0.03 Meter Element Size Mesh Results

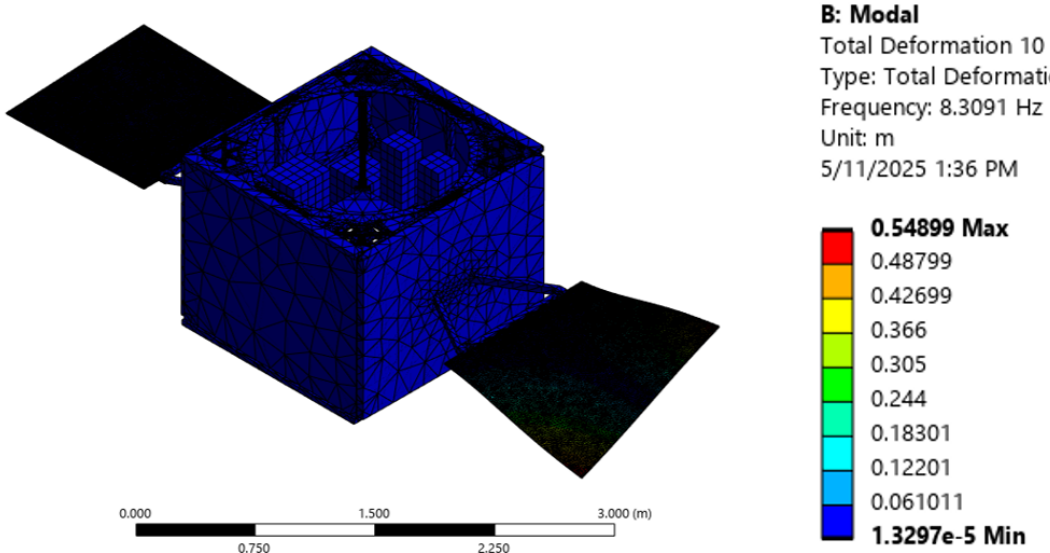


Figure 22: 0.015 Meter Element Size Mesh Results

The maximum displacement and frequency for each local element sizing are used to define convergence. Using the equation:

$$\text{Percentage Change} = \left( \frac{\text{New Value} - \text{Old Value}}{\text{Old Value}} \right) \times 100 \quad (1)$$

the results of mesh convergence are tabulated and plotted. Once the percentage change is below 1%, the mesh is considered to be properly refined. From the data, a local element sizing of 0.015 meters is determined for the solar panels. As the honeycomb panels on the side profiles of the model are responsible for resisting shear, an element sizing of 0.015 meters is used locally on these faces.

Table 2: Percentage change in frequency and maximum displacement between successive mesh refinements

Mesh Size From (m)	Mesh Size To (m)	Frequency Change (%)	Max Displacement Change (%)
0.250	0.125	-7.85%	+3.15%
0.125	0.060	-31.43%	+0.83%
0.060	0.030	-6.10%	-4.48%
0.030	0.015	-0.73%	-0.36%

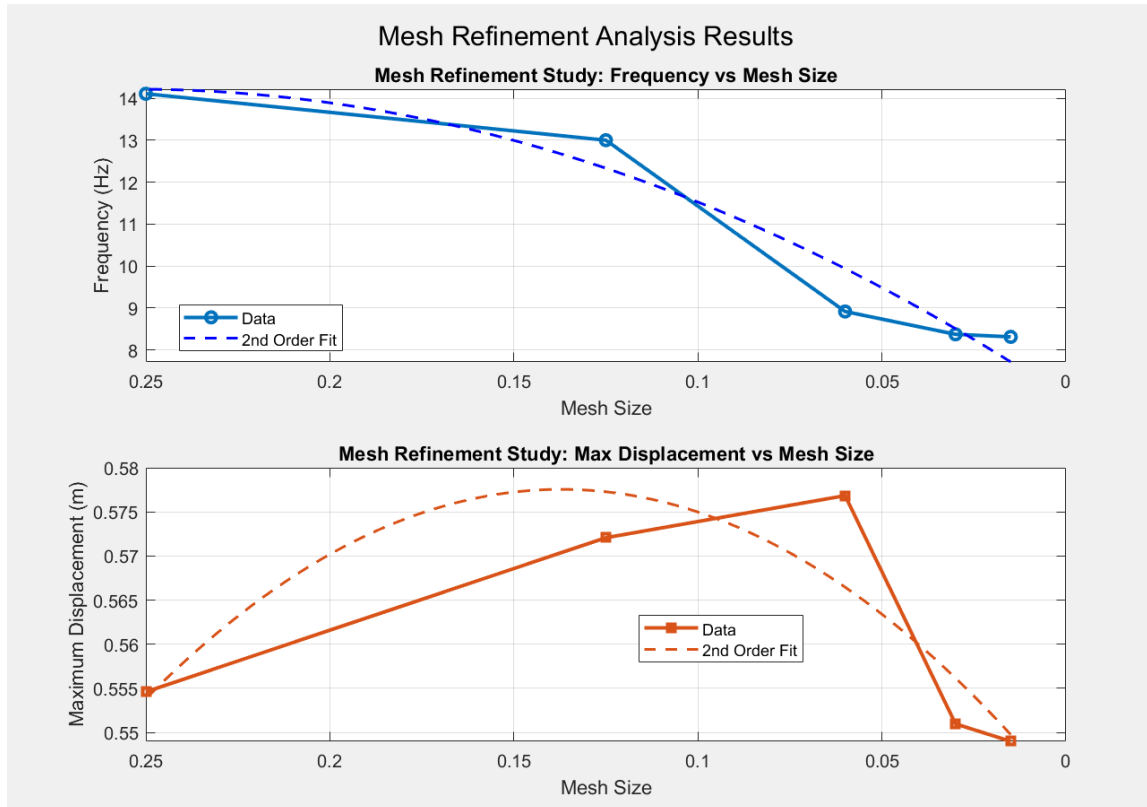


Figure 23: Mesh Convergence Results

This process is essential to ensure that the solution is independent of the discretization and that numerical errors associated with the mesh are minimized. Without demonstrating mesh convergence, simulation results may be unreliable and susceptible to discretization artifacts, potentially compromising the fidelity of the analysis and the safety of subsequent designs. As such, mesh convergence studies are an indispensable part of model verification and are often required to substantiate the credibility of finite element models in both academic research and industry practice.

### 5.3 Freely-Rotating Modal Analysis

The first step in characterizing the dynamic behavior of the large-scale structure involves importing the meshed geometry into the Ansys Modal module to perform an eigenvalue-based modal analysis. To replicate the physical boundary conditions of the experimental setup, the model is constrained using a remote displacement boundary condition rather than a direct geometric constraint. This approach enables the simulation of a point-based support condition, corresponding to the physical center of rotation located at the spherical air bearing interface. The remote displacement is configured to fully restrain translational degrees of freedom (UX, UY, UZ), thereby preventing rigid body motion in space, while leaving rotational degrees of freedom (ROTX, ROTY, ROTZ) unconstrained [2]. This ac-

curately reflects the experimental configuration, wherein the structure is free to undergo rotations about all three principal axes while remaining translationally fixed. By implementing this boundary condition, the resulting mode shapes and natural frequencies extracted from the analysis are representative of the behavior expected under experimental conditions. The meshed geometry in the modal analysis is shown below:

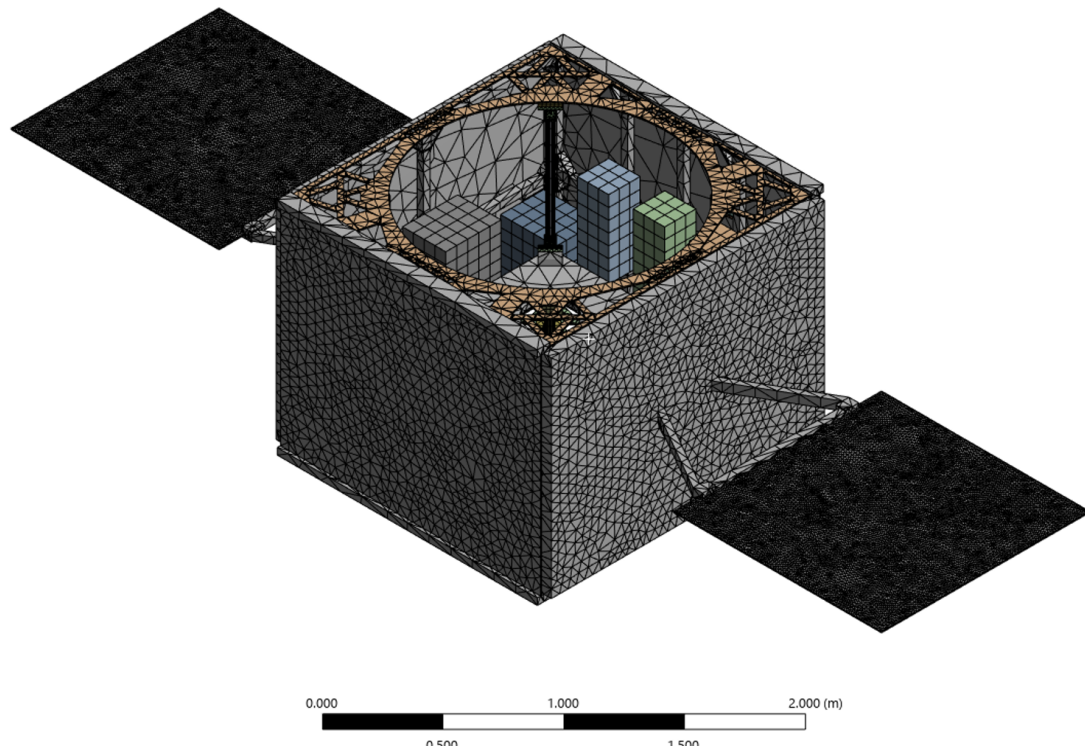


Figure 24: Final Meshed Geometry in Modal Analysis

In Ansys Modal, the analysis settings define the parameters governing the solution of the eigenvalue problem, which determines the natural frequencies of the large-scale structure and the associated mode shapes. A critical setting is the number of eigenmodes to extract, which must be sufficient to capture the frequency range of interest and adequately resolve the dynamic behavior of the system. For the initial modal analysis, 30 eigenmodes are arbitrarily extracted. The solver can incorporate stress stiffening effects, whereby the initial static stress state alters the structure's effective stiffness matrix; this is particularly important for structures under significant preload, such as those subjected to gravitational loading, centrifugal forces, or thermal expansion. Additionally, prestress modal analysis can be enabled by linking the modal solution to a preceding static structural solution, ensuring that the influence of internal stresses on dynamic behavior is properly represented. This method is explored in the following section. The choice of eigenvalue extraction algorithm impacts both computational efficiency and numerical robustness. If large geometric nonlinearities are present prior to modal analysis, the NLGEOM (nonlinear geometry) flag must be activated during the static prestress solve to correctly capture stress stiffening

and follower forces [9]. In the case of the large-scale structure, nonlinear geometries are not considered as all materials are assumed to be isotropic. Postprocessing options such as mode effective mass participation factors and cumulative mass fractions further aid in evaluating the completeness of the extracted modes relative to rigid-body and flexible dynamic behavior. These results are tabulated and discussed in the following section. The workbench overview of the freely-rotating and constant-spin modal analysis is shown below:

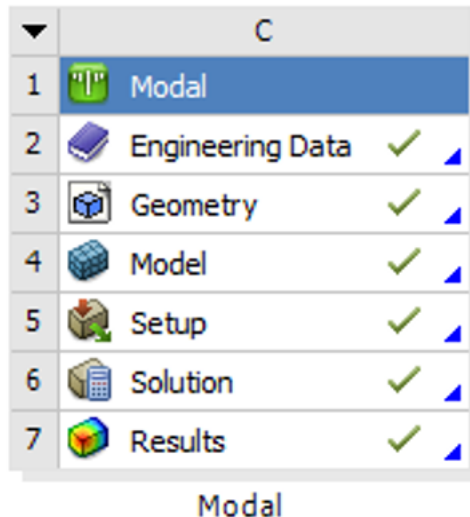


Figure 25: Workbench Overview of Modal Analysis

#### 5.4 Constant-Spin Modal Analysis

To further explore the dynamic behavior, a further constraint is placed upon the model: a constant rotational velocity of 1 rad/s about the  $y$  axis. Using this constraint, behaviors such as wobble and nutation can be studied. Furthermore, the structure can physically rotate about this axis indefinitely. The boundary condition is instilled by right-clicking on the 'Solution' tab in the environment tree and selecting 'Rotational Velocity'. This tool requires a vector component of radial velocity [2] [3]. As the center of rotation is bound to the origin of the model, the vector input is  $[0, 1, 0]$ . The implementation of this constraint is compared to the original freely rotating model in the 'Results and Discussion' section. The constant spin model setup is shown below:

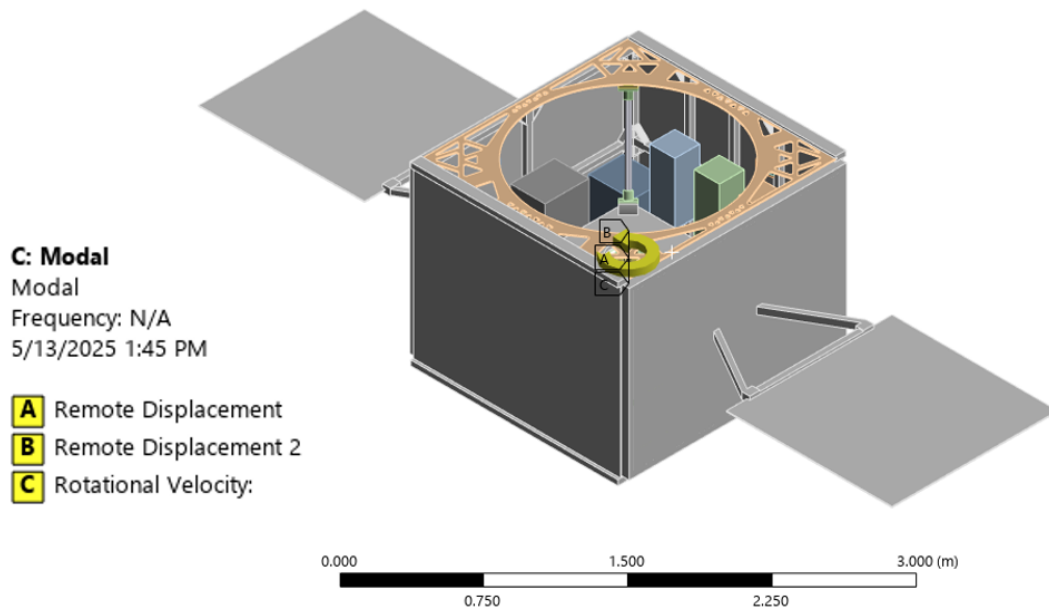


Figure 26: Ansys Modal Setup with Constant Spin Constraint

For the constant spin rate analysis, several modifications are made to the initial modal analysis setup to accurately capture the dynamic behavior. First, the spacecraft is transitioned from a purely rigid body representation to a deformable body configuration, allowing for the simulation of structural flexibility and local deformations that arise during rotation. This change is enforced under the ‘Analysis Settings’ branch of the environment tree, in the ‘Behavior’ tab. This change is critical in enabling the finite element model to resolve true mode shapes associated with both global and local dynamic responses, rather than restricting the analysis to idealized rigid body motions. Additionally, the Coriolis effect is activated within the solver settings to account for inertial forces arising from the rotational motion. The inclusion of Coriolis forces introduces gyroscopic coupling between translational and rotational degrees of freedom, resulting in complex-valued mode shapes and an asymmetric dynamic stiffness matrix [3]. The addition of the Coriolis effect is also enforced under the ‘Analysis Settings’ branch of the environment tree, in tab ‘Coriolis Effect’. This setup adjustment was necessary to realistically simulate the influence of gyroscopic effects. Including both of these behaviors ensures that the computed modal characteristics accurately reflect the operational conditions the structure experiences during operations.

## 5.5 Prestressed Modal Analysis

In the second modal analysis, the model is pre-stressed in Ansys Static Structural to accurately predict the behavior of the large-scale structure under a typical thrust maneuver from the propulsion system. This method aims to represent the constraint of  $45^\circ$  of rota-

tional freedom about the  $x$  and  $y$  axes. The  $45^\circ$  of freedom is defined from the mid-plane to the angle at which the lifting mechanism comes into contact with the bumper [1]. As this region can occur in two directions, the goal is to allow the satellite to rotate up to a maximum of  $90^\circ$  under its own gravitational moment, and that induced by the thrusters. To achieve this, a rotational spring stiffness is derived to balance these moments at the maximum permitted rotation. We assume a typical thrusting maneuver, where two thrusters, each generating a force  $F = 2.5 \text{ N}$ , are mounted symmetrically with a moment arm of  $r_{\text{thruster}} = 24 \text{ inches}$  from the spacecraft center. Converting the moment arm to meters:

$$r_{\text{thruster}} = 24 \times 0.0254 = 0.6096 \text{ m}$$

The total force applied is:

$$F_{\text{total}} = 2 \times 2.5 = 5.0 \text{ N}$$

Thus, the total torque generated by the thrusters about the center is:

$$\tau_{\text{thruster}} = F_{\text{total}} \times r_{\text{thruster}}$$

Substituting known values:

$$\tau_{\text{thruster}} = 5.0 \times 0.6096 = 3.048 \text{ N} \cdot \text{m}$$

The restoring torque produced by translational springs placed at a moment arm  $r_{\text{spring}}$  is expressed as:

$$\tau_{\text{spring}} = F_{\text{spring}} \times r_{\text{spring}}$$

where the spring force is:

$$F_{\text{spring}} = k \times x$$

and the displacement  $x$  for a rotation  $\theta$  is:

$$x = r_{\text{spring}} \times \theta$$

Thus:

$$F_{\text{spring}} = k r_{\text{spring}} \theta$$

Substituting back into the torque expression:

$$\tau_{\text{spring}} = k r_{\text{spring}}^2 \theta$$

At the maximum displacement ( $\theta = \frac{\pi}{2}$ ), the spring-generated torque must balance the thruster-induced torque:

$$k r_{\text{spring}}^2 \theta = \tau_{\text{thruster}}$$

Solving for  $k$ :

$$k = \frac{\tau_{\text{thruster}}}{r_{\text{spring}}^2 \theta}$$

Substituting the known values:

$$r_{\text{spring}} = 0.62 \text{ m}$$

$$\theta = \frac{\pi}{2} \text{ rad}$$

$$\tau_{\text{thruster}} = 3.048 \text{ N} \cdot \text{m}$$

Thus:

$$k = \frac{3.048}{(0.62)^2 \times \left(\frac{\pi}{2}\right)}$$

Calculating:

$$(0.62)^2 = 0.3844$$

$$\frac{\pi}{2} \approx 1.5708$$

$$0.3844 \times 1.5708 = 0.6039$$

$$k = \frac{3.048}{0.6039} \approx 5.05 \text{ N/m}$$

Therefore, to achieve an angular freedom of  $90^\circ$  under the specified thruster loading conditions, the required equivalent translational spring stiffness placed at a radius of 0.62 meters from the center is:

$$k = 5.05 \text{ N/m}$$

These values are inputted for both springs in the static structural model. It is important to note that this model enforces rotational limits through imaginary springs. In the physical model, the rotational freedom is constrained through contact with the bumper from the lifting mechanism. As the lifting mechanism is not included in the analysis, these imaginary springs act as the forcing function to ensure the physical angular requirements. While not accurate to the physical model, this constraint is used to explore the behavior of a rotationally restricted system. In Ansys Static Structural, these springs are created using the 'Insert Spring' function, obtained by right-clicking the 'Contacts' division in the environment tree. The 'body-to-ground' spring is selected, as the 'body-to-body' spring is never compressed or stretched due to the rigid behavior of the structure [4]. In the 'body-to-ground' options, the ground connection is established through  $x$ ,  $y$ , and  $z$  coordinates. The  $y$  coordinate is given a value of  $-0.62m$  to establish a perpendicular moment arm at the level of the bottom isogrid, while the  $x$  and  $z$  coordinates remain at zero. The spring configuration is depicted below:

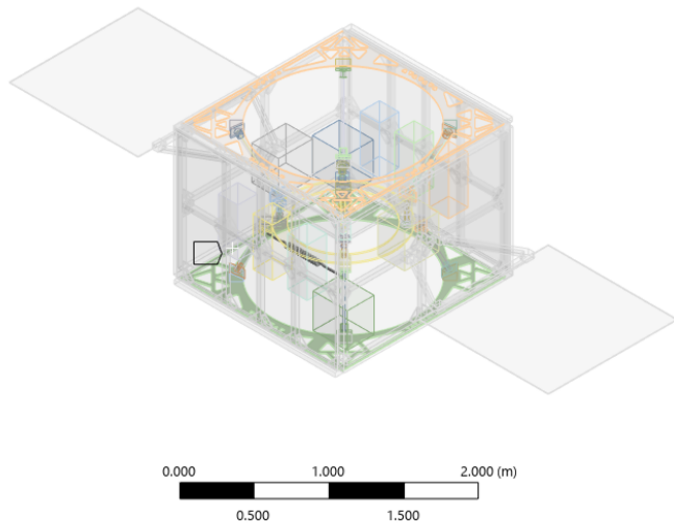


Figure 27: Isometric View of Spring Configuration

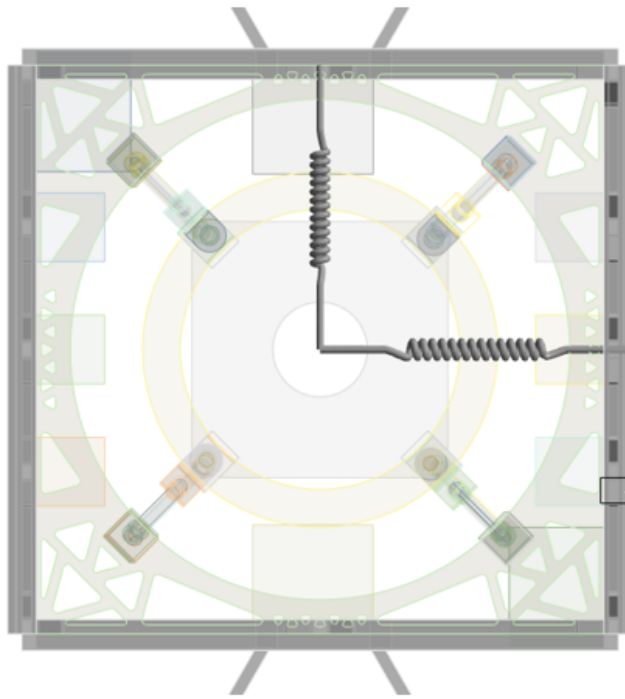


Figure 28: Bottom View of Spring Configuration

The boundary conditions are established in Static Structural using a similar approach from the initial modal analysis. The structure is constrained through a remote displacement boundary condition at the center of rotation. In contrast to the constraints of the remote point that the original modal analysis, this remote point has fully constrained translational and rotational freedom. Dynamic effects are neglected in Static Structural as loads are applied without time dependency. Thus, Static Structural is solely responsible for pre-loading the large-scale structure, and the boundary conditions are fully fixed to achieve such behavior. The pre-conditioned ‘inertial Earth gravity’ boundary condition is input to properly weight the structure. A nominal thrust value of  $2.5\text{ N}$  is applied at two thruster locations on opposite corners of the satellite bus. The thrust at each node in vector form is  $[0, 0, -2.5]$  and  $[0, 0, 2.5]$ , respectively. The purpose of the particular thrusting maneuver selected is outside of the scope of the project and will not be discussed. The model simply aims to predict the dynamic behavior of the large-scale structure under thrust loading conditions. The fully bounded Static Structural Model is found below:

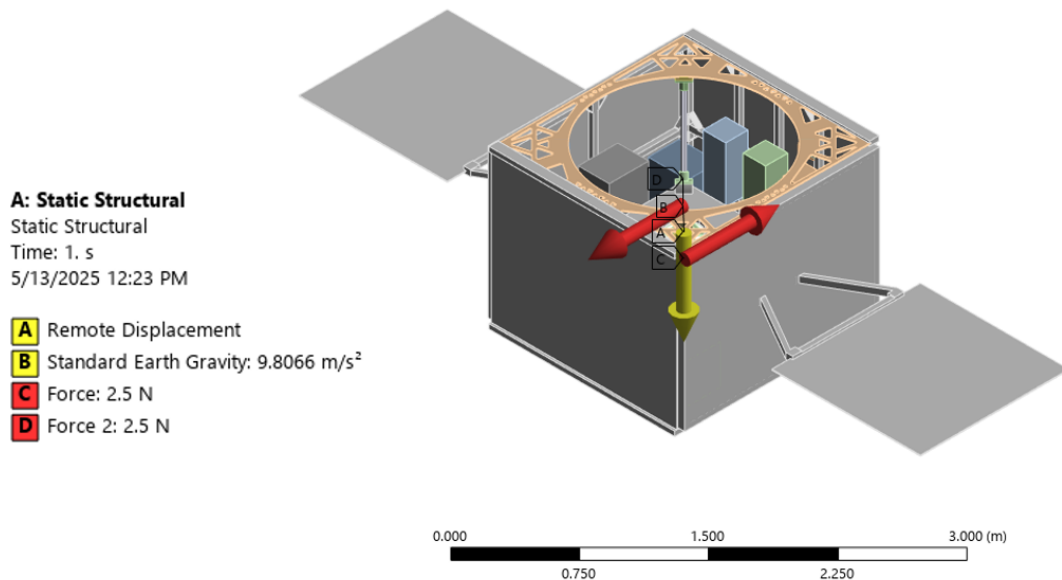


Figure 29: Static Structural Model Setup (Isometric View)

The Static Structural solution is initialized, yielding stress and strain contour plots. The pre-stressed solution is input to the modal analysis, from which the original modal boundary conditions, material assignments, and contact regions are established. Additionally, the analysis inquires for thirty mode shapes in accordance with the previous model. The solution is run to extract the natural frequencies and corresponding mode shapes. The workbench model of this analysis is shown below:

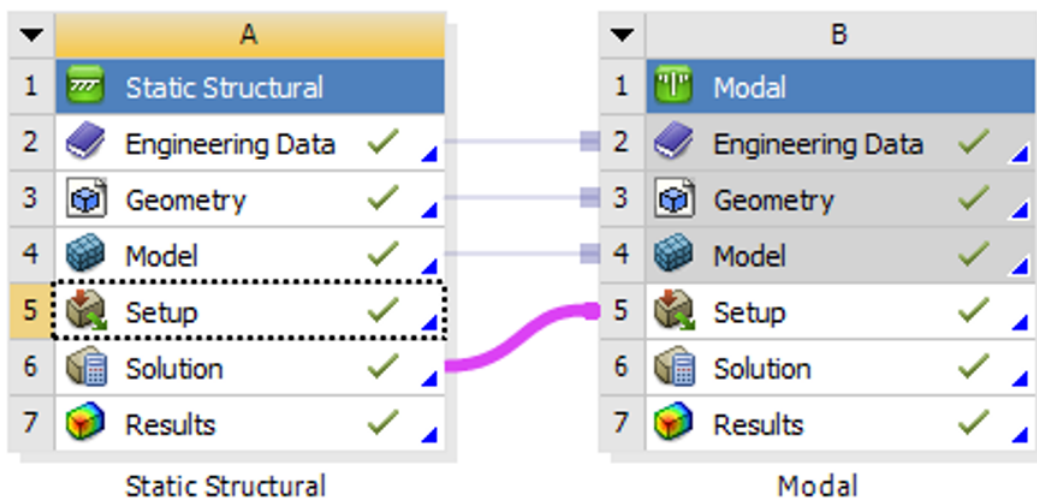


Figure 30: Workbench Overview of Static Structural and Modal Model

## 6. Results and Discussions

This section presents and interprets the results of the numerical analyses performed on the large-scale structural model. Initially, the outcomes of the undisturbed modal analysis are discussed, providing insight into the natural frequencies and corresponding mode shapes of the unconstrained structure. These results establish a baseline understanding of the structure's dynamic characteristics under idealized boundary conditions. Subsequently, the effects of gravitational loading are incorporated through a pre-stressed modal analysis, allowing the influence of static deformation and stress stiffening on the modal behavior to be evaluated. Comparative assessments between the baseline and pre-stressed cases are provided to quantify changes in modal frequencies, mode shapes, and mass participation. The discussion aims to not only validate the numerical approach but also to draw conclusions regarding the structure's expected performance in experimental and operational conditions.

### 6.1 Freely-Rotating Modal Analysis Results

#### 6.1.1 Effective Mass Ratio Tables

In modal analysis, the concept of effective mass quantifies how much of the total system mass participates in a given mode of vibration. Specifically, effective mass measures the dynamic contribution of each mode to the overall translational or rotational motion of the structure when subjected to external excitation. Modes with higher effective mass in a given direction are more significant because they are more easily excited by loads in that direction. Conversely, modes with very low effective mass are typically less relevant to the dynamic response. Assessing the distribution of effective mass across the extracted modes is critical to ensuring that the modal basis sufficiently captures the dynamical behavior of the satellite structure. In engineering practice, it is common to verify that a sufficient number of modes have been extracted to account for a high cumulative percentage of the system's mass. For the methods included in this report, a threshold of 85% in all directions of interest is established, thereby validating the completeness and reliability of the modal analysis. The effective mass table for the initial modal analysis as a percentage of the total mass is shown below:

Mode	Frequency [Hz]	X Direction	Y Direction	Z Direction
1	0.	1.5996e-004	2.3305e-007	1.2406e-004
2	9.5134e-004	1.5093e-004	8.9099e-006	4.8343e-004
3	1.7092e-003	1.3268e-004	2.7807e-007	8.1023e-005
4	3.2036	7.7364e-006	5.4209e-002	1.3861e-008
5	3.9598	2.9217e-004	1.0314e-003	8.6674e-007
6	8.0429	8.3963e-008	2.9586e-008	1.5453e-005
7	8.3032	1.8354e-007	3.4552e-007	2.406e-005
8	9.3796	0.9023	8.4906e-006	3.4989e-004
9	11.075	5.043e-004	9.3822e-006	0.5149
10	13.977	1.2295e-005	0.68489	1.6541e-004
11	14.405	9.4679e-006	3.9419e-004	0.3306
12	15.526	1.1238e-006	3.1098e-006	6.5387e-002
13	16.646	7.809e-007	0.10251	4.9871e-006
14	18.774	3.3236e-006	1.793e-002	2.6286e-006
15	26.666	6.8058e-010	2.8955e-009	2.1655e-007
16	27.346	1.8138e-011	7.7114e-005	4.5566e-009
17	27.604	7.024e-009	6.2322e-005	2.7903e-008
18	28.654	4.7069e-010	1.0947e-007	1.7948e-007
19	38.025	3.2264e-006	1.9949e-008	2.9312e-007
20	38.598	5.8208e-004	6.7814e-006	3.4801e-007
21	38.656	4.8058e-006	4.0038e-003	8.8577e-008
22	38.821	4.6214e-004	7.3134e-003	1.5885e-007
23	38.864	5.2554e-003	8.0399e-004	5.3357e-009
24	41.074	1.4691e-007	1.3889e-007	3.0851e-010
25	42.296	3.2441e-006	8.8633e-005	1.5627e-007
26	48.912	5.3712e-007	5.6025e-007	1.3287e-005
27	49.519	2.5055e-006	3.056e-006	1.1365e-004
28	50.231	4.2911e-008	1.2362e-007	1.0008e-005
29	50.959	4.1928e-005	5.4837e-006	3.0935e-005
30	51.547	7.1365e-004	5.26e-007	2.8098e-006
Sum		0.91064	0.87336	0.91231

Figure 31: Translational Direction Effective Mass Table

Mode	Frequency [Hz]	Rotation X	Rotation Y	Rotation Z
1	0.	0.1603	0.53404	0.32799
2	9.5134e-004	0.6584	5.7661e-006	0.29369
3	1.7092e-003	0.1813	0.46596	0.37832
4	3.2036	6.1986e-017	1.7911e-015	1.9554e-016
5	3.9598	1.4842e-016	2.7469e-018	7.8379e-016
6	8.0429	4.2313e-019	1.177e-017	1.0371e-019
7	8.3032	2.7261e-020	1.0754e-017	2.0711e-018
8	9.3796	5.2643e-015	1.2304e-018	6.4435e-015
9	11.075	4.1131e-015	1.4935e-016	3.6048e-016
10	13.977	2.1886e-016	1.1281e-016	1.5609e-016
11	14.405	2.4305e-015	1.4472e-016	1.1757e-016
12	15.526	6.415e-016	1.0694e-017	1.3084e-017
13	16.646	3.4402e-017	2.9285e-019	2.3073e-017
14	18.774	7.693e-018	5.5438e-018	2.5837e-018
15	26.666	3.2597e-019	7.9714e-021	7.2623e-021
16	27.346	3.9984e-021	2.1193e-020	9.8746e-020
17	27.604	4.2834e-020	1.2329e-019	1.5888e-020
18	28.654	1.2789e-020	3.2382e-019	3.6519e-020
19	38.025	6.0409e-019	3.8464e-019	4.1789e-017
20	38.598	1.911e-019	2.2883e-018	1.3647e-016
21	38.656	1.0551e-018	2.1436e-018	9.1706e-018
22	38.821	1.2861e-017	3.9224e-020	1.5865e-018
23	38.864	2.0417e-017	8.3499e-019	3.8828e-019
24	41.074	2.6145e-019	9.1479e-019	3.0999e-020
25	42.296	2.6967e-020	2.016e-019	6.6193e-021
26	48.912	9.4432e-017	8.4381e-019	1.3238e-018
27	49.519	7.4213e-016	7.8214e-018	7.9212e-018
28	50.231	3.6811e-018	5.383e-018	6.5924e-018
29	50.959	6.1577e-018	2.9092e-018	5.5525e-018
30	51.547	9.1215e-019	1.5399e-018	7.2734e-018
Sum		1.	1.	1.

Figure 32: Rotational Direction Effective Mass Table

The effective mass tables denote key characteristics of the structure's dynamical behavior. First, it is important to note that the sum of the rotational effective mass fractions all sum to 1, as the rotation of the model is not constrained. Furthermore, all translational sums of the effective mass fraction are above 0.85, the threshold discussed above. As seen in the tables, there are three natural frequencies with a value of zero (any number on the order of  $10^{-3}$  is considered to be zero in the analysis). This corresponds to the three

rotational rigid body modes, as the three translational rigid body modes are constrained in the setup. As the model is allowed to freely rotate, no higher order mode contributes to the rotational motion of the structure. Instead, the translational behavior is dominated by higher order modes. For example, much of the excitation in the x-direction is derived from the 8th natural mode of frequency. The translational excitation in the y-direction is dominated by the 10th and 13th normal modes, and the excitation in the z-direction is influenced heavily by the 9th and 11th modes.

### 6.1.2 Mode Shapes

The 8th normal mode of frequency, which dominates excitation in the x-direction, is shown below:

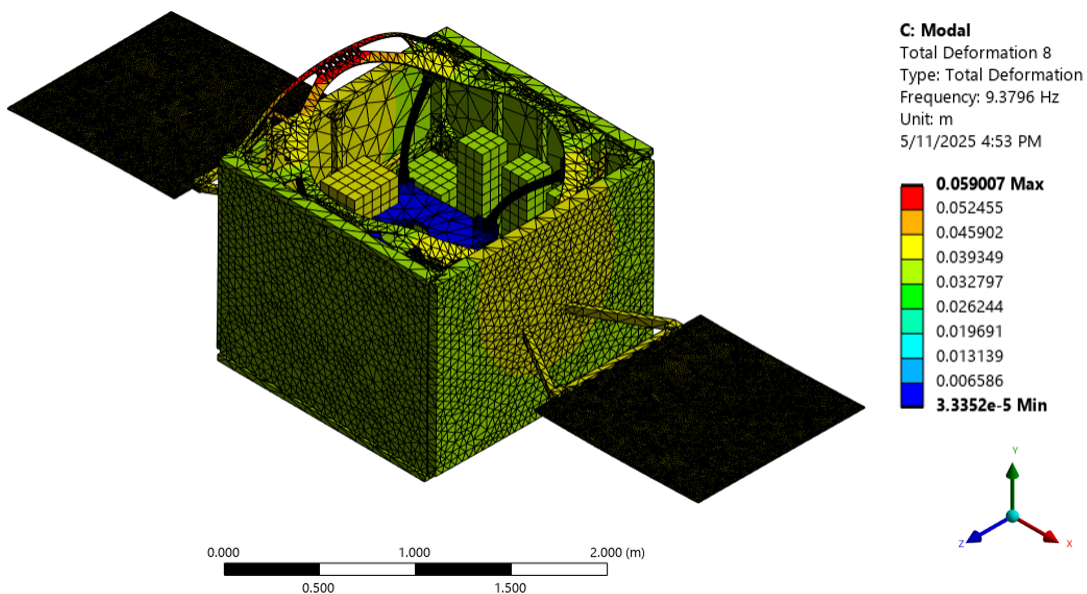
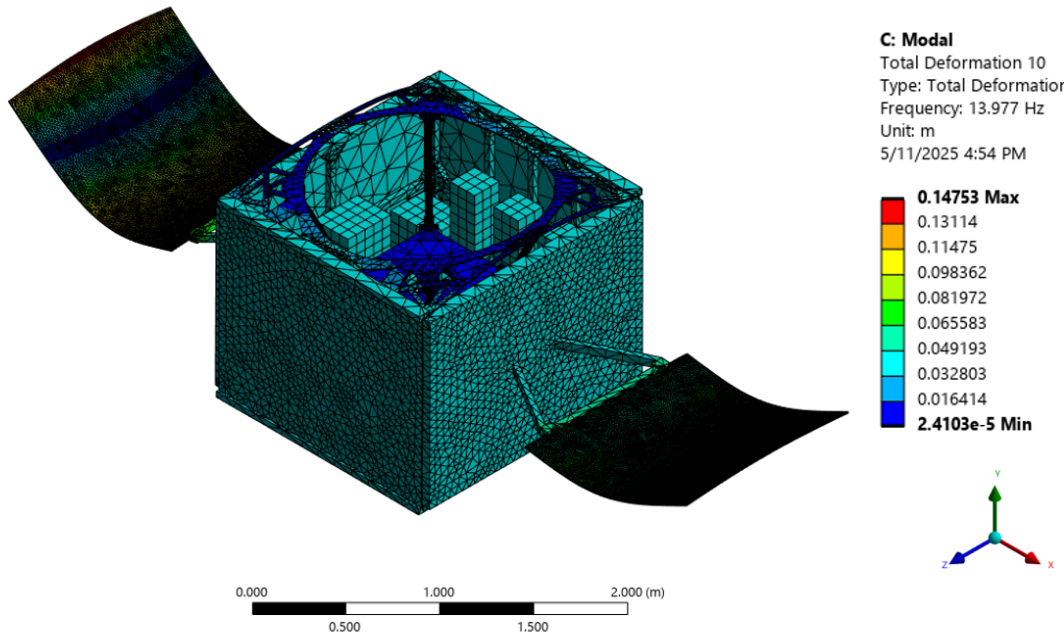
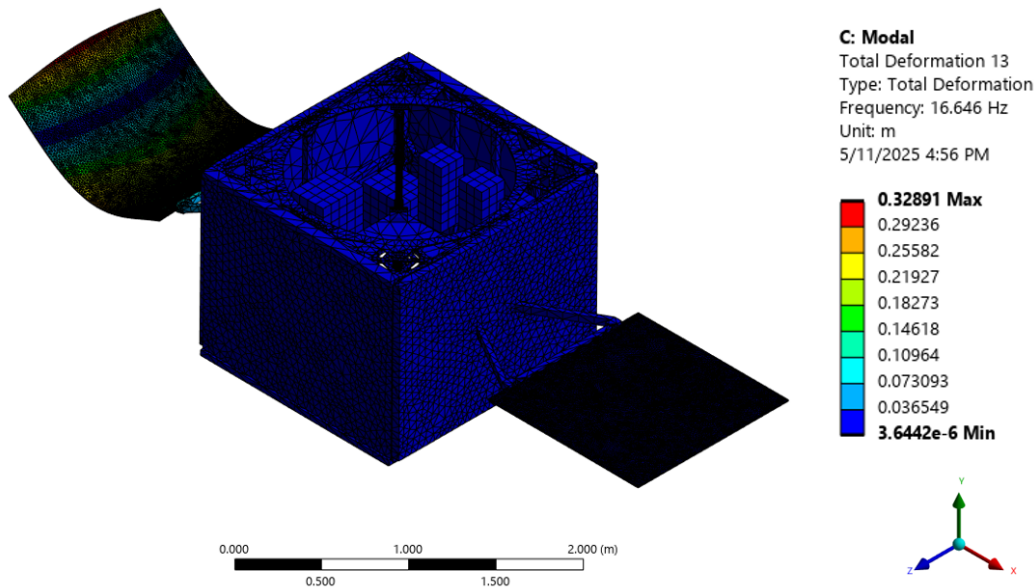


Figure 33: 8<sup>th</sup> Normal Mode for Free Rotational Model

The 8th total deformation occurs at a frequency of 9.3796 Hz. As seen in the figure, the bearing plate remains bounded by the spherical air bearing. The outer structure is pulled in the positive x-direction, as indicated by the flexure of the inner structure. The maximum deformation occurs at the midpoint of the isogrid in the negative x-direction, with a value of 5.9 cm. The mode shape shows a collision between one CMG assembly and the bearing plate. The CMG assembly deflects 3.9349 cm to the positive x-direction: a considerable distance within the clearance of 5.3 cm between the CMG assembly and bearing plate.

Figure 34: 10<sup>th</sup> Normal Mode for Free Rotational ModelFigure 35: 13<sup>th</sup> Normal Mode for Free Rotational Model

The 10th and 13th normal modes determine much of the translational dynamic behavior in the y-direction, having effective mass ratios of 0.685 and 0.103, respectively. The 10th mode of frequency occurs at 13.977 Hz. In this mode, the structure is being pulled in the

positive y-direction, with a maximum deflection of 14.75 cm occurring at the outside edges of the solar panels. The isogrid is pulled in a positive y-direction at the midpoint of the edges connected to the outer structure. The 13th normal mode brings the validity of the approach into question. As seen in Figure 35, the deformation of the 13th mode shape occurs locally along the left lateral solar panel. This is not indicative of any dynamical behavior expected in the model, as the results show the entire bus structure is fixed. Several factors can lead to unrealistic localized deformation behavior in a modal analysis, particularly in structures with appendages such as solar panels. Improper modeling of the panel-to-body connection, such as insufficient hinge stiffness or poorly defined contact conditions, can cause panels to appear detached from the main structure and vibrate independently. This contact is defined as an edge region, which is exhibitive of the fully detailed structure. Localized modes may occur at higher frequencies if the satellite body is modeled with a greater stiffness relative to the appendages, but the entire outer structure is assigned an aluminum alloy material stiffness. Unrealistic mass distribution through mass lumping errors can distort the true dynamic response. Lastly, if the solar panels are permitted to rotate with negligible stiffness at their connection points, they can develop low-frequency decoupled modes, although these should still induce slight motion in the primary structure. This is the most likely reason for this unnatural mode shape occurring.

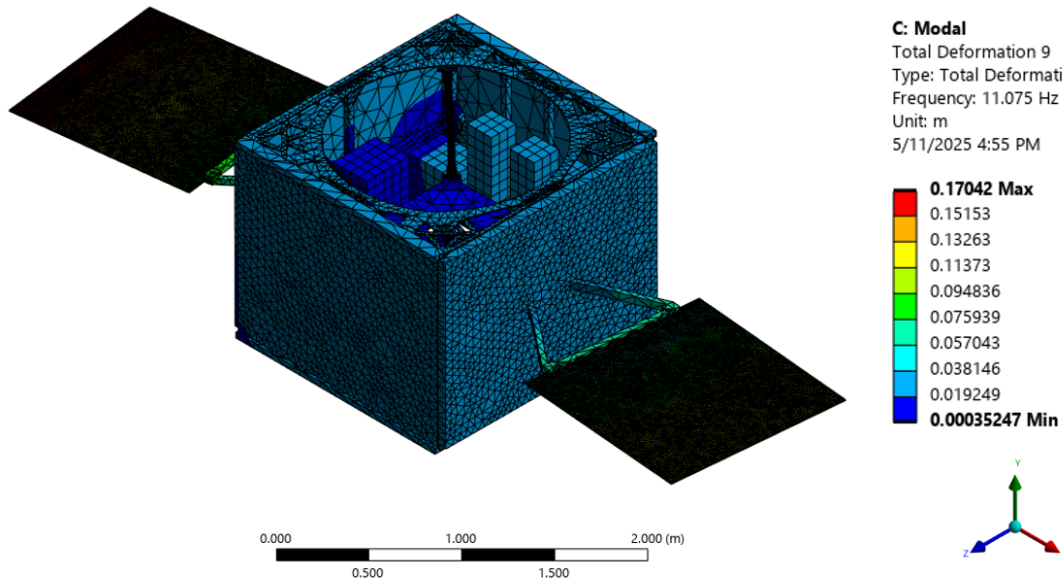


Figure 36: 9<sup>th</sup> Normal Mode for Free Rotational Model

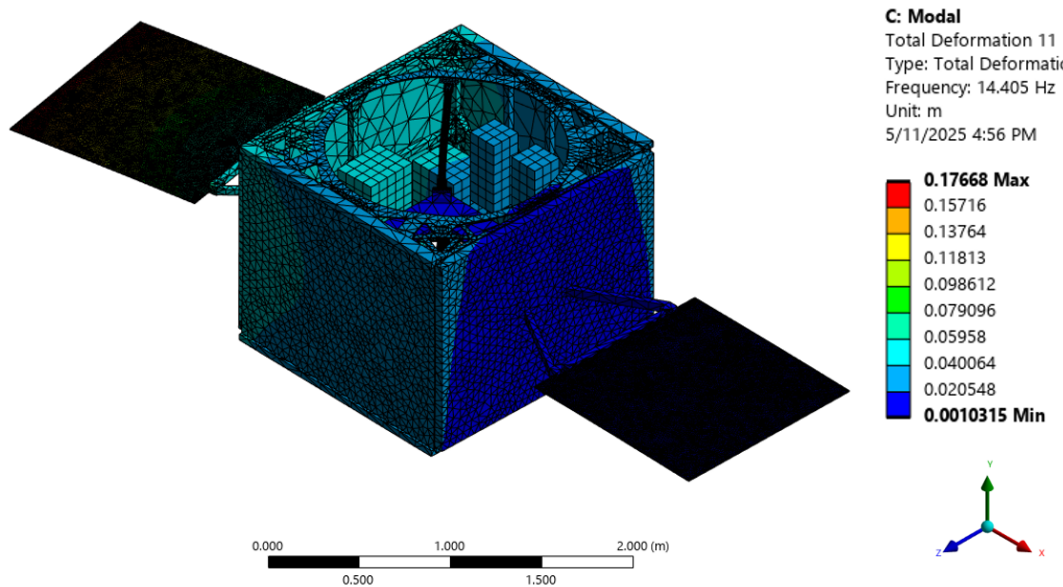


Figure 37: 11<sup>th</sup> Normal Mode for Free Rotational Model

The excitation in the  $z$ -direction is influenced heavily by the 9th and 11th modes. The 9th and 11th modes are symmetric about the  $z$ -axis, both demonstrating flexion of the solar beams laterally as a cantilever beam. The 9th natural mode occurs at 11.075 Hz and has a maximum deflection of 17.04 cm at the corner nodes of the right (positive  $x$ -direction) solar panel. The 11th mode shape occurs at 14.405 Hz and has a similar maximum deflection of 17.67 cm at the corner nodes of the left (negative  $x$ -direction) solar panel.

## 6.2 Constant-Spin Modal Analysis Results

### 6.2.1 Effective Mass Ratio Tables

As discussed in the ‘Methodology and Experimental Details’ section, the constant spin study is the same as the original modal analysis with one further condition placed upon the model: a constant radial velocity of 1 rad/s about the  $y$ -axis. This conditional study is an accurate representation of a particular physical behavior of the large-scale structure. Under these conditions, the structure does not rotate about the  $x$  or  $z$  axes; thus, the interference of the bumper during a 45° tilt around either of these axes is not considered. The effective mass ratio tables for the constant spin study are shown below:

Mode	Frequency [Hz]	X Direction (Real)	Y Direction (Real)	Z Direction (Real)
1	0.	2.4452e-004	3.5251e-006	8.5654e-006
2	1.0696e-003	1.9862e-006	1.1395e-019	3.7737e-006
3	0.51326	7.3565e-005	4.277e-006	2.4676e-004
4	3.0843	8.12e-006	5.3413e-002	1.6594e-008
5	3.841	3.1192e-004	9.3125e-004	9.8686e-007
6	8.247	7.8894e-008	2.9811e-008	1.4008e-005
7	8.5093	2.0775e-007	2.9006e-007	2.3747e-005
8	9.3796	0.90223	8.6943e-006	3.4995e-004
9	11.075	5.0432e-004	9.3452e-006	0.51489
10	13.976	1.2309e-005	0.68054	1.6433e-004
11	14.405	9.4687e-006	3.8953e-004	0.3306
12	15.526	1.1239e-006	2.6868e-006	6.5387e-002
13	16.627	7.8317e-007	0.10504	5.2246e-006
14	18.753	3.3463e-006	1.8598e-002	2.6574e-006
15	26.539	5.1118e-010	2.1923e-009	1.8359e-007
16	27.747	7.5738e-009	2.9413e-005	2.5857e-008
17	27.873	8.038e-011	4.2944e-005	5.5041e-009
18	28.918	4.3288e-010	8.3378e-008	1.4348e-007
19	38.007	2.7939e-006	3.7244e-007	2.8526e-007
20	38.591	5.49e-004	6.1232e-006	3.6334e-007
21	38.656	6.4622e-006	3.9668e-003	8.6357e-008
22	38.821	4.4012e-004	7.3785e-003	1.5828e-007
23	38.863	5.3095e-003	7.8033e-004	6.3901e-009
24	41.074	1.5021e-007	1.3585e-007	2.9451e-010
25	42.306	3.2334e-006	9.0983e-005	1.5618e-007
26	48.971	6.1258e-007	6.4585e-007	1.5791e-005
27	49.533	2.4147e-006	2.9586e-006	1.1091e-004
28	50.232	4.2208e-008	1.214e-007	1.0069e-005
29	50.959	4.2e-005	5.4906e-006	3.0902e-005
30	51.548	7.1346e-004	5.1552e-007	2.8102e-006

Figure 38: Real Components of Effective Mass

Mode	Frequency [Hz]	X Direction (Imaginary)	Y Direction (Imaginary)	Z Direction (Imaginary)
1	0.	0.	0.	0.
2	1.0696e-003	2.8363e-009	8.3373e-011	5.9313e-009
3	0.51326	3.1491e-004	2.3114e-007	1.3934e-004
4	3.0843	1.0421e-009	1.4544e-010	1.4674e-009
5	3.841	3.4718e-008	3.3543e-010	2.1325e-009
6	8.247	3.3267e-005	4.3118e-003	2.0749e-011
7	8.5093	8.7509e-005	2.1922e-003	1.0216e-008
8	9.3796	4.0896e-009	1.5086e-011	4.4786e-006
9	11.075	8.2314e-006	3.9803e-009	2.8663e-010
10	13.976	1.8696e-009	5.8259e-011	2.091e-007
11	14.405	2.1687e-006	3.5465e-007	1.0156e-009
12	15.526	4.1113e-007	1.9182e-007	1.0091e-009
13	16.627	7.9916e-011	1.3667e-011	9.491e-008
14	18.753	2.3355e-010	1.6491e-008	3.8434e-008
15	26.539	6.6356e-010	3.4931e-007	3.7948e-009
16	27.747	6.1555e-011	3.6283e-009	4.819e-008
17	27.873	2.1472e-010	1.4435e-008	2.7997e-008
18	28.918	1.7613e-010	2.9712e-005	2.5419e-010
19	38.007	6.53e-009	1.9256e-009	6.492e-008
20	38.591	3.2109e-007	2.6787e-007	9.4077e-008
21	38.656	9.9366e-008	5.769e-008	4.8864e-009
22	38.821	1.5331e-007	6.0394e-010	2.6443e-008
23	38.863	7.5107e-008	7.8105e-008	4.1207e-007
24	41.074	3.3808e-011	3.098e-012	1.0601e-010
25	42.306	2.6621e-010	6.1503e-010	6.3322e-012
26	48.971	1.7697e-007	2.9057e-007	2.3082e-009
27	49.533	4.7628e-008	5.7655e-008	3.0931e-010
28	50.232	2.7981e-009	5.8646e-009	3.3331e-009
29	50.959	9.6995e-009	5.3474e-009	2.3204e-011
30	51.548	7.1717e-010	1.0774e-010	1.7216e-008

Figure 39: Imaginary Components of Effective Mass

In the context of the constant spin rate modal analysis, the effective mass participation results are presented separately in terms of real and imaginary components, rather than purely translational and rotational contributions. This distinction arises due to the introduction of gyroscopic effects, which fundamentally alter the dynamic behavior of the system. Under a constant spin condition, the governing equations of motion become complex-valued as a result of the asymmetric coupling between inertial forces and displacements. Consequently, the resulting mode shapes are also complex, leading to effective mass

ratios that must be interpreted in terms of their real and imaginary parts. The real component represents the in-phase response of the structure to an applied base excitation, while the imaginary component captures the out-of-phase response induced by gyroscopic coupling. This behavior contrasts with a non-spinning system, where the mass and stiffness matrices remain real and symmetric, yielding purely real mode shapes and conventional translational and rotational effective mass participation. Therefore, in the spinning system, the decomposition into real and imaginary parts is necessary to fully characterize the dynamic response and to accurately account for the additional inertial coupling introduced by the spin environment. The imaginary parts of the effective mass ratios are nearly zero because the spacecraft model is spinning at a very low rate (1 rad/s), resulting in negligible gyroscopic coupling and a dynamic response that closely resembles that of a non-rotating structure. Thus, mode shapes suggestive of the original modal analysis are expected after running the constant-spin analysis.

### 6.2.2 Discussion on Nutation Frequency

Considering the constant spin boundary condition, we expect the model to have a nutation frequency corresponding to one of the first non-zero frequencies in the effective mass ratio table. In the constant spin analysis, only one mode shape is observed at exactly zero frequency, representing pure steady-state spin about the principal spin axis. Unlike a non-spinning rigid body, where six rigid body modes typically appear at or near zero frequency, the introduction of a constant spin rate fundamentally alters the dynamic behavior. The spin provides dynamic stiffness in the transverse rotational directions, effectively eliminating free rotation about axes orthogonal to the spin axis. Instead, the dynamic response in these directions becomes associated with nutation motion, which occurs at a nonzero frequency determined by the spacecraft's mass distribution and spin rate. As a result, the translational rigid body modes are suppressed, and only the steady spin about the principal axis remains at zero frequency. The first nonzero modes in the effective mass table correspond to nutation dynamics and elastic deformations influenced by the gyroscopic coupling. This behavior reflects the expected physics of a spinning spacecraft, where the spin axis remains dynamically stiffened against perturbations while nutational motions emerge as low-frequency oscillations. To assess the validity of the constant-spin analysis, the calculated nutation frequency is compared to the nutation frequency observed in the effective mass ratio table. The calculation is performed below, beginning with the principal inertia matrix derived from the geometry in the modal analysis:

**Principal Moments of Inertia ( $\text{kg}\cdot\text{m}^2$ )**

$$\mathbf{I}_{\text{principal}} = \begin{bmatrix} 289.18 & 0 & 0 \\ 0 & 486.50 & 0 \\ 0 & 0 & 625.66 \end{bmatrix}$$

**Inertia Matrix in Output Coordinate System ( $\text{kg}\cdot\text{m}^2$ )**

$$\mathbf{I}_{\text{output}} = \begin{bmatrix} 291.55 & 0.03 & 21.52 \\ 0.03 & 625.66 & -0.04 \\ 21.52 & -0.04 & 484.12 \end{bmatrix}$$

For a spinning spacecraft with antisymmetric principal moments of inertia ( $I_x \neq I_y$ ), the nutation frequency is given by:

$$\omega_n^2 = \Omega^2 \times \frac{(I_z - I_x)(I_z - I_y)}{I_x I_y}$$

Given:

$$I_x = 289.18 \text{ kg} \cdot \text{m}^2, \quad I_y = 486.50 \text{ kg} \cdot \text{m}^2, \quad I_z = 625.66 \text{ kg} \cdot \text{m}^2$$

and a spin rate of:

$$\Omega = 1 \text{ rad/s}$$

Substituting into the formula:

$$\begin{aligned} \omega_n^2 &= (1)^2 \times \frac{(625.66 - 289.18)(625.66 - 486.50)}{289.18 \times 486.50} \\ \omega_n^2 &= \frac{336.48 \times 139.16}{140701.57} \\ \omega_n^2 &= 0.3327 \end{aligned}$$

Thus:

$$\omega_n = \sqrt{0.3327} = 0.5772 \text{ rad/s}$$

Converting to cycles per second (Hz):

$$f_n = \frac{\omega_n}{2\pi} = \frac{0.5772}{6.2832} = 0.0918 \text{ Hz}$$

Therefore, the nutation frequency of the spacecraft model is approximately:

$$f_n = 0.092 \text{ Hz}$$

Using the antisymmetric form of the nutation frequency formula, the calculated nutation frequency is found to be approximately 0.092 Hz. In contrast, the first nonzero frequency identified in the effective mass participation table is approximately 0.5133 Hz. Although both frequencies represent low-frequency oscillations consistent with expected nutational behavior, the discrepancy between the calculated and observed values can be attributed to several factors. First, the analytical calculation assumes a perfectly rigid spacecraft with pure inertial properties and no elastic deformation, while the finite element model inherently includes elastic flexibility, which tends to stiffen the structure and elevate natural frequencies. Additionally, the effective mass participation analysis captures a coupled response that includes both rigid body-like nutation and structural flexure, leading to a higher effective dynamic stiffness than the purely rigid model predicts. Overall, the observed frequency remains consistent with the physical expectation of a low-frequency nutational mode. The elevation relative to the analytical prediction is reasonable given the more comprehensive modeling captured in the finite element analysis.

### 6.2.3 Mode Shapes

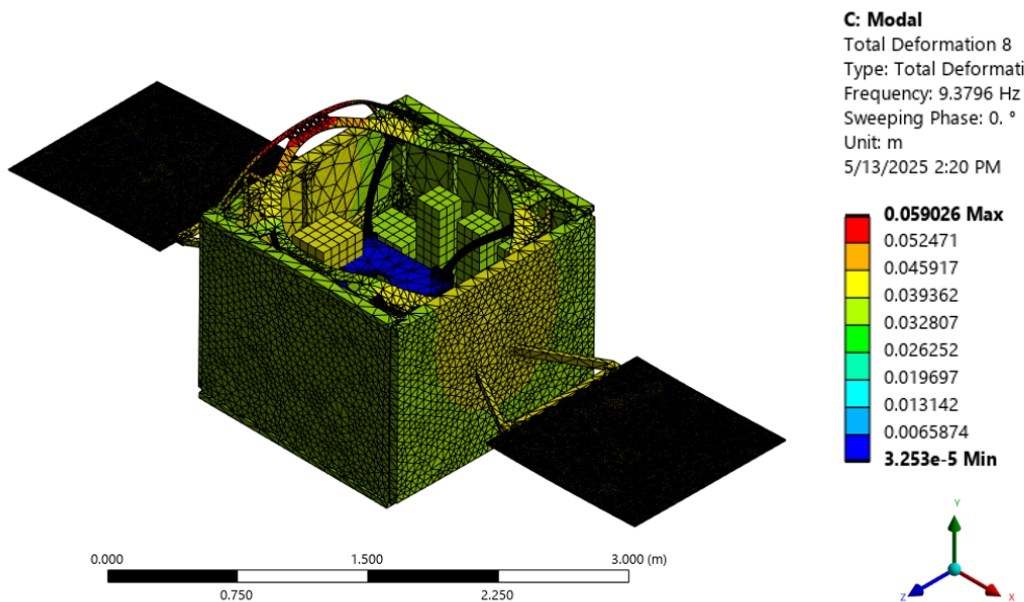


Figure 40: 8<sup>th</sup> Normal Mode for Constant-Spin Model

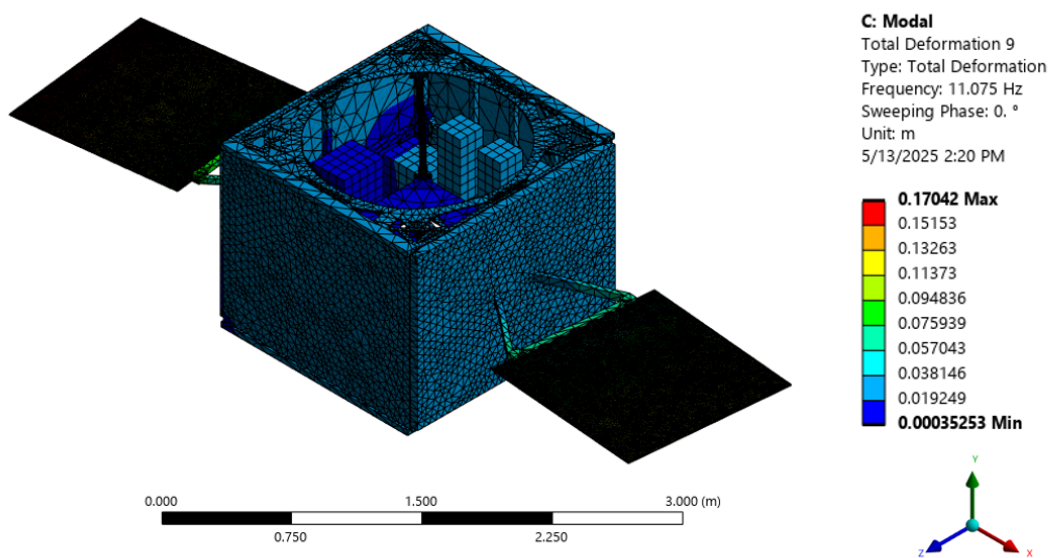
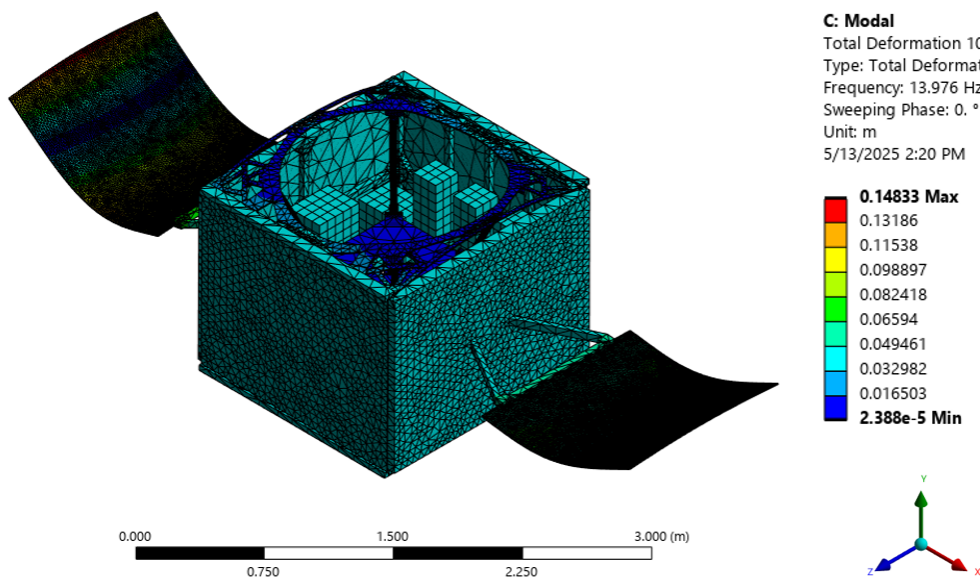
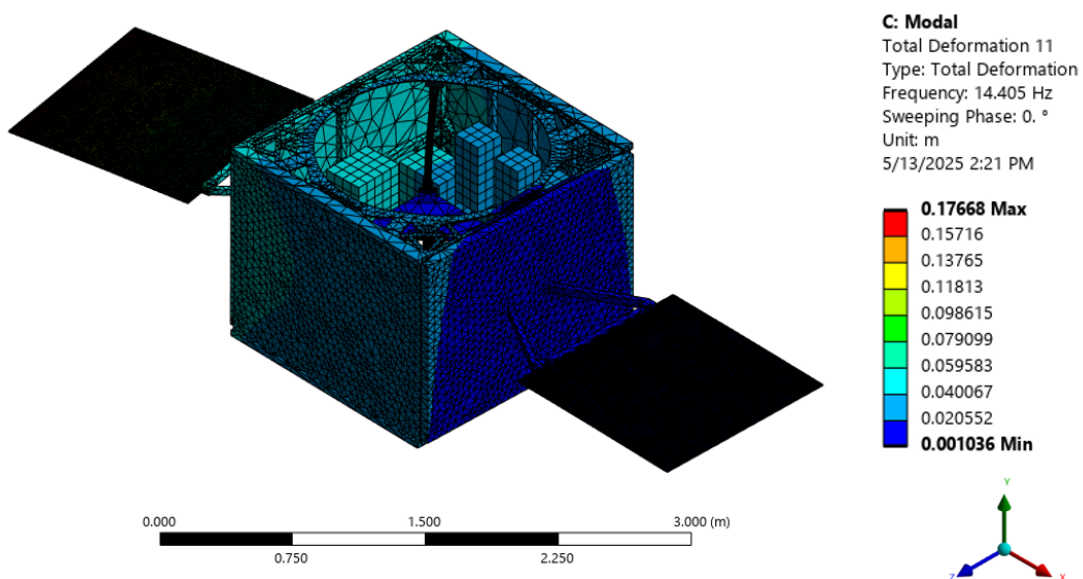


Figure 41: 9<sup>th</sup> Normal Mode for Constant-Spin Model

Figure 42: 10<sup>th</sup> Normal Mode for Constant-Spin ModelFigure 43: 11<sup>th</sup> Normal Mode for Constant-Spin Model

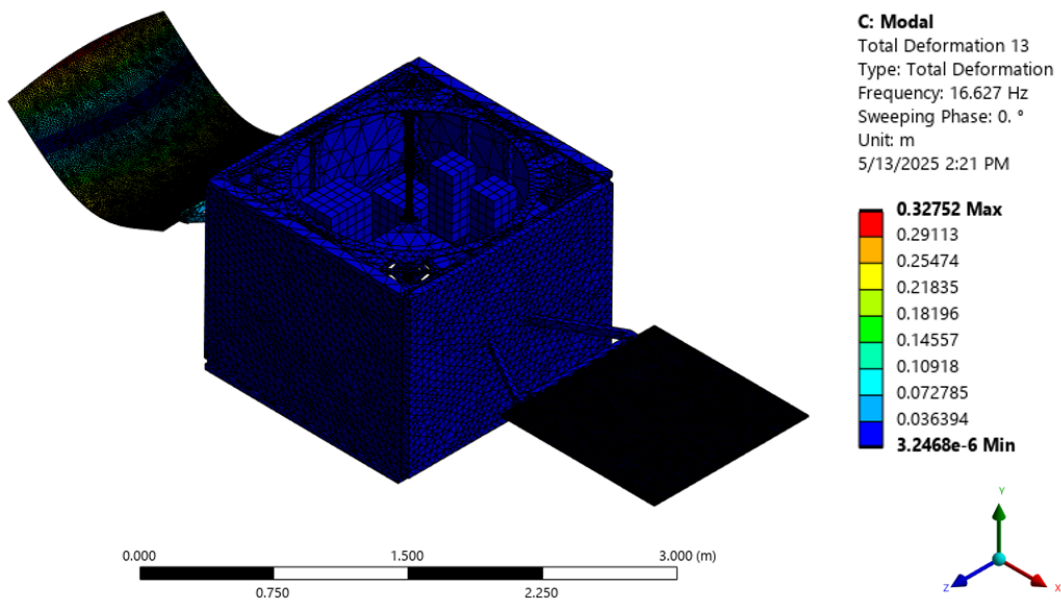


Figure 44: 13<sup>th</sup> Normal Mode for Constant-Spin Model

The mode shapes that excite real motion in the system are nearly identical to the mode shapes which excite translational motion in the original modal analysis. To effectively compare the mode shapes of the original modal analysis and the constant-spin model, the quantities of interest are tabulated and plotted below:

Table 3: Comparison of maximum displacement and frequency for constant-spin and original modal analyses

Mode	Analysis Type	Frequency (Hz)	Max Displacement (m)
8	Constant Spin	9.3796	0.059026
	Original Modal	9.3796	0.059007
9	Constant Spin	11.075	0.17042
	Original Modal	11.075	0.17042
10	Constant Spin	13.976	0.14833
	Original Modal	13.977	0.14753
11	Constant Spin	14.405	0.17668
	Original Modal	14.405	0.17668
13	Constant Spin	16.627	0.32752
	Original Modal	16.646	0.32891

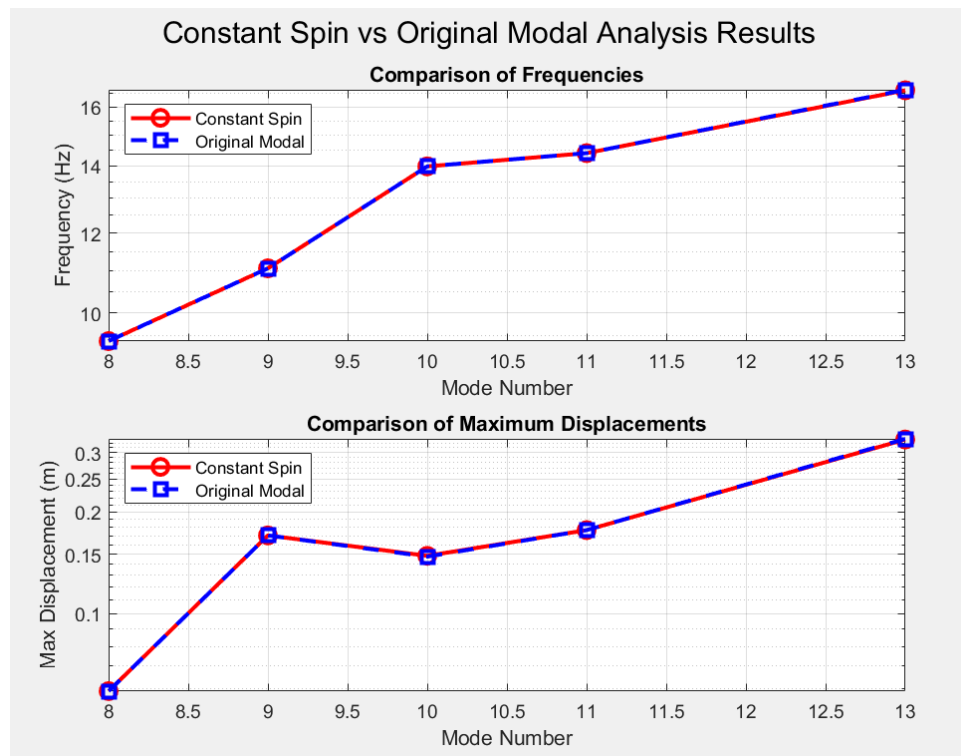


Figure 45: Plot of Constant-Spin vs. Original Modal Analysis Quantities of Interest

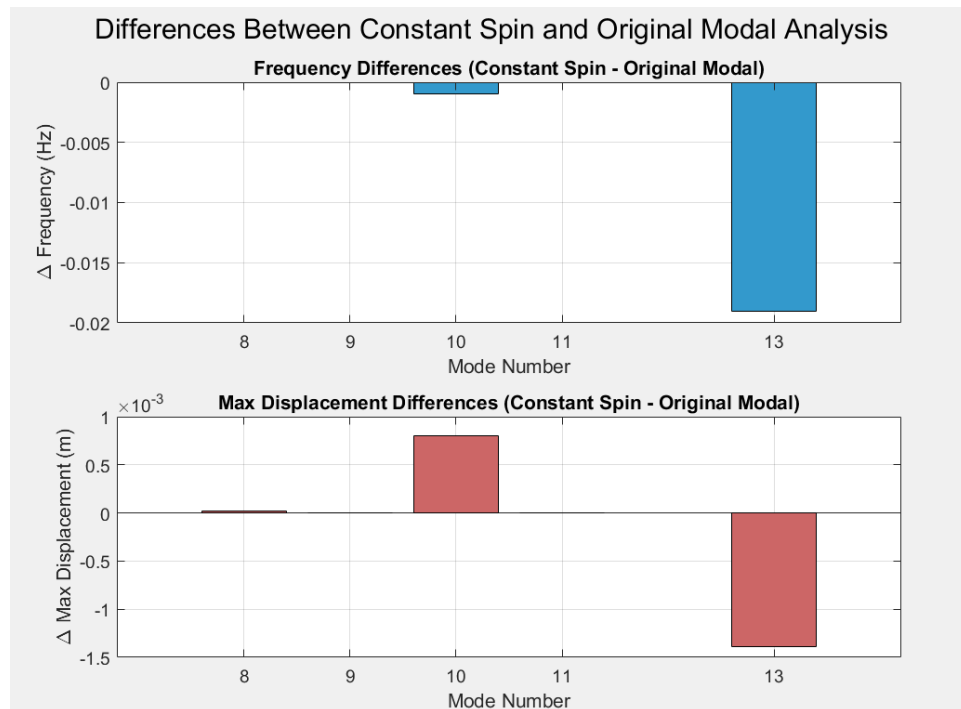


Figure 46: Difference of Constant-Spin vs. Original Modal Analysis Quantities of Interest

The comparison between the original modal analysis and the constant spin rate analysis reveals minimal differences in the quantities of interest, specifically the natural frequencies and maximum displacements of the mode shapes. Across all evaluated modes, the differences in frequency were observed to be on the order of  $10^{-3}$  Hz, while differences in maximum displacement were similarly negligible, typically on the order of  $10^{-4}$  meters. These small discrepancies are attributed to the relatively low spin rate applied in the constant spin analysis, set at 1 rad/s. At such a low angular velocity, gyroscopic effects are minimal, resulting in dynamic behavior that closely resembles the non-spinning configuration. This behavior, however, is similar to the physical conditions expected during experimental operations, where the spacecraft will experience slow rotational motion. As such, incorporating the spin rate into the modal analysis, even at low values, enhances the validity of the simulation and ensures that dynamic effects present during operational conditions are captured within the structural response. Furthermore, the small discrepancies between the original mode shapes and the constant-spin mode shapes attest to the fidelity of the original modal analysis, as the constant-spin analysis correctly characterizes a real physical behavior of the system.

### 6.3 Prestressed Modal Analysis Results

This section presents the results of the static structural and modal analyses performed to characterize the mechanical behavior of the system under thrusting conditions. A static structural analysis is first conducted to establish the preloaded state of the structure under the applied boundary conditions and external loads. The resulting stress and deformation fields are used to capture any stiffness modifications due to loading. This is critical for an accurate assessment of the dynamic response of the system. A modal analysis is performed, incorporating the prestressed condition as determined by the static solution. This approach ensures that the influence of initial stresses on the natural frequencies and mode shapes is appropriately captured, providing a more realistic prediction of the vibrational characteristics of the large-scale structure.

### 6.3.1 Discussion on Sagging

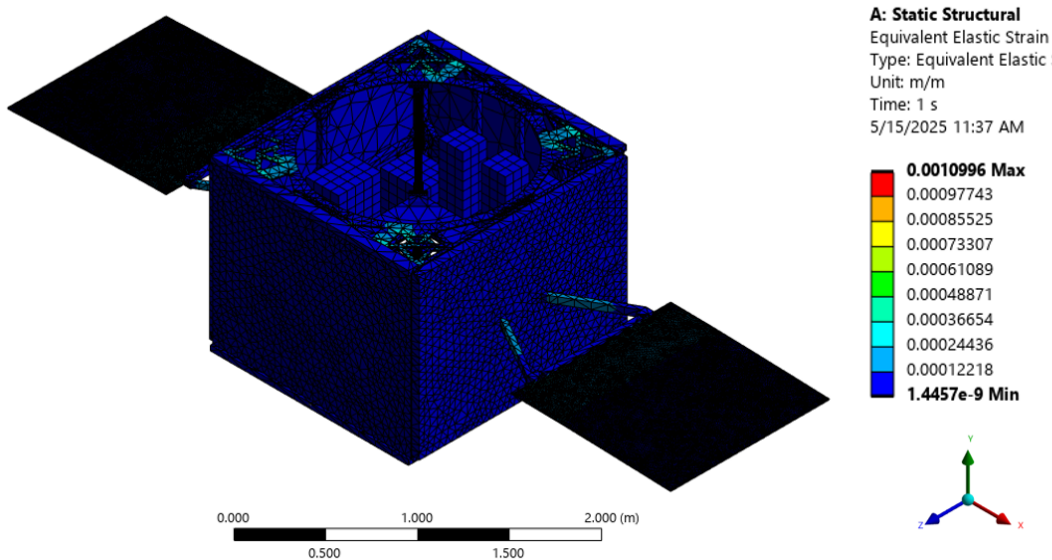


Figure 47: Strain Results from Gravitational Loading

To further assess the validity of the structure, a separate Static Structural analysis is performed neglecting the forces from the thrusters. Thus, the satellite model is gravitationally loaded with the same remote displacement boundary condition as the other analyses. The equivalent elastic strain distribution indicates that the majority of the deformation is concentrated at the structural interfaces between the central bus and the solar panel mounting points. The maximum equivalent strain observed, approximately  $1.1 \times 10^{-3}$  m, occurs along these critical load-bearing regions, suggesting localized flexural deformation due to gravitational and thrust-induced forces. This sagging effect is characteristic of a structure with large, flexible appendages supported by a relatively rigid central core. The solar arrays, due to their significant moment arms and comparatively low bending stiffness, impose downward loading on the supporting bus structure, leading to measurable out-of-plane deflections and strain concentrations. The magnitude of the strain displacements remain low, however. A typical value of concern for maximum strain displacement under gravitational loading is  $1.0 \times 10^{-2}$  m. Ultimately, the sagging observed is consistent with expectations for large spacecraft with flexible extensions.

### 6.3.2 Effective Mass Ratio Tables

In accordance with the initial modal analysis performed, the effective mass ratio tables are shown below to analyze which mode shapes contribute to the overall behavior:

Mode	Frequency [Hz]	X Direction	Y Direction	Z Direction
1	3.0464	3.451e-008	1.5122e-002	6.0991e-007
2	3.2907	7.5122e-006	3.9679e-002	3.0095e-007
3	5.8174	8.5479e-005	5.7646e-006	1.6575e-004
4	7.6037	3.5249e-004	1.0145e-006	7.1107e-005
5	8.1161	8.9419e-005	3.5441e-006	1.3598e-005
6	8.5908	2.0206e-003	1.8744e-004	2.0481e-004
7	9.2476	1.1367e-002	3.079e-003	1.3386e-004
8	9.986	0.87541	1.1692e-002	1.9805e-004
9	11.164	5.0927e-004	5.6382e-005	0.4992
10	14.64	2.8434e-003	0.11714	0.30619
11	14.685	9.8113e-003	0.44179	8.1184e-002
12	16.179	1.133e-007	3.6947e-005	2.4844e-002
13	17.181	2.6601e-003	0.21345	7.4353e-005
14	19.014	4.299e-004	2.1988e-002	2.4306e-007
15	26.653	7.7277e-010	6.5166e-011	7.7044e-008
16	27.338	5.6639e-007	1.4401e-004	1.8863e-008
17	27.604	2.4014e-006	8.3805e-005	6.949e-012
18	28.633	6.5323e-009	2.8416e-007	3.8864e-008
19	38.16	3.5726e-005	2.8366e-005	1.4967e-008
20	38.533	1.7714e-003	2.665e-003	1.8792e-011
21	39.07	2.8982e-004	6.0885e-003	4.1883e-008
22	39.218	2.6138e-003	5.6042e-004	1.6465e-011
23	42.111	2.6235e-007	4.7194e-006	1.0711e-007
24	42.364	1.0387e-006	6.3137e-005	2.23e-008
25	48.957	7.1534e-008	2.8703e-008	9.3114e-008
26	51.529	1.0349e-004	7.4988e-007	7.3029e-005
27	52.029	7.6901e-004	4.3479e-006	1.8013e-005
28	53.374	1.4316e-007	1.4767e-007	2.0732e-009
29	53.583	1.7637e-007	7.5658e-008	8.0282e-009
30	54.996	4.5845e-007	6.2833e-007	7.8725e-007
Sum		0.91118	0.87388	0.91238

Figure 48: Translational Direction of Prestressed Effective Mass Table

Mode	Frequency [Hz]	Rotation X	Rotation Y	Rotation Z
1	3.0464	5.0594e-005	3.132e-006	0.30458
2	3.2907	2.6893e-005	1.1897e-006	0.11721
3	5.8174	3.5382e-003	0.96704	1.2193e-004
4	7.6037	0.55016	2.5978e-003	1.3487e-002
5	8.1161	5.3368e-002	1.8723e-004	3.6872e-003
6	8.5908	0.27234	8.8111e-004	8.2226e-002
7	9.2476	9.536e-002	4.2007e-005	0.4394
8	9.986	3.7961e-005	8.3986e-005	1.3703e-002
9	11.164	1.0044e-003	1.3186e-003	9.1103e-005
10	14.64	5.1662e-004	1.7447e-003	6.8675e-005
11	14.685	4.8111e-005	4.776e-004	2.0748e-007
12	16.179	8.851e-006	1.2516e-002	1.0931e-007
13	17.181	1.0874e-004	1.2771e-006	6.9381e-003
14	19.014	2.6313e-005	2.6272e-007	3.7677e-003
15	26.653	2.7688e-005	7.2886e-008	2.1352e-007
16	27.338	2.5724e-007	7.157e-010	2.7372e-005
17	27.604	2.618e-007	4.3426e-009	4.514e-005
18	28.633	2.0689e-005	1.1334e-009	3.0025e-007
19	38.16	4.3188e-007	2.0977e-009	1.0341e-004
20	38.533	4.8558e-009	5.0484e-008	3.7077e-005
21	39.07	7.2602e-008	4.9957e-009	1.9003e-005
22	39.218	3.6664e-009	9.9444e-010	1.9269e-004
23	42.111	2.0981e-007	1.5804e-006	5.0312e-006
24	42.364	2.5738e-007	9.3381e-008	4.3322e-005
25	48.957	1.4676e-006	3.116e-008	4.1457e-009
26	51.529	1.869e-007	1.7226e-007	1.4253e-010
27	52.029	2.5071e-008	3.3111e-007	7.391e-007
28	53.374	6.7487e-010	6.0749e-012	6.2926e-008
29	53.583	7.1386e-010	2.7661e-011	9.0476e-008
30	54.996	3.7732e-006	5.18e-007	1.626e-007
Sum		0.97665	0.98689	0.98575

Figure 49: Rotational Direction of Prestressed Effective Mass Table

A few differences are present between the effective mass ratio tables for the original Ansys modal analysis and the prestressed version. First, it is noted that the three rotational rigid body natural frequencies are not longer present in the new effective mass tables. Although the model is free to rotate around the remote displacement node at the center of rotation, the rigid body modes no longer exist due to the spring loading on the model. Furthermore, the sum of the rotational effective mass ratios no longer sum to 1, the total mass of the



structure. This is also constrained by the spring loading on the plane of the bottom isogrid. Consequently, there are now modes corresponding to the rotational excitation about one of the three principal axes. The first, second, and seventh normal mode are responsible for a significant excitation about the  $z$ -axis, with effective mass ratios of 0.3046, 0.1172, and 0.4394, respectively. The rotation about the  $x$ -axis is mainly excited by the fourth and sixth natural modes of frequency, with respective effective mass ratios of 0.5502 and 0.2723. The rotational excitation about the  $y$ -axis is dominated by the third natural mode of frequency at an effective mass ratio of 0.9670.

### 6.3.3 Mode Shapes

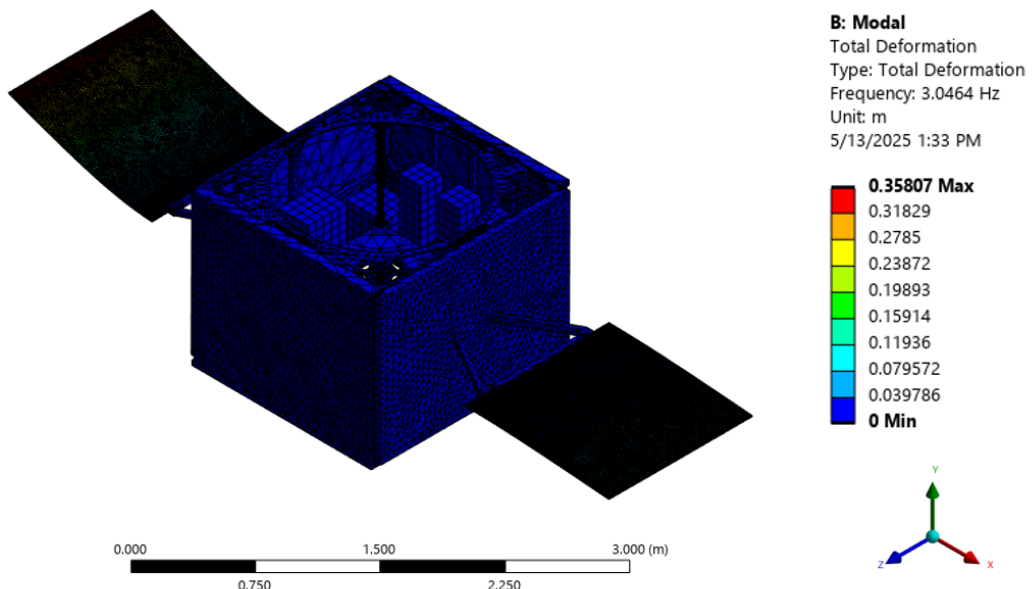
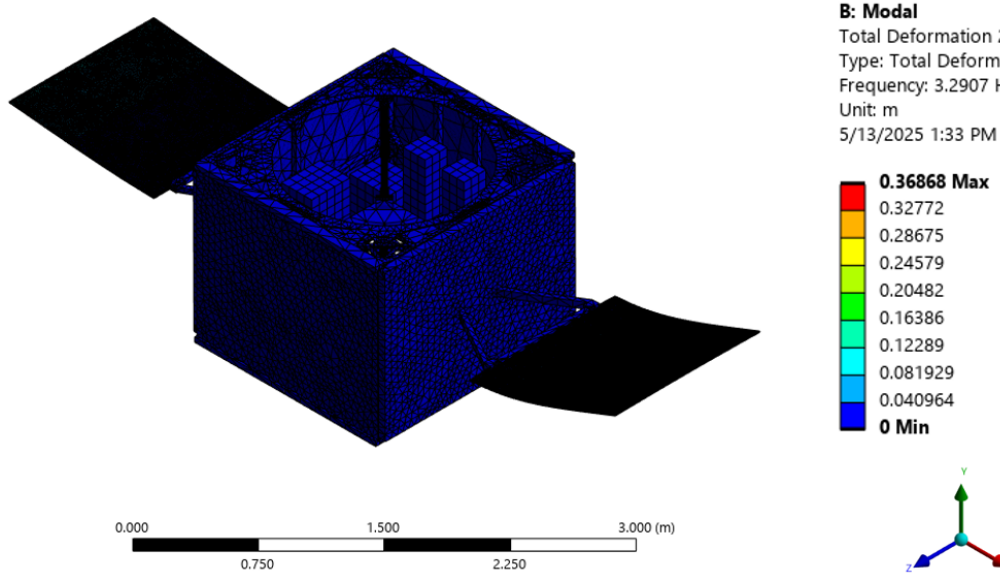
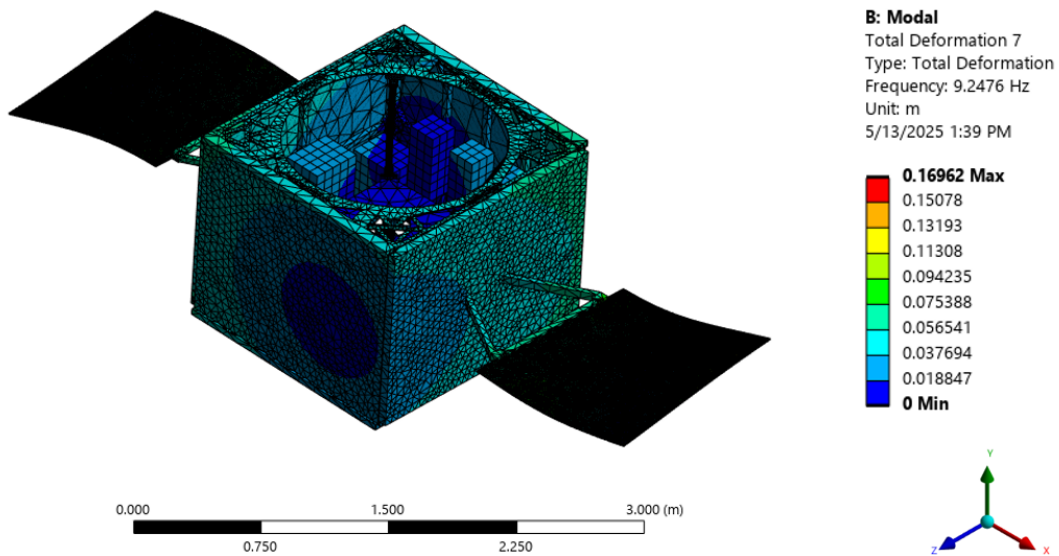


Figure 50: 1<sup>st</sup> Normal Mode for Prestressed Model

Figure 51: 2<sup>nd</sup> Normal Mode for Prestressed ModelFigure 52: 7<sup>th</sup> Normal Mode for Prestressed Model

The first mode shape obtained from the prestressed modal analysis occurs at a frequency of 3.0464 Hz. The deformation pattern clearly indicates that this mode is dominated by bending of the solar panels, while the spacecraft bus remains largely rigid. The maximum deformations are concentrated at the tips of the solar arrays, with a maximum deformation of 0.358 meters. This behavior confirms that the solar panels act as the primary flexible

elements of the system. The ‘flapping’ of the solar panels is responsible for the rotation about the  $z$  axis. The prestressing applied during the static structural step influences the overall stiffness of the panel mounting points, slightly modifying the dynamic characteristics compared to an unstressed configuration. The absence of rigid body modes near 0 Hz suggests that either boundary conditions or rotational spring stiffness have been introduced to sufficiently restrain free translation and rotation, effectively shifting these modes to higher frequencies or replacing them with deformable system modes. The second natural mode of frequency is similar to the first as it is mainly influenced by the bending of the solar panels; however, in this mode, both panels flex in the positive  $y$  direction. Similar to the first mode, the maximum deflection occurs along the edges of the solar panels with a value of 0.3689 meters. The seventh natural mode of frequency occurs at a frequency of 9.2476 Hz. This mode shape differs from the first two in the fact that the satellite bus deforms along with the solar panels. The maximum deflection still occurs at the edges of the solar panels with a value of 0.1696 meters.

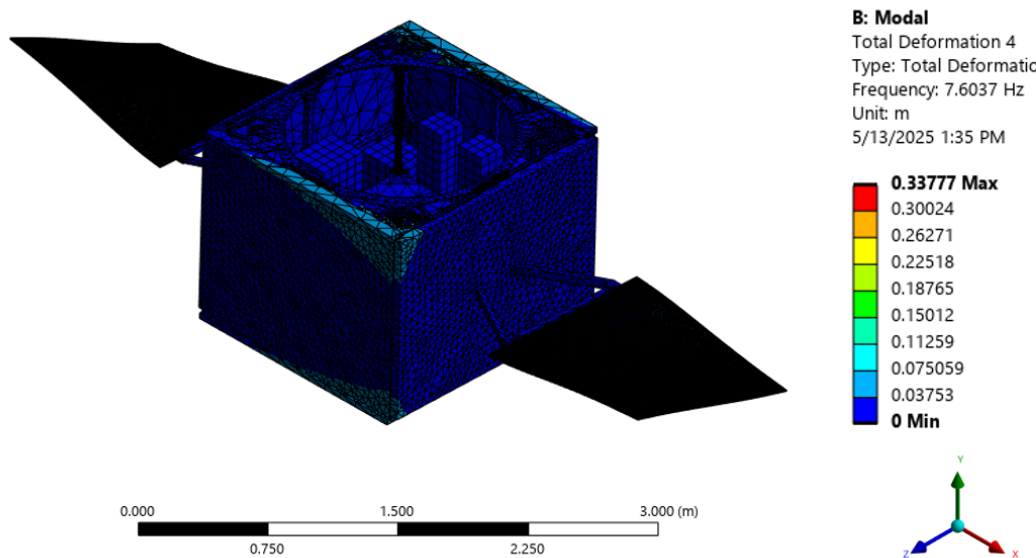


Figure 53: 4<sup>th</sup> Normal Mode for Prestressed Model

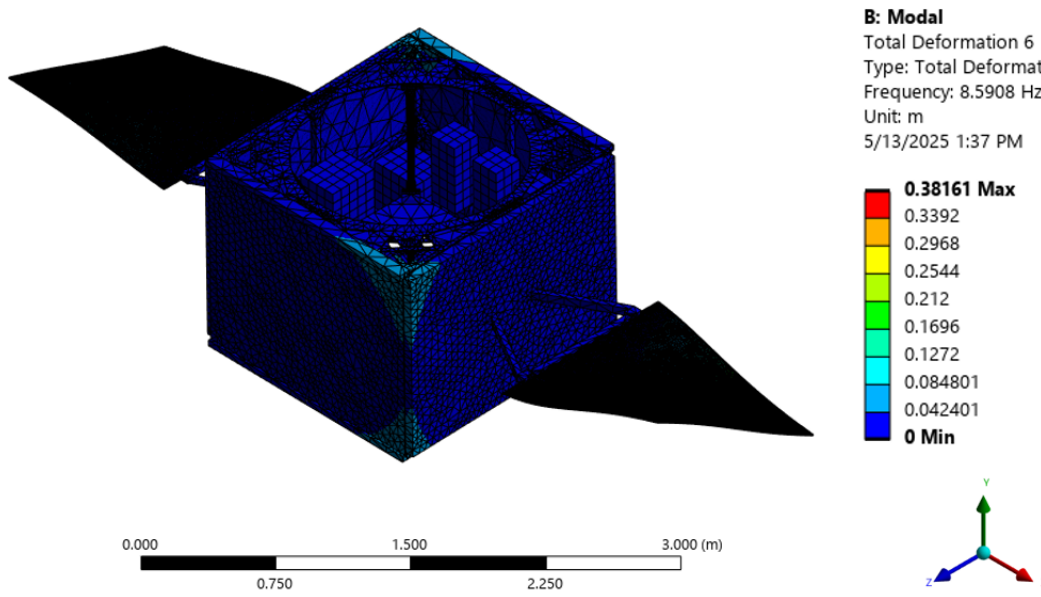


Figure 54: 6<sup>th</sup> Normal Mode for Prestressed Model

The fourth and sixth mode shapes, occurring at 7.6037 Hz and 8.5908 Hz respectively, exhibit significant contributions to rotational excitation about the spacecraft's  $x$ -axis. In the fourth mode, the dominant deformation occurs in the solar panels, which flex asymmetrically along the  $y$ -axis. The maximum deflection of 0.33777 meters is observed at the tips of the solar panels, indicating that these appendages serve as the primary drivers of dynamic response in this mode. The asymmetric  $y$ -direction motion of the panels, mounted symmetrically along the  $x$ -axis, generates a net pitching moment about the spacecraft's longitudinal  $x$ -axis. Similarly, the sixth mode, with a maximum deflection of 0.38161 meters also located at the solar panel tips, shows a more complex deformation pattern involving combined  $y$  and  $z$ -direction displacements. Despite this added complexity, the motion still produces a substantial pitching moment about the  $x$ -axis due to differential motion between the panels relative to the center of mass. In both modes, the large spatial offset of the panels amplifies the rotational coupling, leading to notable rotational effective mass participation about the  $x$ -axis.

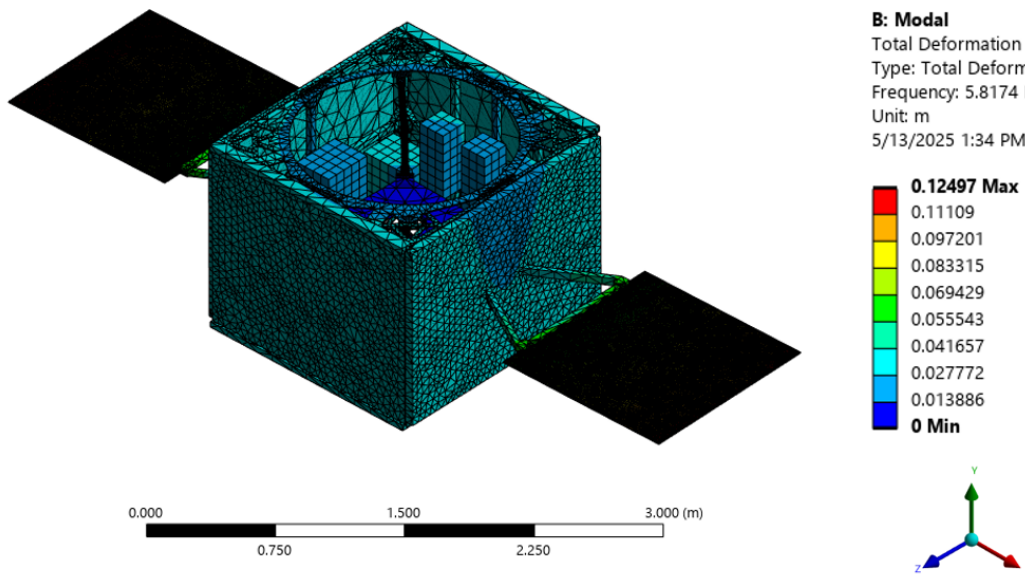


Figure 55: 3<sup>rd</sup> Normal Mode for Prestressed Model

The third natural mode exhibits a dominant contribution to rotational excitation about the  $y$ -axis, with an effective mass participation ratio of 0.9670. In the prestressed model, this mode occurs at a frequency of 5.8174 Hz. The displacement contour of the third mode shape reveals a steadily increasing displacement of the satellite bus components extending from the bearing plate, indicative of a pure rotational motion about the  $y$ -axis. This behavior suggests that inertial forces generated by the rotation are displacing the structural components radially outward from the axis of rotation. The maximum displacement is observed along the edges of the solar panels, reaching a value of 0.12497 meters.

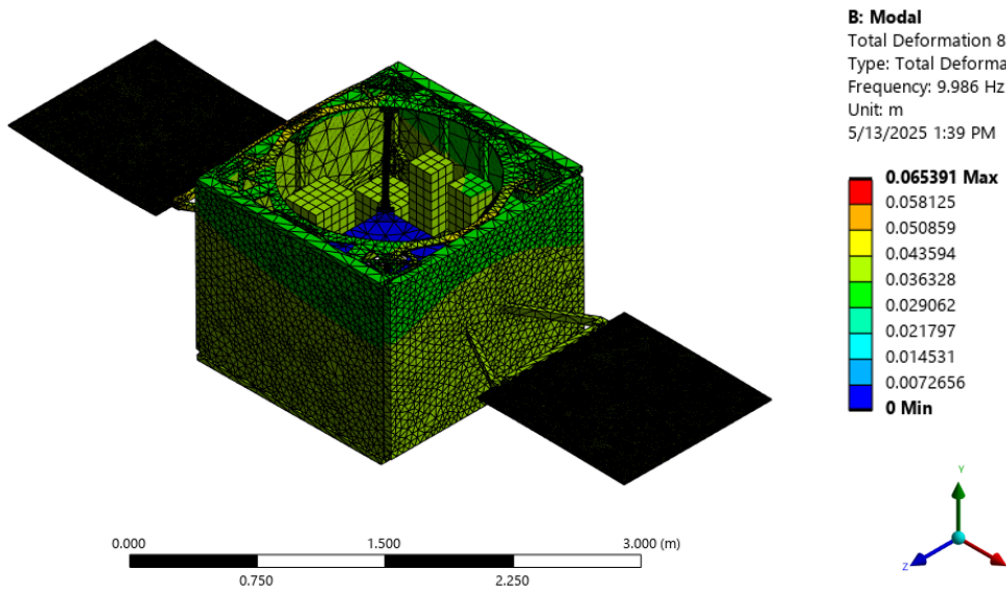


Figure 56: 8<sup>th</sup> Normal Mode for Prestressed Model

The eighth natural mode of frequency is responsible for 87.54% of the translational motion along the  $x$ -axis. Similar to the third natural mode of the prestressed model, the eighth mode shape is described by uniformly increasing displacement of the large-structure extruding from the bearing plate. The maximum deformation occurs along the outer edges of the solar panels, reaching a deformation of 6.539 cm. The eighth natural mode of frequency causes the largest elongation along the  $x$ -axis.

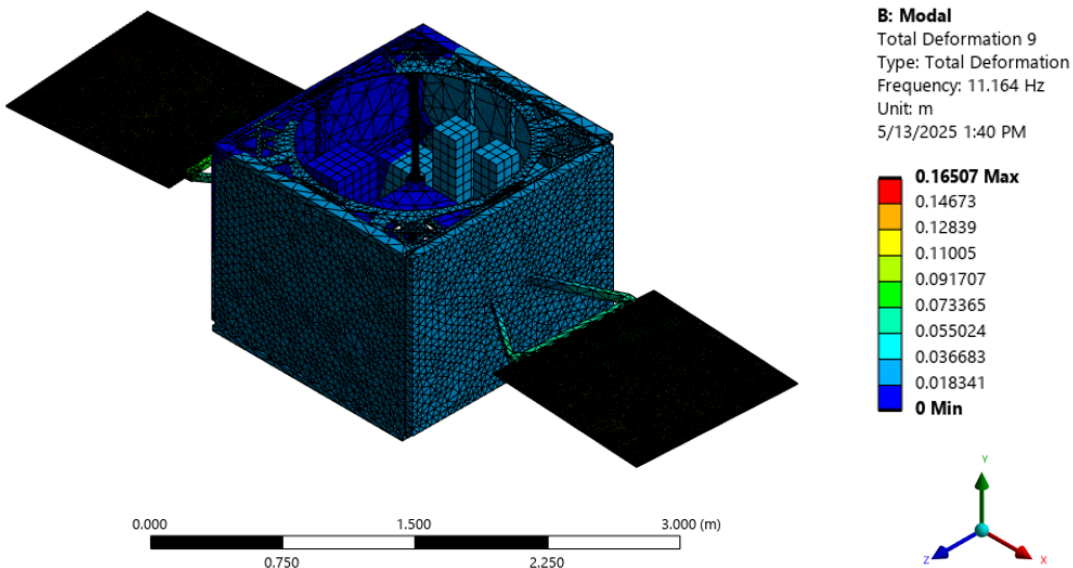


Figure 57: 9<sup>th</sup> Normal Mode for Prestressed Model

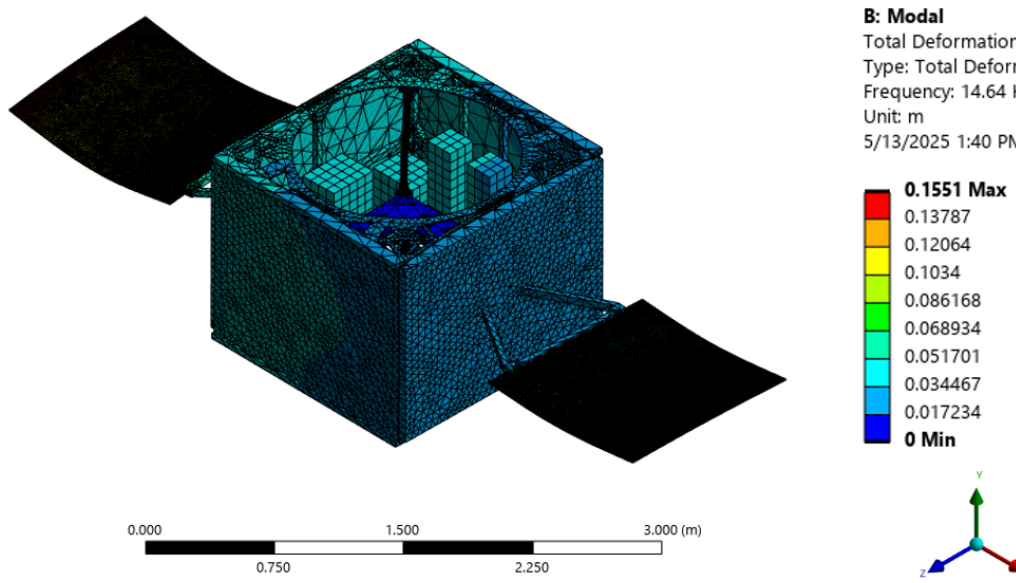
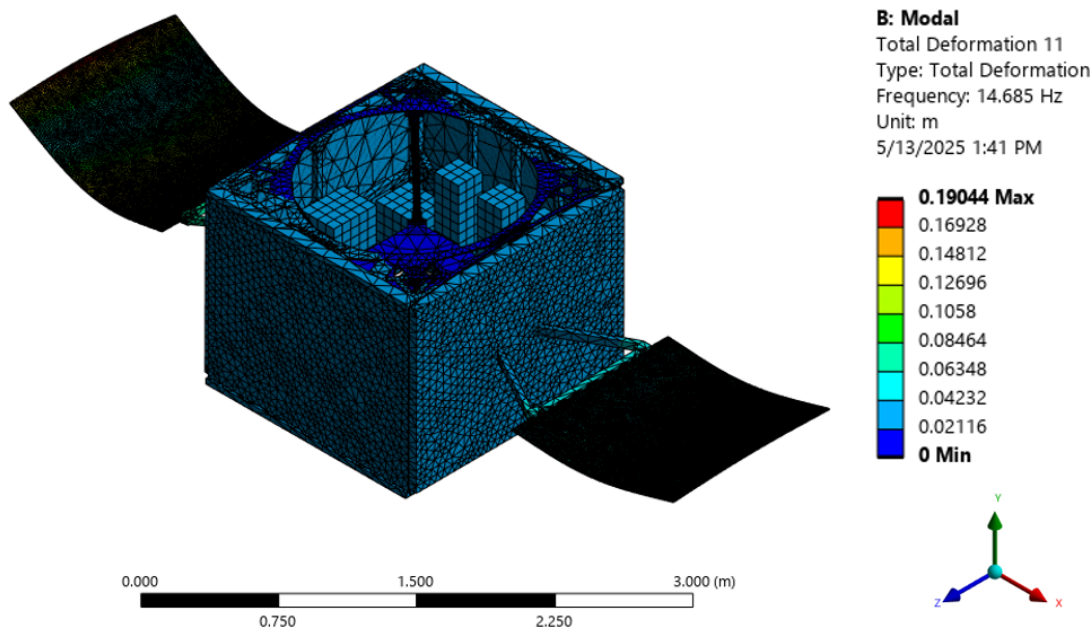
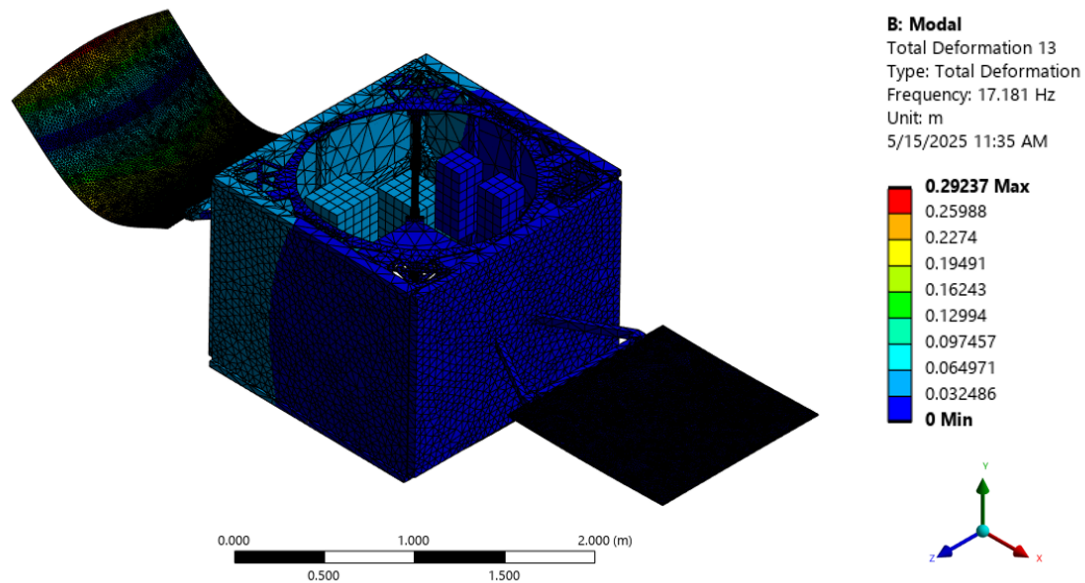


Figure 58: 10<sup>th</sup> Normal Mode for Prestressed Model

The ninth and tenth natural modes of the prestressed model significantly contribute to the translational motion of the satellite model along the  $z$ -axis, with effective mass ratios of 0.4992 and 0.3062, respectively. The ninth mode occurs at a frequency of 11.164 Hz and shows a predominantly symmetric deformation pattern concentrated in the spacecraft bus. The displacement contour indicates a uniform upward displacement of the bus structure, with minimal rotational components, resulting in a strong translational excitation along the  $z$ -axis. The maximum displacement for this mode is 0.16507 meters, occurring along the upper edges of the spacecraft body. Similarly, the tenth mode, occurring at a frequency of 14.64 Hz, demonstrates symmetric deformation, although with slightly greater involvement of the solar panels. Despite this added complexity, the dominant motion remains in the  $z$ -direction, contributing substantially to vertical translation. The maximum displacement for the tenth mode is 0.1551 meters, also located near the upper surfaces of the spacecraft bus. Overall, both modes reinforce the spacecraft's susceptibility to translational excitation along the  $z$ -axis at these frequencies.

Figure 59: 11<sup>th</sup> Normal Mode for Prestressed ModelFigure 60: 13<sup>th</sup> Normal Mode for Prestressed Model

The tenth, eleventh, and thirteenth natural mode shapes contribute to the translational excitement along the  $y$ -axis at respective percentages of 11.71%, 44.18%, and 21.35%.

The tenth mode occurs at a frequency of 14.64 Hz and primarily involves symmetric deformation of the spacecraft bus, accompanied by moderate flexure of the solar panels. The displacement field reveals a dominant upward displacement of structural elements along the  $y$ -axis, with a maximum displacement magnitude of 0.1551 meters concentrated at the edges of the solar arrays. Similarly, the eleventh mode occurs at a frequency of 14.685 Hz and demonstrates a more pronounced flexure in the solar panels while maintaining overall symmetry. The maximum displacement for the eleventh mode is 0.1904 meters, located near the tips of the solar panels. The thirteenth natural mode occurs at 17.181 Hz and is localized along the left (negative  $x$ -axis) side of the satellite model. The maximum deflection is 0.2924 meters along the edge of the left solar panel. In each case, the largely symmetric displacement patterns along the  $y$ -axis indicate strong translational excitation, with minimal rotational coupling into other degrees of freedom. As such, these modes contribute prominently to the vertical dynamic response of the spacecraft structure.

## 7. Conclusions and Recommendations

The three studies conducted are: freely-rotational modal analysis, constant-spin modal analysis, and prestressed modal analysis. The three studies aim to collectively describe the dynamic behavior of the system. The baseline modal analysis, performed without spin or prestress, reveals the fundamental vibrational behavior of the structure under free rotation about all principal axes. Subsequent constant spin rate analysis introduces a slow angular velocity of 1 rad/s about the  $y$ -axis. This analysis setup indicates physical behavior that the large-scale structure is capable of under experimental conditions. Prestressed modal analysis is conducted to simulate the influence of constant thrust forces and gravitational loading on the spacecraft structure. Furthermore, this analysis includes spring loading on the bottom plane of the outer structure to enforce the rotational constraints about the  $x$  and  $z$  axes. In all configurations, the three principal axes originate from the center of rotation of the structure, with the  $x$ -axis being the pitch axis,  $z$ -axis being the roll axis, and  $y$ -axis being the yaw axis.

The validity of the freely-rotational analysis is confirmed through the three rigid-body modes present in the results. The three rigid-body frequencies show that the model is fully bound translationally, as a fully unconstrained model has six rigid-body frequencies. Furthermore, none of the thirty extracted mode shapes contribute significantly to the rotational excitement of the large-scale structure. This evidence further substantiates the claim that the model is unbound in rotation. The effective mass ratio tables suggest that the structure is subject to translational excitement within the frequency range of 9.3796 Hz to 14.405 Hz. The mode shapes within this range include bus strain as well as flexure of the solar panels, the latter of the two contributing the most to deformation. The results of the freely-rotating modal analysis provide a comprehensive baseline for the natural dynamic response of the large-scale structure on the spherical air bearing.

The constant-spin modal analysis expands on the freely-rotating model by incorporat-

ing rotational effects. To simulate the gyroscopic environment accurately, the spacecraft model is transitioned from rigid to deformable, and incorporates Coriolis forces into the analysis settings. As a result, the modal results are expressed in terms of real and imaginary effective mass components, accounting for in-phase and out-of-phase inertial coupling. However, due to the relatively low spin rate, gyroscopic effects are negligible, resulting in imaginary effective mass components near zero and mode shapes that closely resemble those from the freely-spinning rigid body configuration. Differences in natural frequencies were found to be on the order of  $10^{-3}$  Hz, while maximum displacement variations were within  $10^{-4}$  meters. These discrepancies are insignificant from a practical standpoint. This validates the assertion that the dynamic response of the spacecraft will remain largely unaffected by slow spin rates, affirming the reliability of using baseline modal analysis predictions for low-speed rotational conditions. In further investigations, a maximum spin rate can be derived from the attitude control and propulsion subsystems. This spin rate can be substituted for the value of 1 rad/s in the constant-spin model to probe the intensity of gyroscopic effects under maximum loading.

The prestressed modal analysis is conducted to simulate the influence of thrust pulses and gravitational loading on the large-scale structure. The preloaded structure is established by applying static nodal forces mimicking propulsion system thrusts and introducing an equivalent spring stiffness to model rotational restrictions around the  $x$  and  $z$ -axes. The results of the prestressed modal analysis reveal a different behavior than the baseline freely-rotating model. First, the rigid body rotational modes are eliminated due to the introduction of restoring torques via the equivalent springs. New dominant modes emerge, characterized by coupling between bending and rotational behaviors. The coupled excitation exists within the frequency range of 3.046 Hz to 14.685 Hz. Despite negating the three rotational rigid-body frequencies, the first three mode shapes are still indicative of these modes, as they are constrained only by the springs on the bottom plane of the model. Disregarding the first three mode shapes, the excitation of the model lies within the frequency range of 7.604 Hz to 14.685 Hz.

The third natural mode of the prestressed configuration, occurring at 5.8174 Hz, exhibits strong rotational participation about the  $y$ -axis, with an effective mass participation ratio of 0.9670. The fourth and sixth modes are primarily responsible for rotational excitation about the  $x$ -axis, while the first, second, and seventh modes contribute significantly to rotation about the  $z$ -axis. The imposed static loads and artificial springs effectively anchor the spacecraft against free rotation, modifying the rotational low-frequency modal spectrum. Translational dynamics are also influenced by the prestressed configuration. The eighth mode, previously dominant in  $x$ -axis translation, continued to exhibit maximum displacement concentrated along the solar panels. However, the maximum displacement magnitude was slightly reduced compared to the free modal analysis. Similar behavior is observed for  $z$ -axis and  $y$ -axis translational modes, where the ninth, tenth, and eleventh modes capture the dominant vertical motion. The strong vertical motion in these modes suggests that the spacecraft bus and solar panels remain the most dynamically significant features of the structure even after loading.

Consistencies between the three analyses lead to conclusions about the dynamical response of the system. The large-scale structure exhibits excitation in a general frequency range of 7.604 Hz to 14.685 Hz. This range is typical for medium-sized satellites with large appendages such as solar panels. Many medium-sized spacecraft aim to reach their first natural frequency mode at 50 Hz to mitigate vibration in a launch setting [7] [10]. However, this behavior is usually achieved in a stowed configuration. The large-scale satellite is permanently in a deployed configuration, as the solar panels do not need to function in an experimental setting. The dynamic environment experienced by the spacecraft model is influenced by several operational disturbance sources inherent to typical satellite systems [11]. Thruster firings, particularly during attitude adjustment maneuvers, introduce low-frequency disturbances generally concentrated below 5 Hz [13]. While the primary structural modes of the spacecraft reside above this frequency range, repeated low-frequency thrust impulses have the potential to couple into flexible modes if sufficient excitation energy is present. This behavior should be accounted for in the attitude control system. Additionally, reaction wheels and control moment gyroscopes (CMGs), utilized for fine attitude control, introduce vibratory disturbances predominantly in the frequency range of 50–300 Hz. These disturbances arise from mechanical imbalances and rotational harmonics associated with the wheel or gimbal speeds. The natural frequencies of the satellite structure lie outside the principal harmonic bands of wheel-induced disturbances. The experimental conditions must consider the full spectrum of potential excitation sources to ensure that modal responses under operational loads remain within acceptable limits, thereby preserving structural integrity and maintaining precise attitude control throughout the mission.

In terms of model setup, several best practices are confirmed across the three analyses. The remote displacement boundary conditions simulate the spherical air bearing interface and provide realistic constraints while preserving rotational freedom. The application of the mesh refinement study in the solar panel regions ensures that results are mesh-independent and numerically reliable. Furthermore, the use of lumped mass approximations for complex subassemblies such as the control moment gyroscopes and propulsion system components effectively reduces computational load without sacrificing significant accuracy in the modes of interest. If computational power is not limited, it is in the best interest of the analysis to include the subassembly geometries. Furthermore, the modeling of the solar panel-to-bus connection can be refined to better capture local dynamics for higher frequency localized modes. Finally, gyroscopic effects were found to be negligible at 1 rad/s. Future studies considering higher spin rates may reveal stronger gyroscopic coupling effects, including mode splitting and precession behavior. Such effects could be critical for more dynamic mission profiles or alternative spacecraft designs involving faster rotation rates.

Across the three analyses, the mode shapes are significantly influenced by the solar array, particularly the solar panels. In both the free modal and prestressed analyses, the maximum displacements consistently occurred at the solar panel edges, demonstrating their critical role in shaping the structural flexibility of the system. Thus, if the excitation frequency range is found to be too low during experimental conditions, the profile of the

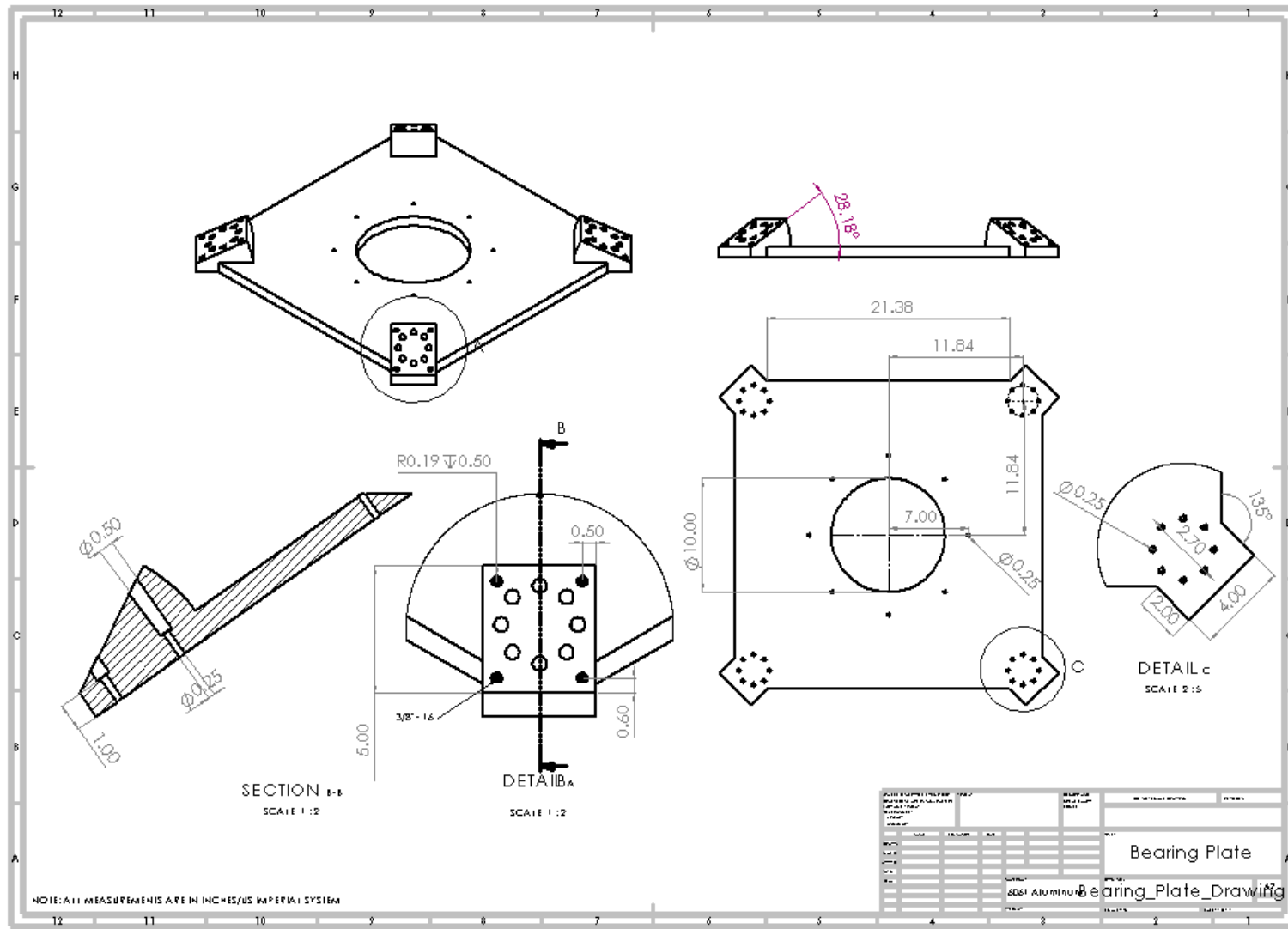
solar wing can be modified. For example, if the large-scale structure exhibits rotational excitation about the  $x$ -axis, it is likely due to the flexure of the solar panels. Therefore, the solar panel profile can be cut in half laterally to mitigate the response of the system. This procedure would change the solar panel from a 48 by 48 by 0.25 *in* prism to a 48 by 24 by 0.25 *in* prism. Refining the profile of the solar panels additionally benefits the ability to model different orbit procedures in the high bay. As seen in Appendix M, the original effective envelope of the interceptor satellite is heavily constrained by the volume of the translationally stationary satellite model. Refining the solar panels of both the chief and interceptor model allows for more translational freedom of the interceptor model. By cutting the solar panels in half laterally, a revised effective envelope is created, which can be seen in Appendix L.

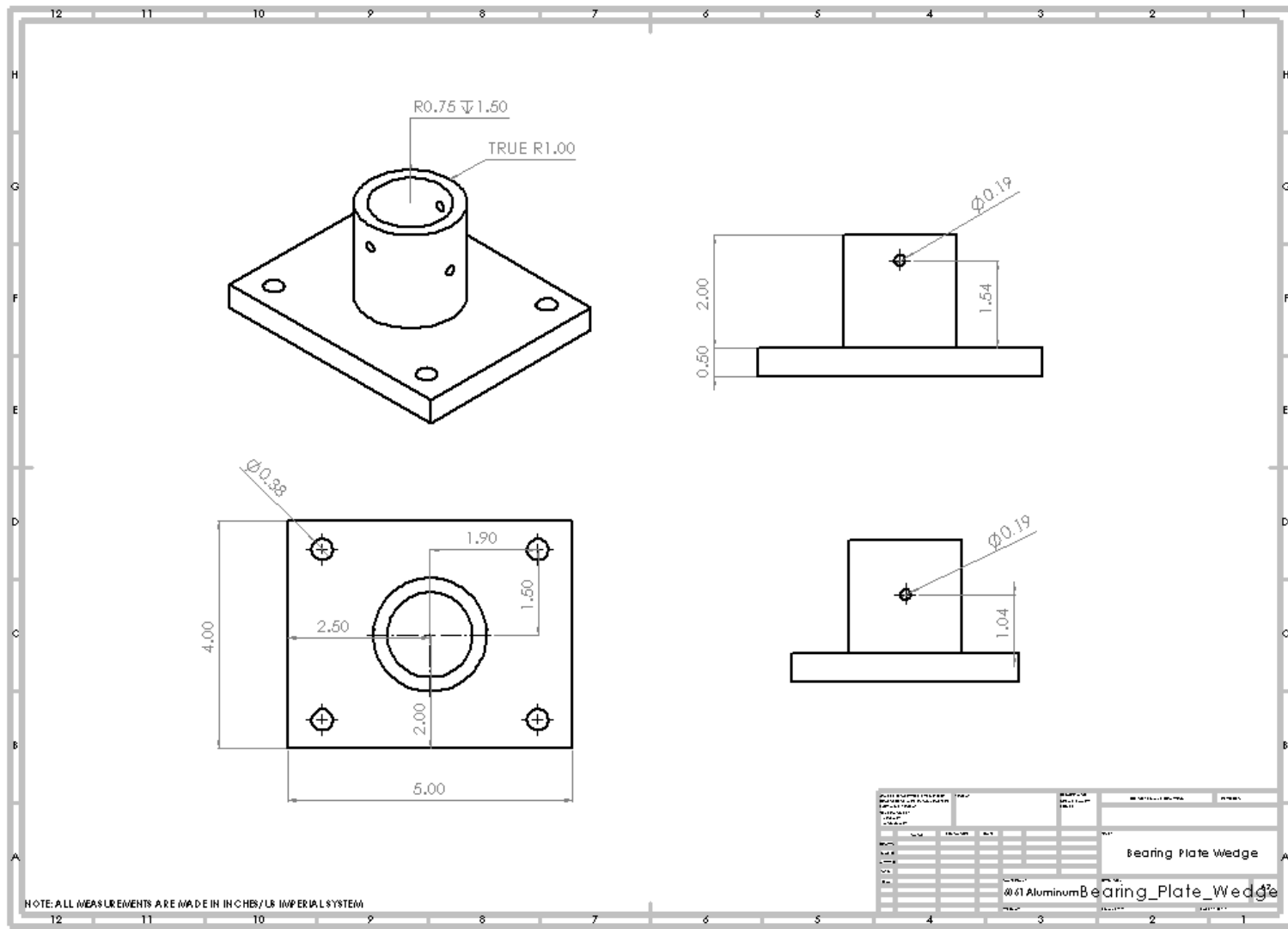
In terms of analysis, a few procedures are identified to properly describe the dynamic behavior of the large-scale structure under experimental conditions. As mentioned in the introductory trade study, the final design of the large-scale structure is prestressed through spring connections between the rods and wedge subassemblies in the inner structures. These connections are simplified to contact groups across all three analyses. For more accurate vibrational characteristics of the system, the spring loading should be accounted for at these joints. Furthermore, the connection of the isogrid to the outer structure is modeled by two edge connections in the modal analysis. Physically, this connection is more complex and is bound by the other two edges of the top and bottom profiles of the outer structure. The behavior of the system is directly influenced by this connection, as visible in the eighth normal mode shapes of the freely-rotating and constant-spin analyses. To accurately describe the dynamic behavior of the system, the connection of the isogrid to the outer structure should be refined further. To complement modal analysis, transient dynamic simulations incorporating thrust profiles and realistic damping estimates should be pursued. This provides a more accurate representation of time-dependent responses during maneuvering. Finally, the design of the large-scale structure should be validated through ground testing. Experimental modal analysis (EMA) should be conducted post-fabrication to validate key natural frequencies and mode shapes predicted in this report. Particular focus should be placed on verifying low-frequency modes that dominate translational and rotational motions.

In conclusion, this work provides a comprehensive dynamic characterization of the large-scale SDA spacecraft simulator. By incorporating realistic loading conditions, rotational effects, and structural prestress, the analysis offers high-accuracy predictions of modal behavior, informing future design improvements and operational experimental planning.

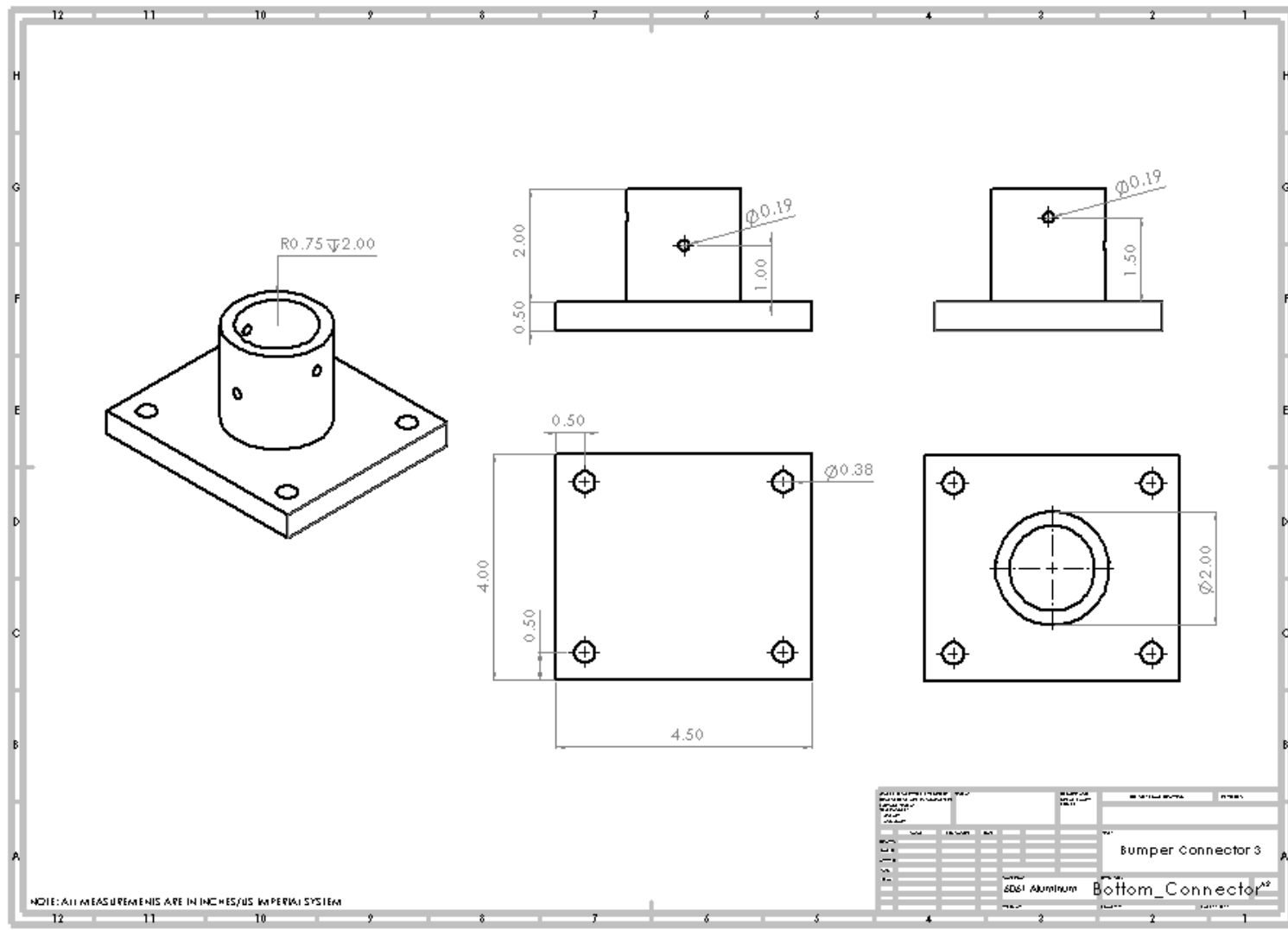
## 8. Appendices

This section details Appendices A-P and covers detailed drawings, MATLAB scripts, and Solidworks 3D models.

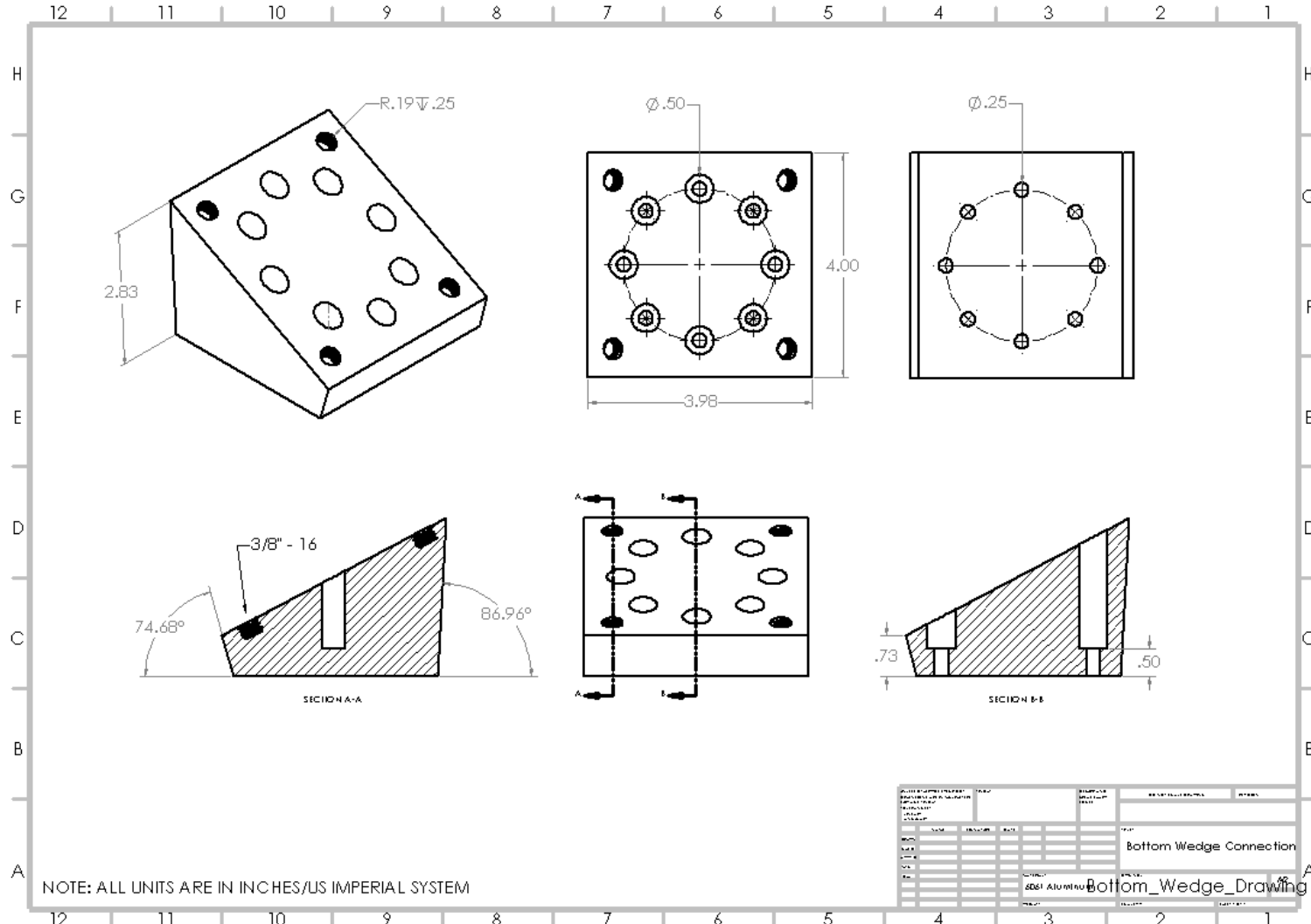




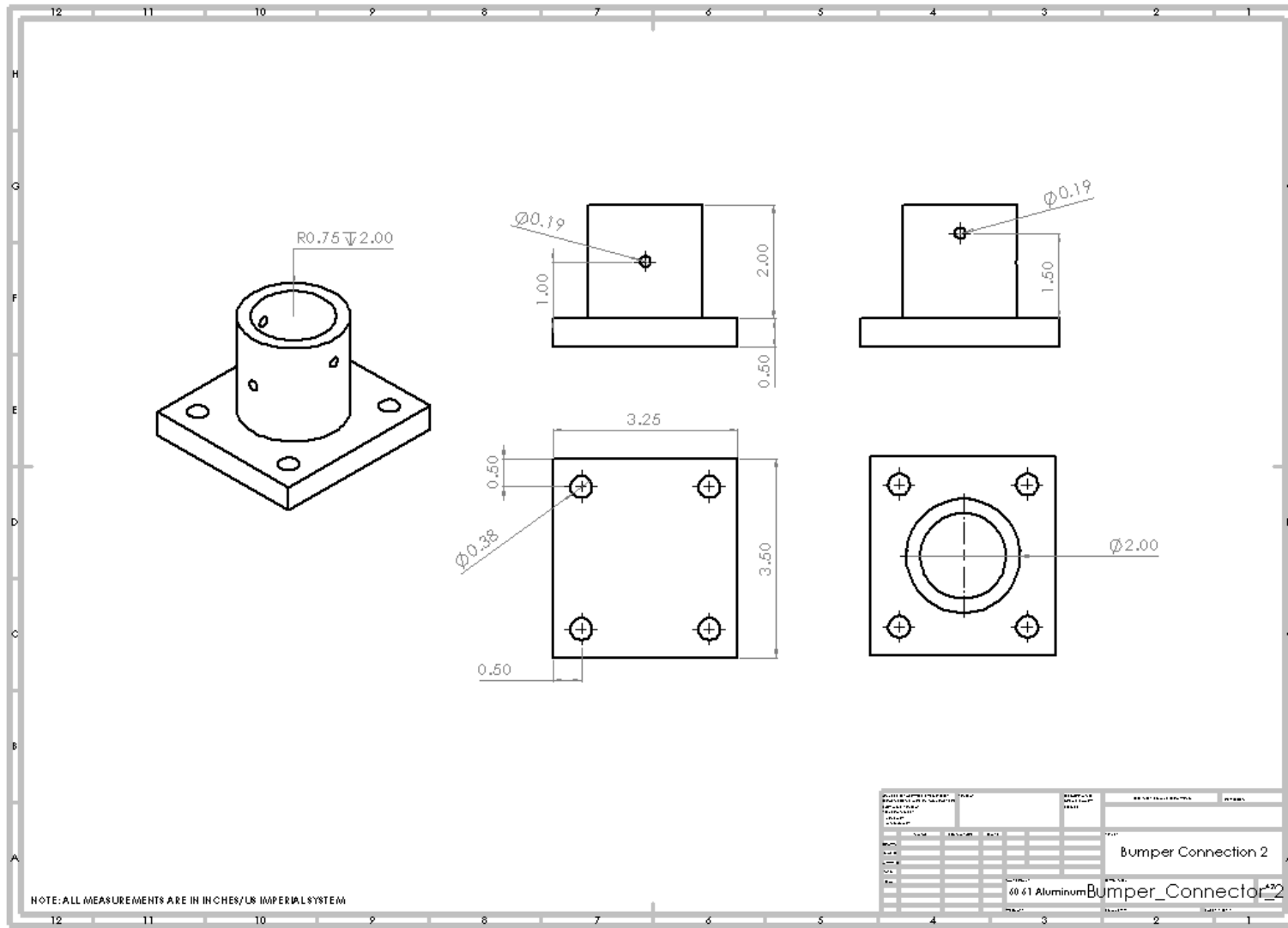
Cornell University

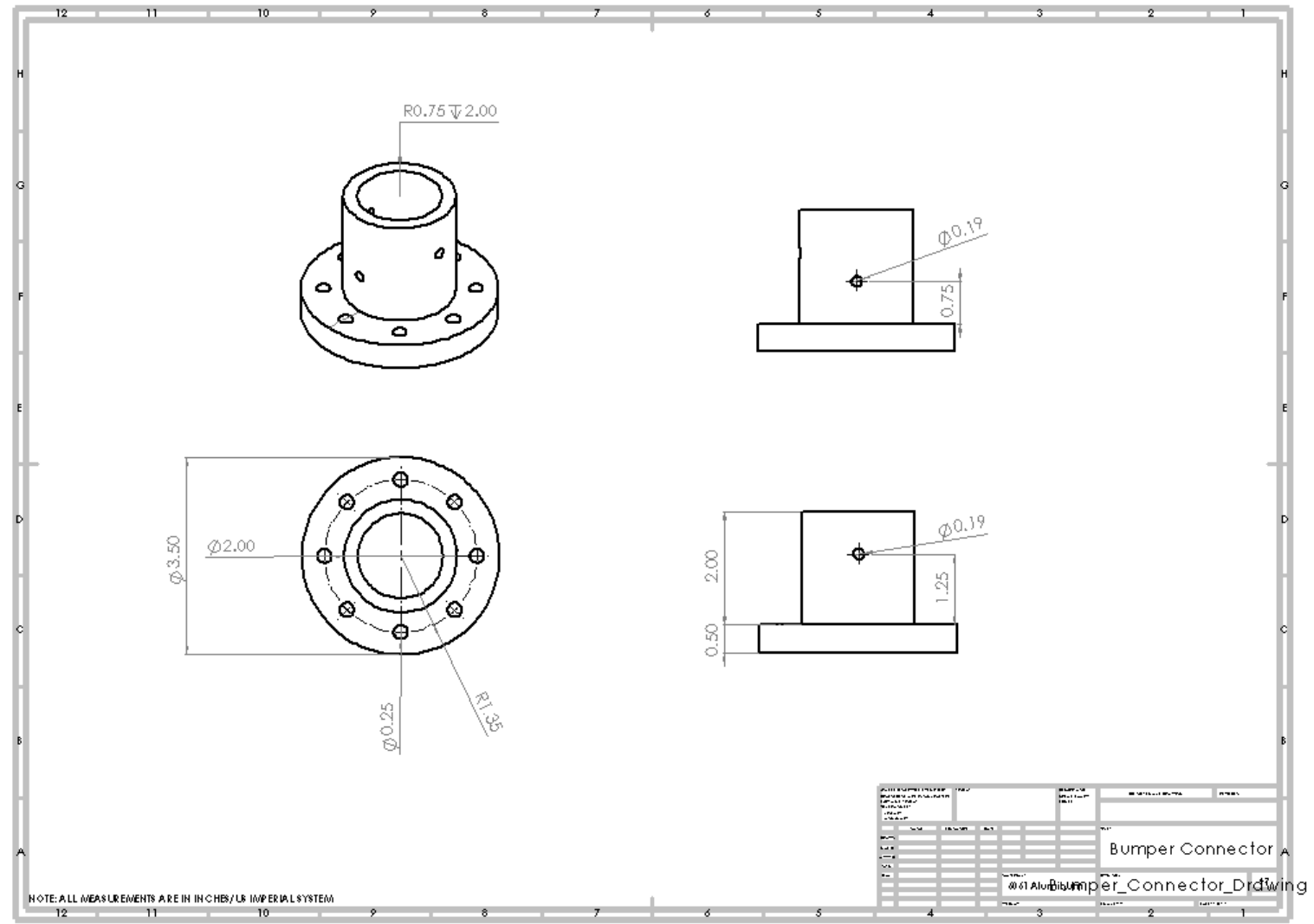


Cornell University

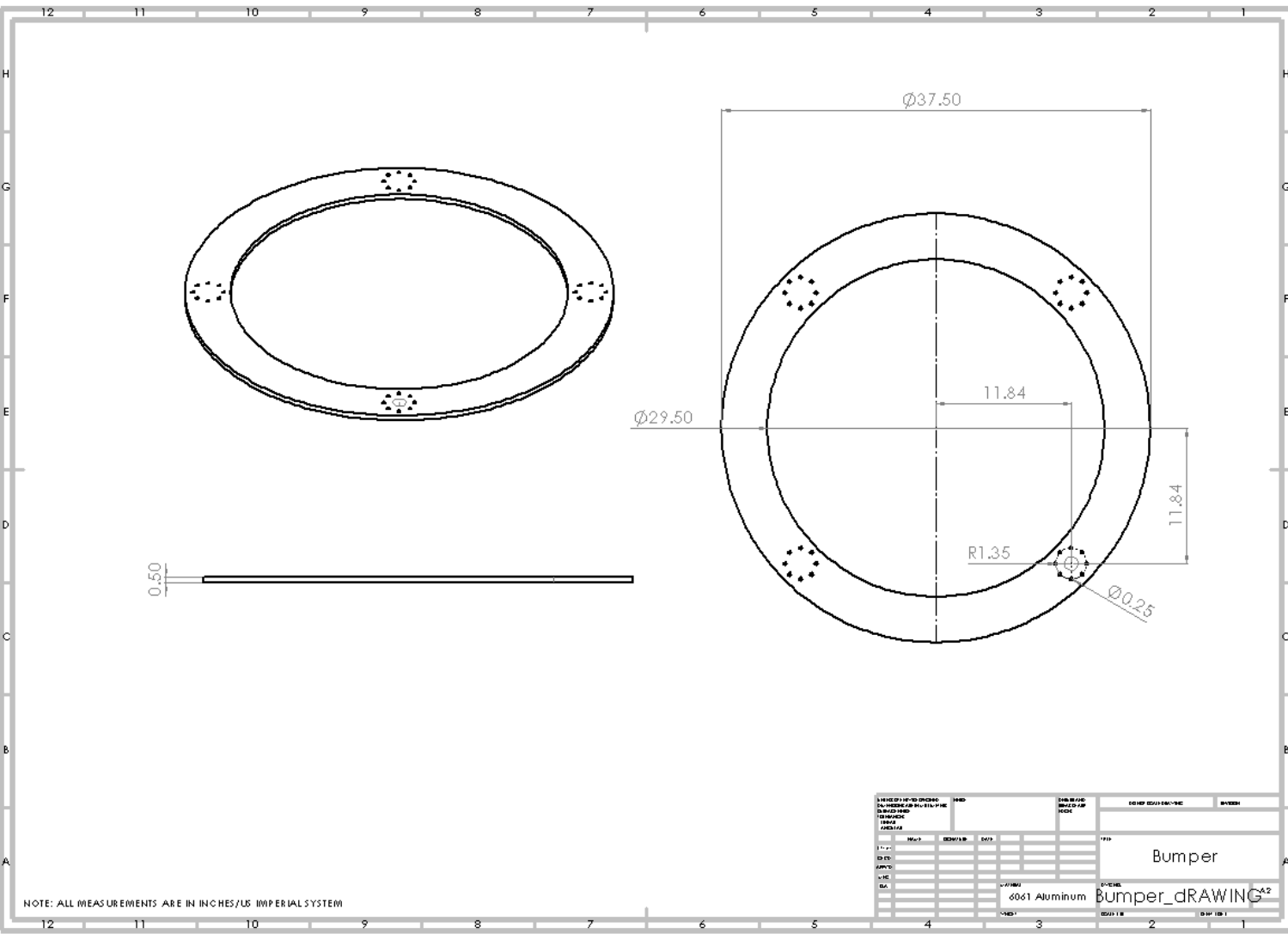


Cornell University

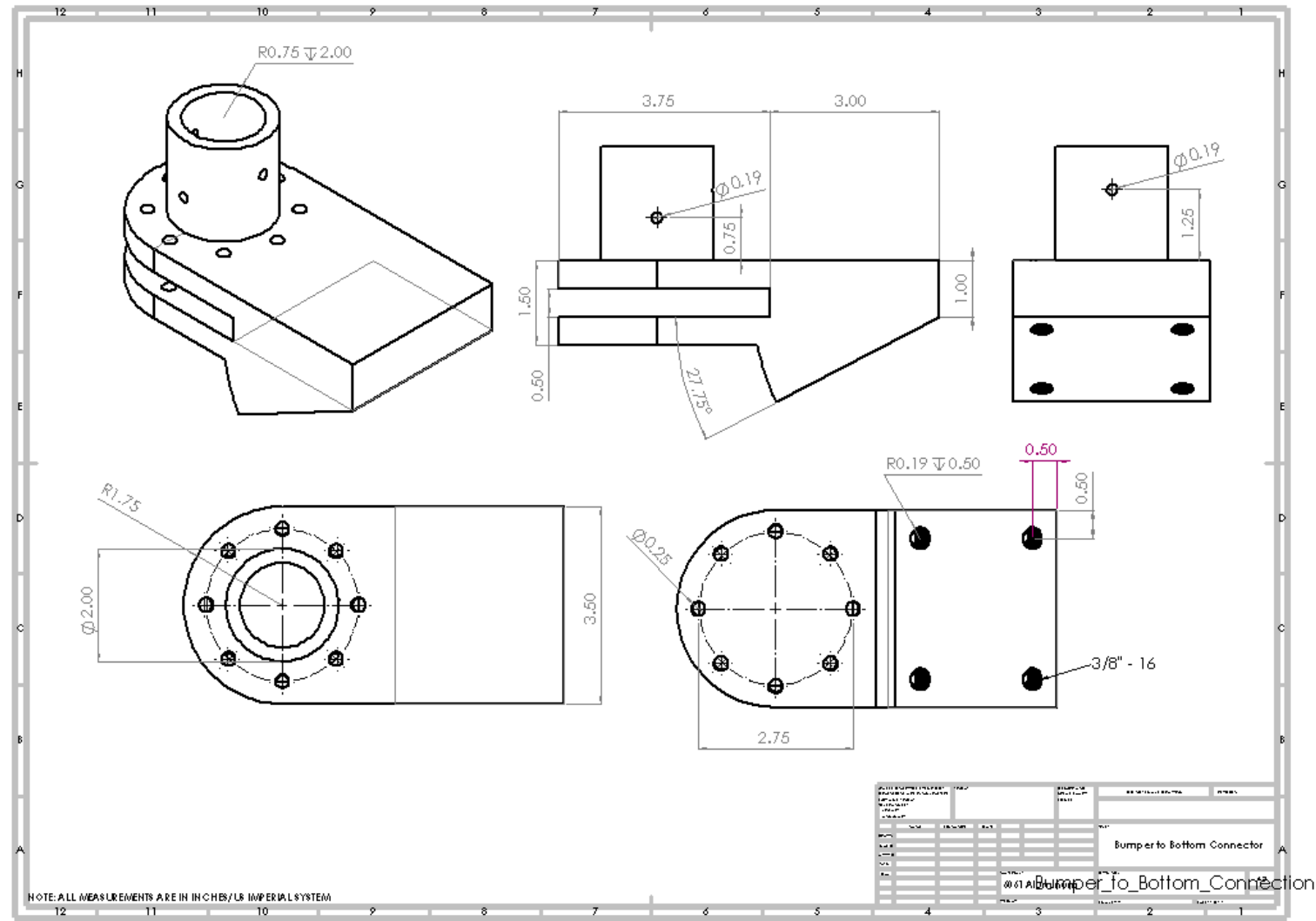




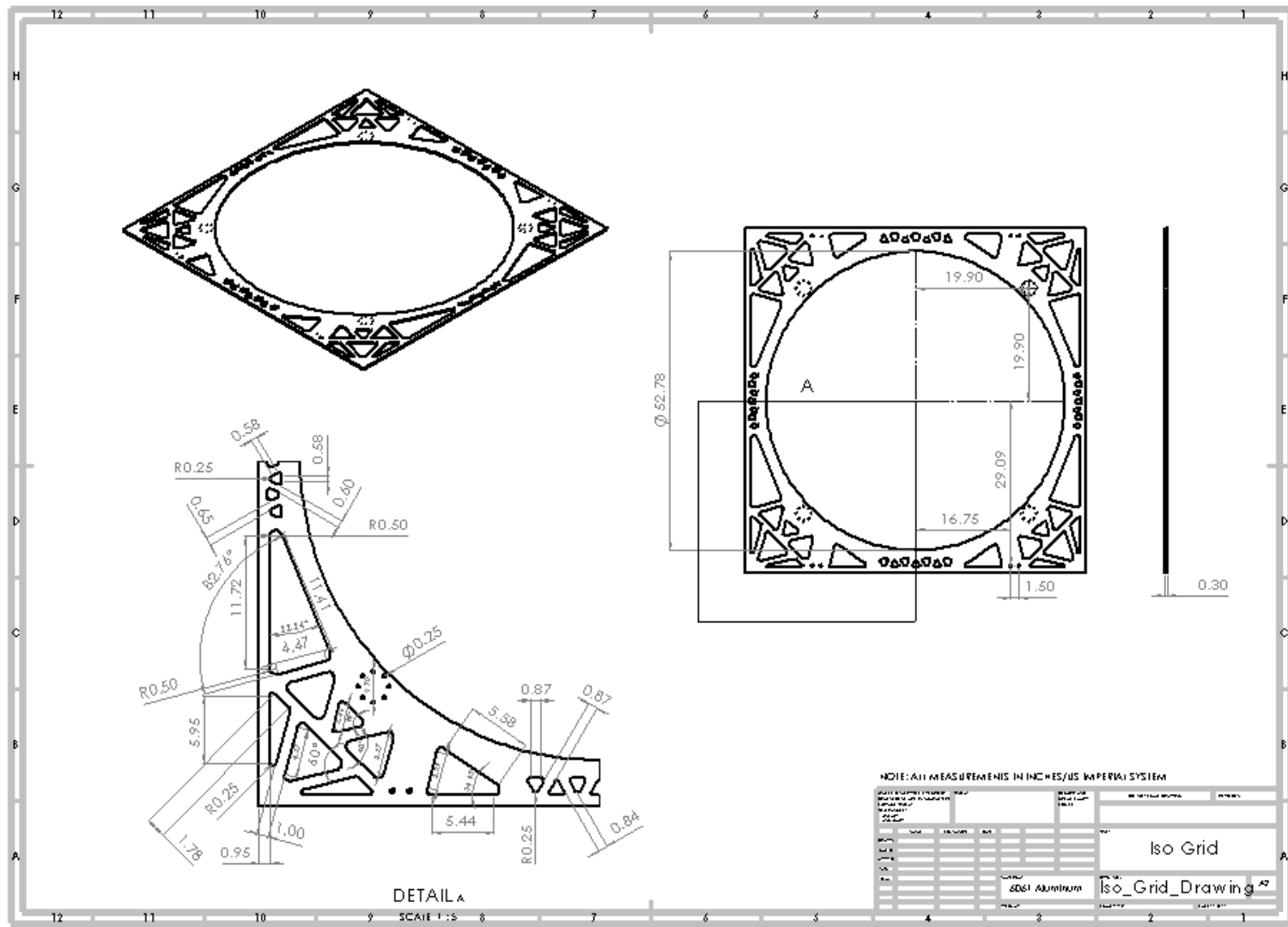
Cornell University.

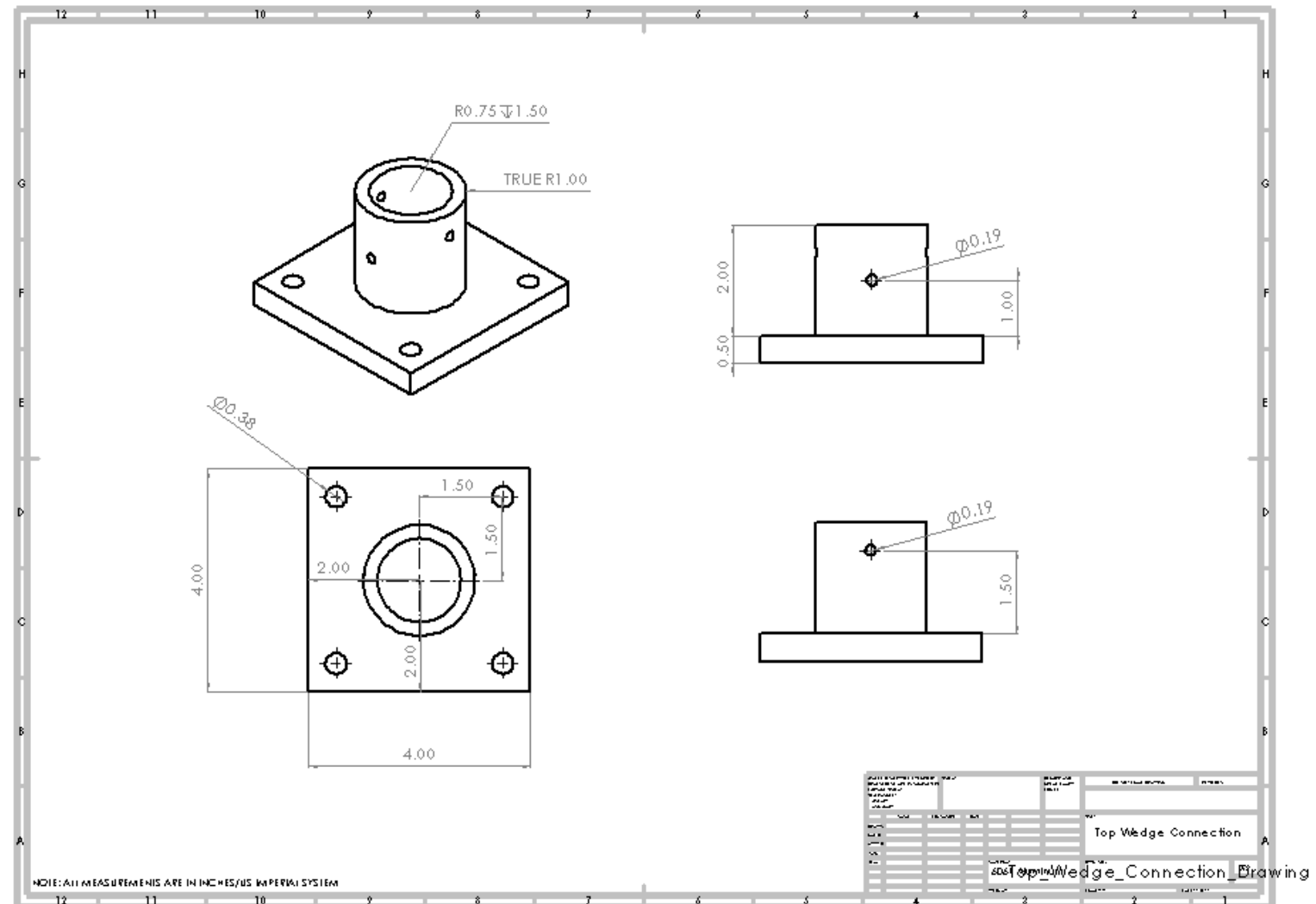


Cornell University

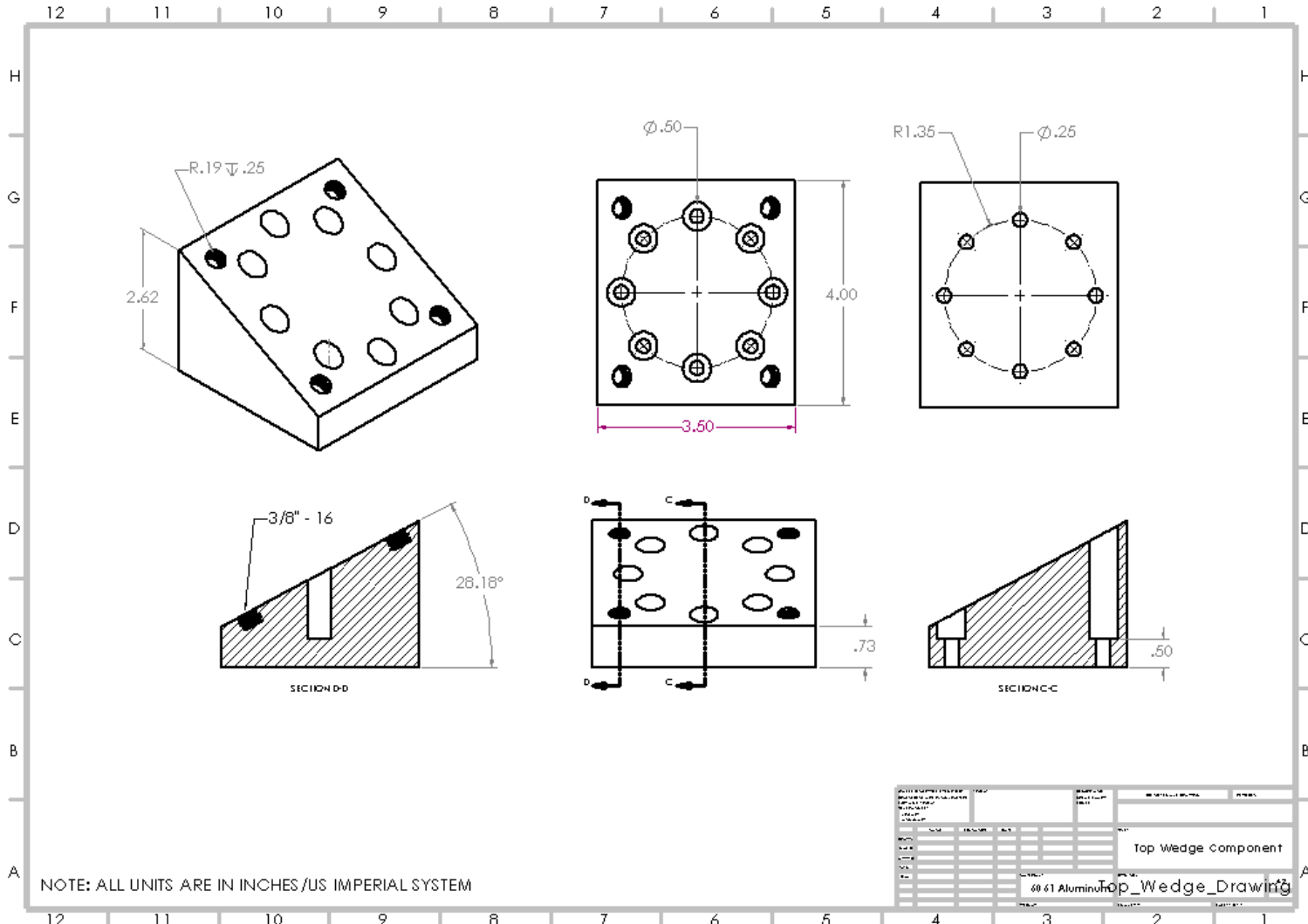


Cornell University

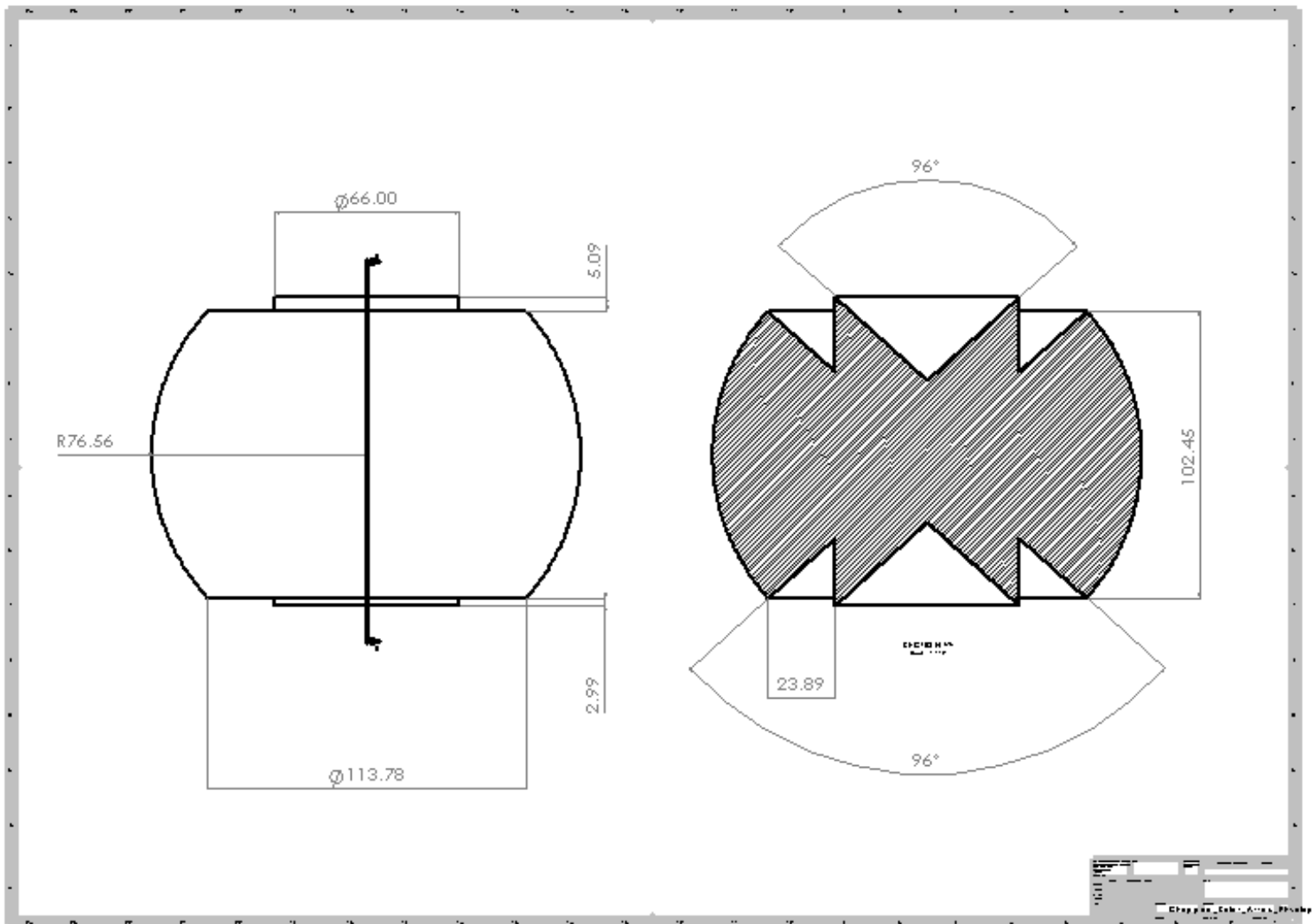




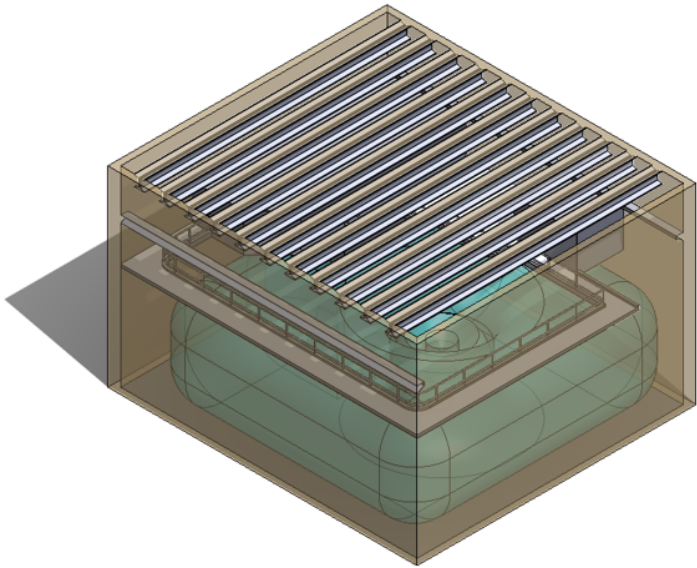
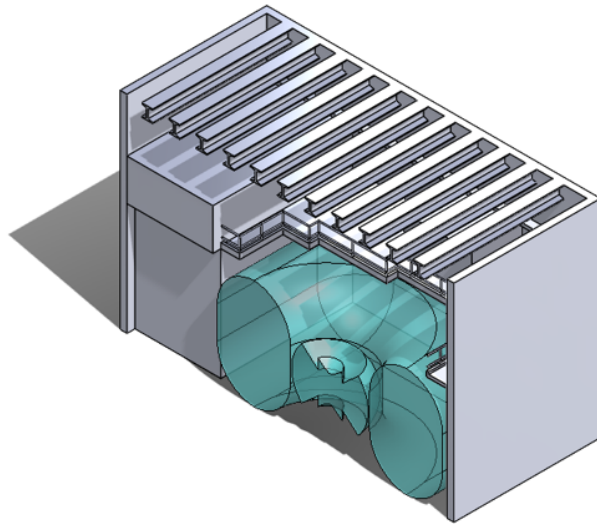
Cornell University.



Cornell University



Cornell University



## Appendix O

MATLAB script used for Mesh Convergence:

```

1 % Mesh refinement data
2 delta = [0.25, 0.125, 0.06, 0.03, 0.015]; % Mesh sizes
3 freq = [14.107, 12.999, 8.9136, 8.3698, 8.3091]; % Frequencies (Hz)
4 max_disp = [0.5546, 0.57207, 0.57684, 0.55097, 0.54899]; % Maximum
    displacement (m)
5
6
7 % Create fine mesh points for smooth fit
8 fine_mesh = linspace(min(delta), max(delta), 100);
9
10 % Polynomial fit (degree 2)
11 p_freq = polyfit(delta, freq, 2);
12 p_disp = polyfit(delta, max_disp, 2);
13 freq_fit = polyval(p_freq, fine_mesh);
14 disp_fit = polyval(p_disp, fine_mesh);
15
16 % Create figure
17 figure;
18
19 % Plot Frequency vs Mesh Size
20 subplot(2,1,1);
21 plot(delta, freq, 'o-', 'LineWidth', 2);
22 hold on;
23 plot(fine_mesh, freq_fit, '--', 'LineWidth', 1.5, 'Color', 'b');
24 hold off;
25 set(gca, 'XDir','reverse'); % Invert x-axis to show finer meshes on
    right
26 xlabel('Mesh Size');
27 ylabel('Frequency (Hz)');
28 title('Mesh Refinement Study: Frequency vs Mesh Size');
29 grid on;
30 legend('Data', '2nd Order Fit', 'Location', 'best');
31
32 % Plot Maximum Displacement vs Mesh Size
33 subplot(2,1,2);
34 plot(delta, max_disp, 's-', 'LineWidth', 2, 'Color', [0.8500 0.3250
    0.0980]);
35 hold on;
36 plot(fine_mesh, disp_fit, '--', 'LineWidth', 1.5, 'Color', [0.8500
    0.3250 0.0980]);
37 hold off;
38 set(gca, 'XDir','reverse'); % Invert x-axis
39 xlabel('Mesh Size');
40 ylabel('Maximum Displacement (m)');

```

```
41 title('Mesh Refinement Study: Max Displacement vs Mesh Size');
42 grid on;
43 legend('Data', '2nd Order Fit', 'Location', 'best');
44
45 % Improve layout
46 sgttitle('Mesh Refinement Analysis Results');
```



## Appendix P

Code Used for analysis between Freely-Rotating and Constant-Spin Modal Analyses:

```

1 % MATLAB Script to Plot Frequency and Maximum Displacement for
2 % Constant Spin vs Original Modal
3
4 % Data from the table
5 modes = [8, 9, 10, 11, 13];
6
7 % Frequencies (Hz)
8 freq_constant_spin = [9.3796, 11.075, 13.976, 14.405, 16.627];
9 freq_original_modal = [9.3796, 11.075, 13.977, 14.405, 16.646];
10
11 % Max Displacements (m)
12 disp_constant_spin = [0.059026, 0.17042, 0.14833, 0.17668, 0.32752];
13 disp_original_modal = [0.059007, 0.17042, 0.14753, 0.17668,
14     0.32891];
15
16 %% Plotting
17 figure;
18
19 % Plot Frequency Differences
20 subplot(2,1,1);
21 semilogy(modes, freq_constant_spin, 'ro-', 'LineWidth', 2, ...
22     'MarkerSize', 8);
23 hold on;
24 semilogy(modes, freq_original_modal, 'bs--', 'LineWidth', 2, ...
25     'MarkerSize', 8);
26 hold off;
27 grid on;
28 ylabel('Frequency (Hz)');
29 title('Comparison of Frequencies');
30 legend('Constant Spin', 'Original Modal', 'Location', 'northwest');
31 xlabel('Mode Number');
32
33 % Plot Displacement Differences
34 subplot(2,1,2);
35 semilogy(modes, disp_constant_spin, 'ro-', 'LineWidth', 2, ...
36     'MarkerSize', 8);
37 hold on;
38 semilogy(modes, disp_original_modal, 'bs--', 'LineWidth', 2, ...
39     'MarkerSize', 8);
40 hold off;
41 grid on;
42 ylabel('Max Displacement (m)');
43 title('Comparison of Maximum Displacements');

```



```

39 legend('Constant Spin', 'Original Modal', 'Location', 'northwest');
40 xlabel('Mode Number');
41
42 sgttitle('Constant Spin vs Original Modal Analysis Results');

```

```

1
2 % MATLAB Script to Plot Differences in Frequency and Max
   Displacement
3
4 % Data from the table
5 modes = [8, 9, 10, 11, 13];
6
7 % Frequencies (Hz)
8 freq_constant_spin = [9.3796, 11.075, 13.976, 14.405, 16.627];
9 freq_original_modal = [9.3796, 11.075, 13.977, 14.405, 16.646];
10
11 % Max Displacements (m)
12 disp_constant_spin = [0.059026, 0.17042, 0.14833, 0.17668, 0.32752];
13 disp_original_modal = [0.059007, 0.17042, 0.14753, 0.17668,
   0.32891];
14
15 % Compute Differences
16 delta_freq = freq_constant_spin - freq_original_modal;
17 delta_disp = disp_constant_spin - disp_original_modal;
18
19 %% Plotting Differences
20 figure;
21
22 % Plot Frequency Differences
23 subplot(2,1,1);
24 bar(modes, delta_freq, 'FaceColor', [0.2 0.6 0.8]);
25 grid on;
26 ylabel('\Delta Frequency (Hz)');
27 title('Frequency Differences (Constant Spin - Original Modal)');
28 xlabel('Mode Number');
29
30 % Plot Displacement Differences
31 subplot(2,1,2);
32 bar(modes, delta_disp, 'FaceColor', [0.8 0.4 0.4]);
33 grid on;
34 ylabel('\Delta Max Displacement (m)');
35 title('Max Displacement Differences (Constant Spin - Original Modal
   ');
36 xlabel('Mode Number');
37
38 sgttitle('Differences Between Constant Spin and Original Modal
   Analysis');

```

## 9. List of Variables

Symbol	Description
$F$	Force (N)
$x$	Displacement (m)
$k$	Spring stiffness (N/m)
$\sigma$	Normal stress (Pa)
$\epsilon$	Normal strain (unitless)
$E$	Young's modulus (Pa)
$l$	Original length of the bar (m)
$A$	Cross-sectional area ( $m^2$ )
$\Delta l$	Change in length (m)
$M$	Mass matrix
$K$	Stiffness matrix
$\tilde{K}$	Mass-normalized stiffness matrix
$\lambda$	Eigenvalue ( $rad^2/s^2$ )
$\omega$	Natural frequency (rad/s)
$v$	Eigenvector (mode shape)
$q$	Generalized coordinates
$\zeta$	Damping ratio (unitless)
$L$	Cholesky factor of mass matrix
$I$	Identity matrix
$\tau$	Torque (N·m)
$\Omega$	Spin rate (rad/s)
$\omega_n$	Nutation frequency (rad/s)
$f_n$	Nutation frequency (Hz)
$I_x, I_y, I_z$	Principal moments of inertia ( $kg \cdot m^2$ )
$u_d$	Displacement vector (DOF space)
$u_b$	Boundary displacement vector
$u_\ell$	Interior displacement vector
$M_{cb}, K_{cb}$	Craig-Bampton mass and stiffness matrices
$M_{bb}, M_{bq}, M_{qb}, M_{qq}$	Submatrices of Craig-Bampton mass matrix
$K_{bb}, K_{qq}$	Submatrices of Craig-Bampton stiffness matrix
$\phi_{cb}$	Craig-Bampton transformation matrix
$\phi_r, \phi_\ell$	Constraint modes and normal modes
$F(t)$	External force vector as function of time (N)

## References

- [1] ANSYS Inc. Datum objects: Axis insert. [https://ansyshelp.ansys.com/public/account/secured?returnurl=/Views/Secured/corp/v242/en/discovery/Discovery/user\\_manual/design/t\\_datum-objects\\_axis\\_insert.html](https://ansyshelp.ansys.com/public/account/secured?returnurl=/Views/Secured/corp/v242/en/discovery/Discovery/user_manual/design/t_datum-objects_axis_insert.html), 2024.
- [2] ANSYS Inc. Modal analysis type. [https://ansyshelp.ansys.com/public/account/secured?returnurl=/Views/Secured/corp/v242/en/wb\\_sim/ds\\_modal\\_analysis\\_type.html](https://ansyshelp.ansys.com/public/account/secured?returnurl=/Views/Secured/corp/v242/en/wb_sim/ds_modal_analysis_type.html), 2024.
- [3] ANSYS Inc. Rotational velocity boundary condition. [https://ansyshelp.ansys.com/public/account/secured?returnurl=/Views/Secured/corp/v242/en/wb\\_sim/ds\\_Rotational\\_Velocity.html](https://ansyshelp.ansys.com/public/account/secured?returnurl=/Views/Secured/corp/v242/en/wb_sim/ds_Rotational_Velocity.html), 2024.
- [4] ANSYS Inc. Static structural analysis type. [https://ansyshelp.ansys.com/public/account/secured?returnurl=/Views/Secured/corp/v242/en/wb\\_sim/ds\\_static\\_mechanical\\_analysis\\_type.html](https://ansyshelp.ansys.com/public/account/secured?returnurl=/Views/Secured/corp/v242/en/wb_sim/ds_static_mechanical_analysis_type.html), 2024.
- [5] Ferdinand P. Beer, E. Russell Johnston, John T. DeWolf, and David F. Mazurek. *Mechanics of Materials*. McGraw-Hill Education, 7th edition, 2015.
- [6] Austin Downey. Vibration mechanics, 2022. GitHub repository.
- [7] European Cooperation for Space Standardization (ECSS). Space engineering: Structural load analysis. Technical Report ECSS-E-ST-32-10C, ECSS, 2008.
- [8] Walter G. Hurty and Robert R. Craig Jr. *Structural Dynamics: An Introduction to Craig-Bampton Methods*. Cornell University Library, 1968.
- [9] Robert J. Kuether and Matthew S. Allen. A comparison of craig–bampton and non-linear reduced-order modeling for substructuring. In *Proceedings of the 32nd International Modal Analysis Conference (IMAC)*, 2014.
- [10] NASA. Structural design and test factors of safety for spaceflight hardware. Technical Report NASA-STD-5001B, NASA, 2020.
- [11] NASA Goddard Space Flight Center. General environmental verification specification (gevs) for gsfc flight programs and projects. Technical Report GSFC-STD-7000, NASA, 2013.
- [12] Scott Gordon. The craig-bampton method. <https://studylib.net/doc/9557139/the-craig-bampton-method>, 1999.
- [13] James R. Wertz and Wiley J. Larson. *Space Mission Analysis and Design*. Microcosm Press and Springer, 3rd edition, 1999.